

REPORT DOCUMENTATION PAGE				Form Approved OMB No. 0704-0188	
Public reporting burden for this collection of information is estimated to average 1 hour per response, including the time for reviewing instructions, searching existing data sources, gathering and maintaining the data needed, and completing and reviewing this collection of information. Send comments regarding this burden estimate or any other aspect of this collection of information, including suggestions for reducing this burden to Department of Defense, Washington Headquarters Services, Directorate for Information Operations and Reports (0704-0188), 1215 Jefferson Davis Highway, Suite 1204, Arlington, VA 22202-4302. Respondents should be aware that notwithstanding any other provision of law, no person shall be subject to any penalty for failing to comply with a collection of information if it does not display a currently valid OMB control number. PLEASE DO NOT RETURN YOUR FORM TO THE ABOVE ADDRESS.					
1. REPORT DATE (DD-MM-YYYY) 06-02-2017		2. REPORT TYPE Final Report		3. DATES COVERED (From - To) Nov. 2013 - Dec. 2016	
4. TITLE AND SUBTITLE Experimental Investigation of Free Field and Shock-Initiated Implosion of Composite Structures				5a. CONTRACT NUMBER	
				5b. GRANT NUMBER N00014-10-1-0662	
				5c. PROGRAM ELEMENT NUMBER	
6. AUTHOR(S) Arun Shukla				5d. PROJECT NUMBER	
				5e. TASK NUMBER	
				5f. WORK UNIT NUMBER	
7. PERFORMING ORGANIZATION NAME(S) AND ADDRESS(ES) University of Rhode Island 70 Lower College Rd. Kingston, RI 02881-0811				8. PERFORMING ORGANIZATION REPORT NUMBER	
9. SPONSORING / MONITORING AGENCY NAME(S) AND ADDRESS(ES) Office of Naval Research 875 North Randolph St. Arlington, VA 22203-1995				10. SPONSOR/MONITOR'S ACRONYM(S)	
				11. SPONSOR/MONITOR'S REPORT NUMBER(S)	
12. DISTRIBUTION / AVAILABILITY STATEMENT Nonclassified; Unlimited Distribution					
13. SUPPLEMENTARY NOTES					
14. ABSTRACT A comprehensive series of experimental studies is performed to study the implosion behavior of a variety of different composite structures under varying loading conditions. Experiments are performed in a large pressure vessel designed to maintain constant hydrostatic pressure during collapse. 3D Digital Image Correlation (DIC) is calibrated for submerged structures and used in conjunction with high-speed cameras to provide full-field displacement data in conjunction with pressure data to investigate collapse mechanics. Studies performed investigate: i) the natural implosion of carbon-fiber epoxy cylinders, ii) natural implosion of GFRP cylinders, iii) the differences in behavior between the aforementioned materials and aluminum during implosion, iv) dynamic mode evolution in the collapse of CFRP cylinders, v) mitigation of pressure pulses from CFRP cylinder implosion using polyurea coatings, vi) the collapse of CFRP cylinders under subcritical pressure and shock loading, and vii) the collapse of double hull composite structures. Results from each provide significant new understanding of the collapse mechanics of these structures, with applications to the design and development of undersea vehicles and piping.					
15. SUBJECT TERMS Blast Mitigation, Buckling, Carbon-fiber/epoxy, Collapse Mode, Composite Structures, Double Hull, Digital Image Correlation (DIC), Fluid-Structure Interaction, GFRP, Implosion, Pressure Wave, Shock Wave, Underwater Explosion (UNDEX)					
16. SECURITY CLASSIFICATION OF:			17. LIMITATION OF ABSTRACT	18. NUMBER OF PAGES 225	19a. NAME OF RESPONSIBLE PERSON Arun Shukla
a. REPORT	b. ABSTRACT	c. THIS PAGE			19b. TELEPHONE NUMBER (include area code) 1-401-874-2283

Table of Contents

Chapter 1 : Study of Implosion of Carbon/Epoxy Composite Hollow Cylinders Using 3-D Digital

Image Correlation.....1

Introduction	3
Materials	5
Experimental Procedure	7
DIC Technique	8
Collapse Pressure Predictions	12
Specific and Total Impulse	13
Results and Discussion	14
Large Diameter Filament-Wound Specimens (CT)	14
Reduced Diameter Filament-Wound Specimens (CTRD)	19
Roll-Wrapped Specimens (RC)	23
Braided Specimens (BC)	27
Pressure History Parameters	32
Impulse	34
Surface Cavitation	36
Conclusions	40
Acknowledgements	41
References	41

Chapter 2 : Hydrostatic Implosion of GFRP Composite Tubes Studied by Digital Image

Correlation.....45

Introduction	47
Experimental Details	49
DIC Technique	52
Collapse Pressure Predictions	56
Specific and Total Impulse	57
Time-Frequency Analysis	57
Results and Discussion	59
57.2mm Filament-Wound Tube (RT)	59
101.8mm Filament-Wound Tube (GT)	64
Braided Tube (BG)	69
Pressure Parameters	74
Impulse	76
Wavelet Analysis	78
Conclusions	79
References	80
Chapter 3 : Experimental Investigation on Underwater Buckling of Thin-walled Composite and Metallic Structures.....	84
Introduction	86
Experimental Details	88
Specimen Geometry	88
2.2 DIC Technique	90
Flow Energy	91

Results	93
Aluminum Tubes	93
Filament-Wound Carbon	95
Filament-Wound Glass	99
Discussion	102
Suction Region	102
Pressure Parameters	104
Total Flow Energy	104
Circumferential DIC Results	106
Conclusions	107
Acknowledgements	108
References	108
Chapter 4 : Dynamic Collapse Mode Evolution in Carbon Composite Tubes.....	112
Introduction	114
Materials	115
Experimental Procedure	115
Results and Discussion	116
Conclusions	121
Acknowledgements	121
References	121
Chapter 5 : Mitigation of Pressure Pulses from Implosion of Hollow Composite (CFRP) Cylinders	
.....	124

Introduction	126
Experimental Details	128
DIC Technique	130
Total Flow Energy	131
Results and Discussion	132
Underpressure Comparison	133
Overpressure Comparison	135
Midpoint Velocity	136
Midpoint Acceleration	138
Flow Energy	139
Effect of Exterior Coatings on Damage	141
Conclusions	144
Acknowledgements	145
References	145

Chapter 6 : Shock-Initiated Buckling of Carbon/Epoxy Composite Tubes at Sub-Critical Pressures

.....	149
Introduction	151
Experimental Details	152
Results	155
Natural Implosion Experiments	155
Interaction of Shock Wave with Specimen	158
Identifying Features of the Pressure History	160

Near-Field Explosion (102mm Standoff)	163
Mid-Field Explosion (203mm Standoff)	166
Far-Field Explosion (305mm Standoff)	168
DIC Analysis of Initial Shock Response	170
Conclusions	173
Acknowledgements	174
References	174

Chapter 7 : Dynamic Instabilities in Double Hull Composite Cylinders Under Hydrostatic Pressure

.....	177
Introduction	179
Material Selection and Specimen Design	182
Experimental Procedure	182
Analysis	184
Increase in collapse pressure	184
Composite Thickness Effects on Collapse Pressure	185
Impulse	187
Energy	189
Results and Discussion	190
Predicting Collapse Pressure	190
Collapse Behavior Categories	191
DIC Contours	193
Double Hull Implosion Pressure Pulse	199

Impulse and Energy	205
Post-Mortem Specimen Evaluation	206
Conclusions	212
Acknowledgements	214
References	214

Chapter 1 : Study of Implosion of Carbon/Epoxy Composite Hollow Cylinders Using 3-D Digital Image Correlation

by

Michael Pinto, Sachin Gupta, and Arun Shukla

has been published in Composite Structures

Corresponding Author: Arun Shukla

Dynamic Photo Mechanics Laboratory

Department of Mechanical, Industrial and Systems Engineering

University of Rhode Island

206 Wales Hall, 92 Upper College Rd Kingston, RI, 02881,

USA Phone: +1-401-874-2283

Email Address: shuklaa@uri.edu

ABSTRACT

A comprehensive study on the hydrostatic implosion of carbon fiber reinforced epoxy composite tubes is conducted experimentally to examine the failure and damage mechanisms of collapse. Experiments are performed in a pressure vessel designed to provide constant hydrostatic pressure through the collapse. Filament-wound, braided, and roll-wrapped carbon-fiber/epoxy tubes are studied to explore the effect of geometry and reinforcement architecture on the modes of failure. 3-D Digital Image Correlation technique, which is first calibrated for the underwater environment, is used to capture the full-field deformation and velocities during the implosion event. Dynamic pressure transducers are employed to measure the pressure pulses generated by the event and evaluate its damage potential. The results show that composites with braided fabric reinforcements are found to have more damage potential to adjacent structures than those containing unidirectional reinforcements, as they release pressure waves with significantly greater impulse.

Introduction

The use of composites has attracted attention in underwater marine applications due to the array of advantages offered by these materials. Composite materials offer alternatives with reduced weight, improved corrosion resistance, and for submerged structures, greater potential operating depths. In addition, these materials provide improved stealth qualities by having very low thermal, acoustic, and magnetic signatures, increasing their appeal for military applications. For these reasons, the presence of composite materials in marine industries is increasing, and are currently used in several naval applications, such as sonar domes, masts, and hull sheathings[1]. One of the biggest obstacles to widespread adaptation of composite materials is a lack of complete understanding and simple design rules for these materials, especially under extreme loading conditions[1]. For this reason, the present work looks to expand the current knowledge of composite behavior by examining the problem of implosion.

The implosion of a submerged structure occurs when external pressure reaches a critical value, causing an instability in the structure and resulting in a rapid and often catastrophic collapse. During this collapse, the boundaries of the structure and surrounding fluid are accelerated to high velocities and stop suddenly once the collapse is completed. This abrupt change in momentum releases a pressure wave into the surrounding fluid, which can have the potential to damage nearby structures[2-4]. A dramatic example of this occurred at the Super-Kamiokande facility in Japan, where the implosion of a single photomultiplier tube released a shock wave powerful enough to trigger a chain reaction of collapses, resulting in the implosion of nearly 7000 adjacent tubes, causing \$20-30 million of damage [2,3]. For this reason, the implosion problem has gained much attention in recent decades. The implosion of glass spheres has been studied by several authors who characterized the pressure pulse emitted during collapse as well as its potential for

damage to nearby structures[4-7]. The implosion of aluminum tubes has also been studied in recent work. Turner and Ambrico identified key stages of the implosion event in relation to the local pressure about the collapsing structure [8]. In this work, the implosion of aluminum tubes resulted in (i) an initial period of underpressure as the tube volume is reduced, (ii) a small, sharp peak corresponding to the wall-to-wall contact at the completion of collapse, (iii) a larger positive pressure peak resulting from the change in momentum of surrounding fluid, and (iv) a broad overpressure period as the collapse propagates through the length of the tube. Also in this work, robust fluid-structure computational models are developed which correlated quite well with experimental data. Most recently, Ikeda et. al studied the free-field implosion of aluminum and brass tubes with varying geometries [9]. This work examined the effect of different modes of collapse on the emitted pressure pulse, and used bubble dynamic scaling laws to compare these changes.

Though several analytical treatments exist on the subject, the implosion of composite tubes under hydrostatic loading has only been experimentally studied in a few previous works. Moon et al. examined implosion of filament-wound carbon/epoxy composite tubes with different winding angles both experimentally and computationally to determine collapse pressures and modes[10]. Both Ross and Smith performed experiments on carbon/E-glass tubes to determine critical buckling pressure, buckling modes, and create design tables[11,12]. Hernandez-Moreno et al. studied filament-wound glass/epoxy composite tubes with a winding angle of 55° to examine effects of winding pattern on the collapse pressure[13]. Hur et al. examined the buckling modes, loads, and play failure of carbon/epoxy tape layup tubes both experimentally and computationally[14]. Yang et al. developed an analytic model for critical buckling pressure based on anisotropic laminate theory and performed experiments on E-glass/epoxy tubes to test

predictions[15]. However, in none of these studies is the pressure pulse from the collapse measured, nor are high-speed images of the collapse event captured. Therefore there is a lack of understanding of the implosion of composite tubes in terms of how it will affect the local pressure fields in surrounding fluid. This study addresses the existing gap in knowledge by examining the pressure pulses emitted in collapse of carbon-fiber reinforced composite tubes and capturing full-field displacements during the implosion event. In addition, this study seeks to evaluate the effects of reinforcement architecture on implosion to help guide material selection to reduce damage potential to nearby structures. It is shown that the implosion of carbon/epoxy tubes results in the release of potentially hazardous pressure waves, and that the type of reinforcement used in the materials plays a significant role in the impulse delivered by that wave. Due to the enhanced brittle nature of the failure of braided preforms, specimens with that type of reinforcement release pulses with the greatest impulse upon collapse.

Materials

The implodable volumes in this study are laminated carbon/epoxy composite tubes. Three different reinforcing fabric architectures are studied, filament-wound, roll-wrapped, and braided carbon fabric. The filament-wound tubes consist of seven layers of unidirectional carbon fabric reinforcement arranged in a $[\pm 15/90/\pm 45/\pm 15]$ layup. The tubes are manufactured by Rock West Composites (West Jordan, UT) with a nominal wall thickness of 1.52mm and are thoroughly sanded on the exterior surface for excellent finish and tolerances. Tubes of two different inner diameters are studied, 76.2mm (notated as CT) and 60.3mm (notated as CTRD). The roll-wrapped tubes contain 11 layers of unidirectional tape, arranged in a $[0_3/\pm 45/90/\pm 45/0_3]$ layup. These tubes are also manufactured by Rock West Composites, with a nominal inner diameter of 76.2mm and nominal thickness of 1.52mm. The braided composite tubes are constructed of two

layers of braided carbon fabric reinforcement sandwiching one unidirectional layer to obtain a $[\pm 45/90/\pm 45]$ layup. The specimens are manufactured by Dragonplate™ (Elbridge, New York) with an inner diameter of 76.2mm and a nominal wall thickness of 2.03mm. All composite tube specimens are cut to have an unsupported length of 279.4mm. The dimensions are selected as to provide specimens with a relatively low expected collapse pressure, and a high radius-to-thickness ratio (>18) so that thin-wall assumptions may be utilized. At least two experiments are performed to demonstrate repeatability.

Specimen	Reinforcement	Inner Diameter (mm)	Wall Thickness (mm)	L/D	Effective Modulus $\left[\sqrt{E_{11}^2 + E_{22}^2} \right]$ (GPa)
CT	Filament-Wound	76.4	1.39	3.7	74.2
CTRD	Filament-Wound	60.4	1.58	4.6	78.4
RC	Roll-Wrapped	76.3	1.63	3.7	91.1
BC	Braided	75.8	2.12	3.7	41.0

Table 1: Geometric and material properties of studied specimens

Experimental Procedure

All implosion experiments are conducted in a large spherical (2.1m dia.) pressure vessel with a maximum pressure rating of 6.89MPa to provide constant hydrostatic pressure throughout the collapse event. Several Plexiglass windows mounted about the midspan of the pressure vessel allow the specimens to be viewed by cameras and adequately lit by two high intensity light sources.

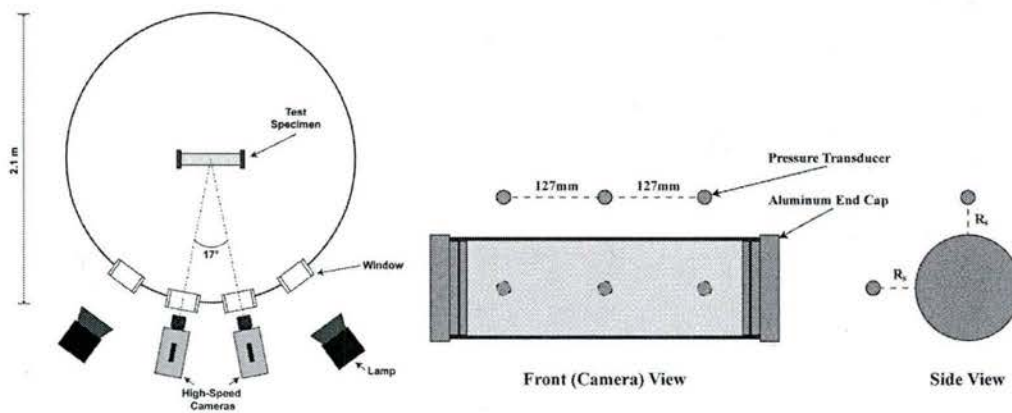


Figure 1: Experimental apparatus (left) and test specimen configuration (right)

Prior to set-up, all composite tube specimens are sealed using two aluminum end caps fitted with rubber O-rings. The specimen is suspended horizontally in the center of the pressure vessel using several steel cables attached to the inner walls of the vessel. The tubes are secured in such a way that they cannot move or float during the filling process and the painted surface is faced toward the viewing windows. To measure the changes in local pressure during the collapse event, several dynamic pressure transducers (PCB 138A05, PCB Piezotronics, Inc., Depew, NY) are mounted at different locations about the specimen both axially and circumferentially (Figure 1). Three sensors are located at the midspan of the specimen, and four are located at axial offsets 127mm from the midspan. All sensors are mounted such that the standoff distance, R_s , between

the sensing element and the outer surface of the specimen is nominally 45mm. The amplified outputs of these sensors are monitored by an Astro-med Dash® 8HF-HS portable data recorder (Astro-Med Inc., West Warwick, RI) at a sampling rate of 2 MHz.

The vessel is then flooded with water that is filtered for maximum optical clarity, leaving a small air pocket at the top. Once the vessel is filled, nitrogen gas is introduced into the air pocket to pressurize the vessel. The pressure inside the vessel is increased at a gradual rate (0.083 MPa/min) until the specimen collapsed. At this point, the cameras and pressure sensors are end triggered to record the data occurring 1 second prior to triggering. In this way, data is collected for the entire collapse event by all recording devices.

DIC Technique

A random speckle pattern is applied to a region covering the entire length of the specimen and approximately half of the circumference using flat black paint. These circular speckles are painted with a diameter of at least 2mm so that each mark occupies a minimum of 3x3 pixels in the recorded images. This region is painted white prior to speckling to enhance the contrast of the pattern. Two high-speed cameras (Photron SA1, Photron USA, Inc.), offset by 17° are used to capture stereo images of the patterned region of the specimen at 50,000 frames/s for CT and RC tubes, 45,000 frames/s for BC tubes, and 36,000 frames/s for CTRD tubes. The stereo images are analyzed using a commercially available image correlation software, VIC3D 2012(Correlated Solutions, Inc., Columbia, SC).

3-D Digital image correlation (DIC) is a well known experimental tool used to determine real-time, full-field displacements across the viewable surface of the specimen throughout the implosion event [16]. This technique is calibrated for underwater testing based on previous work

[17] for good confidence in the accuracy of measured displacements and velocities. Here, the basic methodology and results of that work are summarized.

To evaluate the accuracy of using the 3-D DIC methodology for determining 3-D positions for points on a submerged object, calibration experiments are conducted by imaging a submerged calibration specimen within a small custom designed tank. This technique replicates the optical effects of submersion using a more accessible smaller tank. A schematic of the setup is shown in Figure 2. The setup is approximately 600 mm long and 200 mm wide with height of 150 mm. Two acrylic windows, of same thickness to those used in the pressure chamber are installed with a stereo angle of $\sim 20^\circ$ for viewing purpose. A 76 mm x 51 mm (3 in x 2 in) speckled flat aluminum specimen is mounted inside the tank on a precision translation stage, which can provide both in-plane and out-of-plane translation with 0.01 mm accuracy.

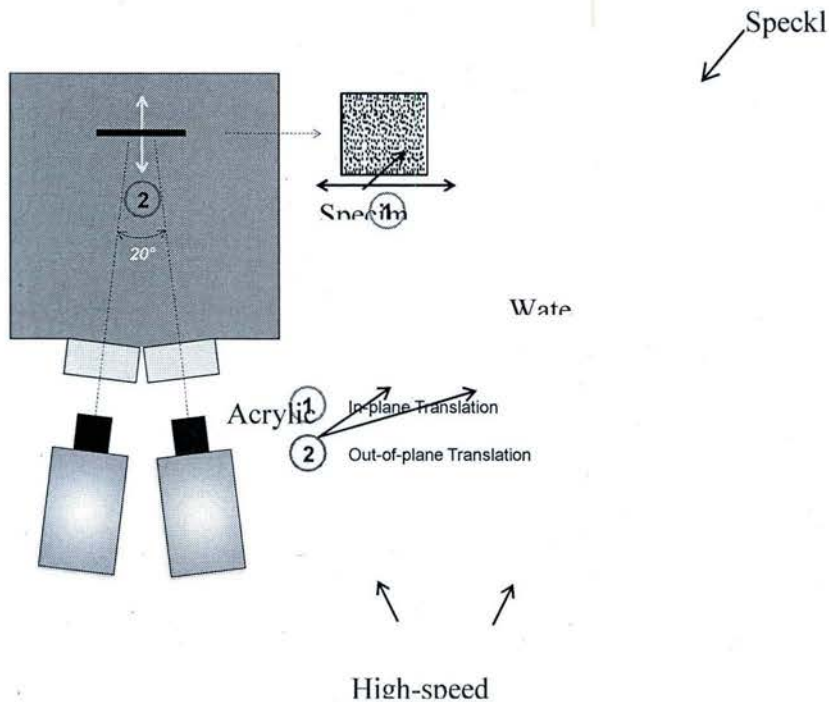


Figure 2: Calibration experiment for 3D DIC of submerged structures

High-speed cameras are placed outside the tank such that the surface normal of each window is aligned with the optical axis of the respective camera. The resolution of the camera image is 1024 x 1024 pixels, corresponding to an approximate magnification factor of 11.44 pixels/mm. The specimen is placed at the intersection point of the two camera axes inside the tank (450 mm deep in water), a location that is consistent with implosion experiments. Using the translation stage, the specimen is translated in 1 mm increments in both in-plane and out-of-plane direction and the corresponding images are captured. Displacement of the specimen at each translation increment is estimated with Vic-3D software.

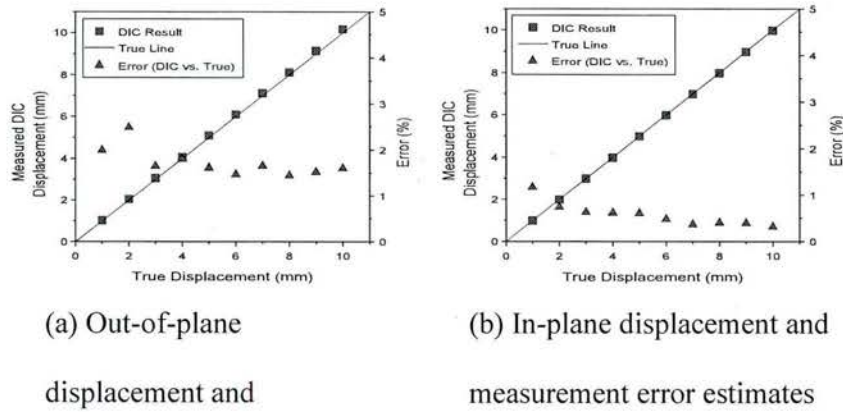


Figure 3: Calibration results for out-of-plane and in-plane translation

A plot of the actual out-of-plane displacement and the measured average displacement of the specimen is shown in Figure 3(a). The measured average surface displacements are in good agreement with the true displacements and the percentage error between true and measured out-of-plane displacement is ~1.5% to 2.5%. The magnitude of absolute error are nearly proportional to the given displacement value, which results in an approximately constant percentage error.

Hence, it can be concluded that the out-of-plane displacements can be accurately captured ($< 3\%$ error) for the underwater experiments.

A comparison of given in-plane displacement and measured average DIC displacement as shown in Figure 3(b) indicates that the two are in very good agreement. The absolute magnitude of error is nearly constant ~ 0.02 to 0.03 mm for the range of given displacement and therefore the percentage error shown in Fig. 4(b) decreases (from 1.2% to 0.5%) with increase in displacement. Therefore, when the optical axis of cameras is aligned with the normal of the viewing windows, both in-plane and out-of-plane displacements can be measured with good accuracy for submerged objects by using the camera and stereo parameters obtained using a submerged calibration grid.

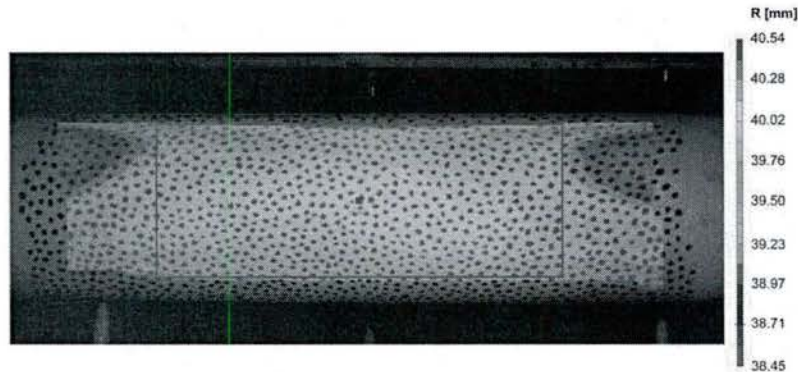


Figure 4: Example of radius reconstruction of submerged RC composite tube

To further validate the DIC technique for underwater experiments, the outer radii of each specimen are reconstructed using DIC software prior to each experiment. In each case, the calculated outer radius is very close to the measured value, typically within 1mm. As an example, an image of a typical RC specimen with reconstructed radius is shown in Figure 4. In the region indicated by the box, the average calculated radius is 39.80mm with a standard

deviation of 0.19mm. This is very close to the true outer radius of 39.78mm and gives excellent confidence in the accuracy of DIC in this application.

Collapse Pressure Predictions

Several authors have employed laminate and shell theory to predict the buckling collapse pressure of laminated composite tubes under hydrostatic pressure [18,19]. These approaches make the assumption that the tube is thin-walled and very long, and casts an eigenvalue problem based on the constitutive equations of the net laminate structure. It has been observed theoretically [20,21] as well as experimentally [9,11] that the length/diameter ratio of thin-walled tube specimens has a significant effect on the collapse pressure and mode of the tube, and that shorter tubes ($L/D=2$) generally have a much higher collapse pressure than longer tubes ($L/D=8$). Therefore, it is important to take the sample length into consideration when estimating the collapse pressure of real test structures.

Koudela and Strait [22] developed such a procedure to create design formulae for laminated and sandwich composite tubes under hydrostatic pressure. These authors started with the Von Mises solution[21] for isotropic tubes and made several empirical modifications to the above formula to account for the anisotropy of the laminates and the non-uniform distribution of stress through the thickness of the laminate, resulting in the following modified design equation:

$$P_{critical,ani} = \frac{0.85\sqrt{E_1 E_2} t^{2.5}}{(1-\nu_{12}\nu_{21})^{0.75} L R_c^{0.5} R_o} * \frac{1}{1 + \frac{\sqrt{E_1 E_2} t^2}{12 R_c R_o G}} \quad (1)$$

Here, E_1 and E_2 are the longitudinal and transverse moduli, respectively, ν_{12} and ν_{21} are Poisson's ratios of the two major axes, R_o is the outer radius of the laminate, and G is the shear modulus. The values for these parameters were based on manufacturer data.

Finally, the expected collapse pressure and shape are also predicted using Finite Element Analysis (FEA) with commercially available ABAQUS software (Dassault Systèmes Americas Corp., Waltham, MA). A linearized buckling analysis [23] is conducted using this software package to obtain the first buckling mode and pressure. This analysis is performed to increase confidence in the validity and repeatability of experimental observations.

For the tubes in this study, the analytic and empirical predictions of buckling pressure described above provided a useful means of estimating the magnitude of the collapse pressure and provided an upper bound for that parameter. The predictions obtained from FE linearized buckling analyses are much more accurate, predicting the collapse typically within 10% of the observed value.

Specific and Total Impulse

When evaluating the damage potential of a pressure wave, the impulse delivered by the pulse is often just as if not more important than the peak pressure at which it is delivered [24]. This is because the impulse combines the effect of both pressure magnitude and the duration of that pulse, which heavily influences the response of a structure to that pulse. For this reason, the specific impulse of the local pressure history is calculated for each specimen type. Here, the specific impulse delivered up to an arbitrary time, t , is defined simply as [24]:

$$I = \int_0^t \Delta p dt \quad (2)$$

where Δp is the dynamic pressure at time t . To form a better means of comparing impulses between specimens with different collapse pressures, a normalized impulse is defined as follows:

$$\bar{I} = \frac{\int_0^t \Delta p dt}{\int_0^t p_0 dt} \quad (3)$$

Where P_0 is the hydrostatic pressure during the collapse event.

Results and Discussion

Specimen	P_{cr} (MPa)	Minimum Pressure, P_{min} (MPa)	Underpressure Duration (ms)	Normalized Negative Impulse, \bar{I}	Potential Hydrostatic Energy (J)
CT	0.73 [± 0.01]	0.45 [± 0.04]	5.727 [± 0.162]	0.083 [± 0.004]	926.4 [± 0.4]
CTRD	1.61 [± 0.09]	0.98 [± 0.07]	2.580 [± 0.122]	0.123 [± 0.004]	1284 [± 93]
RC	0.75 [± 0.06]	0.25 [± 0.05]	4.568 [± 0.209]	0.057 [± 0.003]	961 [± 86]
BC	1.83 [± 0.10]	1.23 [± 0.07]	2.318 [± 0.244]	0.405 [± 0.038]	2402 [± 22.6]

Table 2: Impulse and energy parameters of studied specimens, 95% confidence interval in brackets

Large Diameter Filament-Wound Specimens (CT)

The larger diameter CT specimens failed violently at approximately 0.73 MPa. These tubes buckled in a mode 3 shape, collapsing completely during the failure process then rebounding to a roughly cylindrical shape following the release of pressure. The averaged local pressure trace

about the midspan of the specimen at a standoff distance of 48.3mm is shown in Figure 5, and high-speed images as well as DIC generated displacement and velocity contours corresponding to key points on the trace are seen in Figure 6.

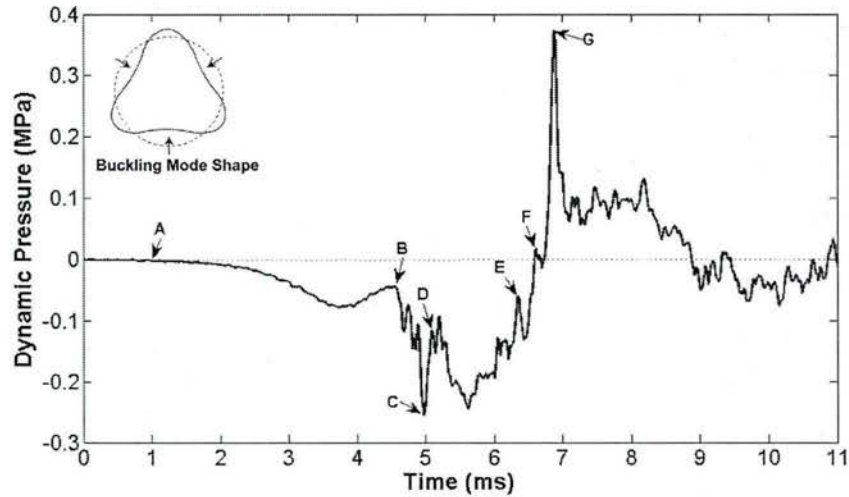


Figure 5: Local pressure history and buckling mode shape about midspan of CT specimens

Before the start of the rapid and unstable collapse of the structure, a significant amount of slow, quasi-static deformation is measured by DIC. For CT tubes, this initial ovaling amounts to - 4.31mm (11% of the tube radius), a very significant amount of deformation which may serve as an early warning of implosion risk. To focus on the deformation of solely the dynamic event, DIC displacement contours have been adjusted to subtract this initial deformation out. In other words, the presented DIC results represent deformation from an arbitrary time after the initial ovaling, but before the dynamic event. This convention is followed for all specimens studied. As the collapse initiates, the local pressure about the midspan decays somewhat smoothly for about 4.5ms, from time A to time B. By examining the correlated images for this period, it is seen that this pressure decays corresponding with the buckling of the tube in a mode 3 shape, without

visible damage. At time B, a longitudinal crack is observed on the bottom visible lobe of the structure, pursued immediately by a small amount of cavitation on that surface. This is followed by an abrupt drop in local pressure, caused by increased acceleration due to the loss of structural stability in that region brought on by cracking. The local pressure continues to fall until it reaches a minimum at time C. At this instant, it is observed that surface cavitation has intensified, reflecting this drop in pressure. A sudden increase in velocity magnitude is also seen at time C, increasing from $\sim 4\text{m/s}$ at time B to $\sim 10\text{m/s}$ over a period of 0.5ms , demonstrating the sudden loss of stability brought on by longitudinal cracking. Following the minimum pressure, a sudden spike in pressure is seen at time D. This spike is relatively large, $\sim 0.15\text{MPa}$, and has not been observed in previous implosion studies on homogeneous materials. The cause of this peak can be found by comparing images at C and D. In image C, as previously discussed, the bubbles formed by surface cavitation are at their maximum size. In image D, all visible bubbles have vanished. Between these two images, the surface cavitation bubbles collapse inward upon themselves and the surface on which they reside. The collapse of such bubbles has been well documented as resulting in large pressure pulses [26], and is therefore the cause of the observed spike at time D in the local pressure trace. It should be noted that no DIC contours are available after time D, as large scale damage to the surface of the specimen caused destruction of the speckle pattern and subsequently loss of correlation.

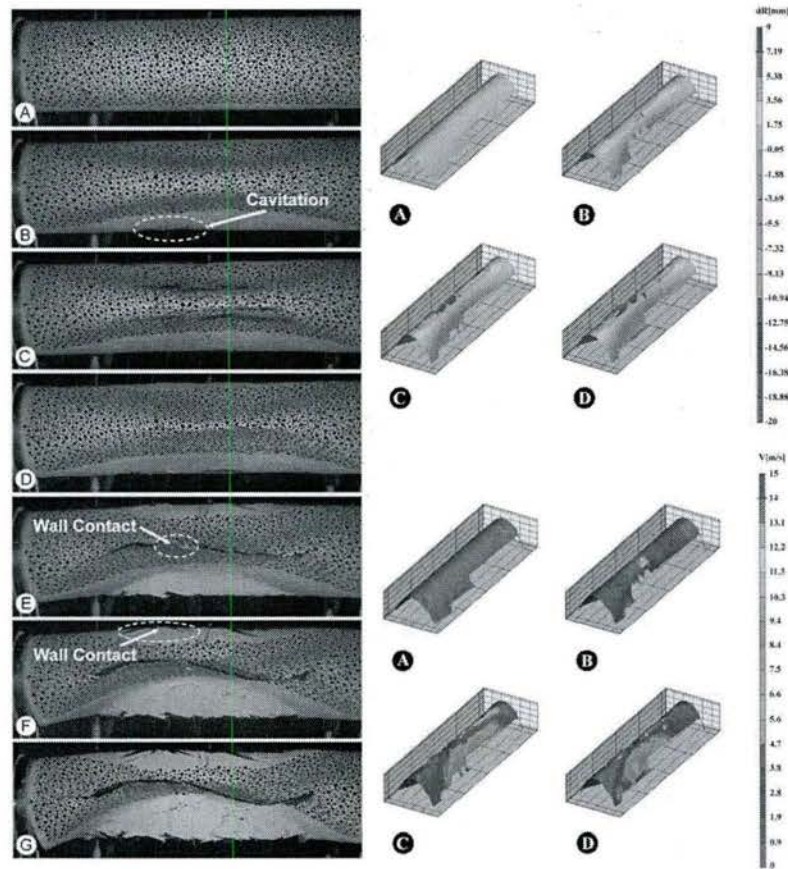


Figure 6: High-speed photographs (left) and DIC contours of radial displacement (top-right) and velocity (bottom-right) for CT specimens

Near the end of the underpressure region of the pressure history, two small yet distinct peaks can be seen at times E and F. These peaks are analogous to those seen in the implosion of aluminum tubes [8,9] and are indicative of wall-to-wall contacts at the center of the structure. The reason that multiple wall contacts are seen in this case is that the structure buckles in a mode 3 shape, and the non-homogenous nature of the material may cause two lobes to contact slightly before the third makes contact. Looking at the corresponding images E and F, wall-to-wall contacts are indeed seen as indicated by arrows.

After the walls contact, the collapse of the structure is abruptly halted. This causes the surrounding fluid, which accelerated inward with the surface of the structure, to rapidly decelerate. This drastic change in momentum causes the release of a high magnitude pressure pulse, observed in the pressure history at time G. Following this pulse is a broad region of overpressure as the buckling propagates through the length of the tube. Here it is seen that the tube has closed completely in the circumferential direction assuming a mode 3 buckling shape. After this point, longitudinal buckling waves develop from the applied axial compression imparted by hydrostatic pressure in conjunction with the loss in structural integrity from accumulated damage.

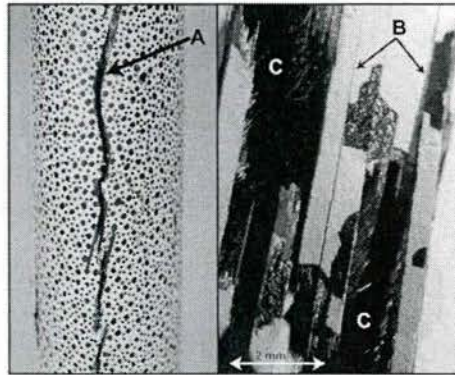


Figure 7: Post-mortem images of CT specimens, showing (A) through-thickness longitudinal cracking, (B) interfibrillar cracks, and (C) fractured fibers.

Post-mortem images of CT specimens, shown in Figure 7, give a clearer view of the types and scales of damage incurred on the structure. These images clearly show that the dominating mode of failure is nearly exclusively three longitudinal cracks, marked as "A", spaced at approximately 120° corresponding with the lobes of the mode 3 buckling shape. While some small amount of

circumferential cracking is observed in the vicinity of these larger cracks, they are relatively minor in comparison. Additionally, the tube is seen to regain much of its original shape, and no significant delamination is observed. Optical microscopy of the fracture surfaces show the major cracks are aligned parallel with the fiber angle of the outer ply, $\pm 15^\circ$ from the length axis, denoted by "B" in the figure. This implies that these cracks initiated in regions of high tensile stress in the outer ply, and propagated through the relatively weak, resin-rich interfibrillar region parallel to the reinforcing fibers. Fractured fibers in underlying plies are also seen in this micrograph, denoted as "C" in the figure. The fracture surfaces of these plies are also parallel to the $\pm 15^\circ$ outer ply, showing that the cracking initiated in the outer ply retains its original orientation as it propagates through the shell thickness. Additionally, the observed visible fibers appear very short, and protrude a fairly small distance from the fractured matrix. This shows that the failure of the laminate was quite brittle, with very little fiber pull-out present.

Reduced Diameter Filament-Wound Specimens (CTRD)

The smaller diameter filament-wound CTRD specimens at 1.60 MPa. Interestingly, both of these specimens appear to initiate a mode 3 collapse shape, then reduce to a mode 2 shape as the implosion progresses and the tube flattens. As with the larger specimens, the tubes return to a roughly cylindrical shape following depressurization. The averaged local pressure trace about the midspan of the specimen at a standoff distance of 48.3mm is shown in Figure 8, and high-speed images as well as DIC generated displacement and velocity contours corresponding to key points on the trace are seen in Figure 9.

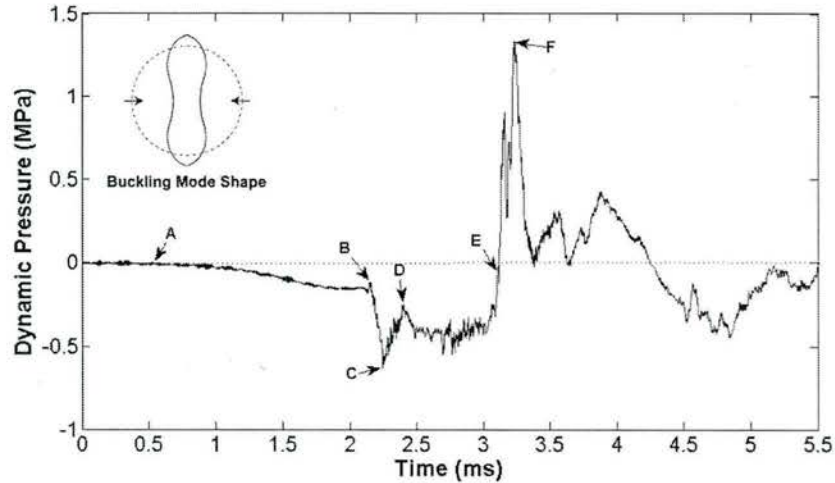


Figure 8: Local pressure history and buckling mode shape about midspan of CTRD specimens

CTRD specimens also experience some initial quasi-static deformation, though it is significantly less than CT specimen, amounting to only -1.02mm (3% of tube radius). The reason for this difference is the increased structural rigidity of these specimens brought on by reduced diameter and increased thickness-to-radius ratio. The collapse and resulting local pressure history for CTRD specimens is quite similar to that of the larger diameter filament-wound tubes previously discussed. A relatively smooth drop in pressure is observed between times A and B (~1.5ms) as the tube begins to collapse in a mode 3 shape as seen in the corresponding high-speed images. Over this period, the tube is seen to be collapsing with a velocity of ~8.75 m/s in DIC contours, significantly faster than CT specimens. At time B in the pressure profile, a small sharp peak is seen followed by a rapid drop in pressure. Similar to CT specimens, this corresponds to the appearance of a longitudinal crack (see Figure 9.B) causing the loss of structural stability which in turn allows the speed of collapse to increase greatly. In fact, immediately after through-thickness cracking, at time C, a large region of significantly higher velocity, ~14 m/s, appears in the vicinity of the crack. This rapid increase in fluid velocity results in an equally rapid drop in

pressure, and the pressure continues to fall steeply to a distinct minimum at that time. At this point, the pressure at the surface of the structure has fallen low enough to cause cavitation, as highlighted in the corresponding image in Figure 9. At time D, the pressure rises to a relatively small peak. Examining high-speed images shows that cavitation bubbles have vanished at this time, indicating that this peak is a result of a pressure pulse emitted from the collapse of the bubbles. The underpressure region continues until time E when a sharp peak is observed. This peak corresponds to the wall-to-wall contact at the completion of the collapse, as previously discussed, and is shown in the matched high-speed photograph. As was the case with CT specimens, damage on the surface of the structure causes loss of DIC correlation after this time

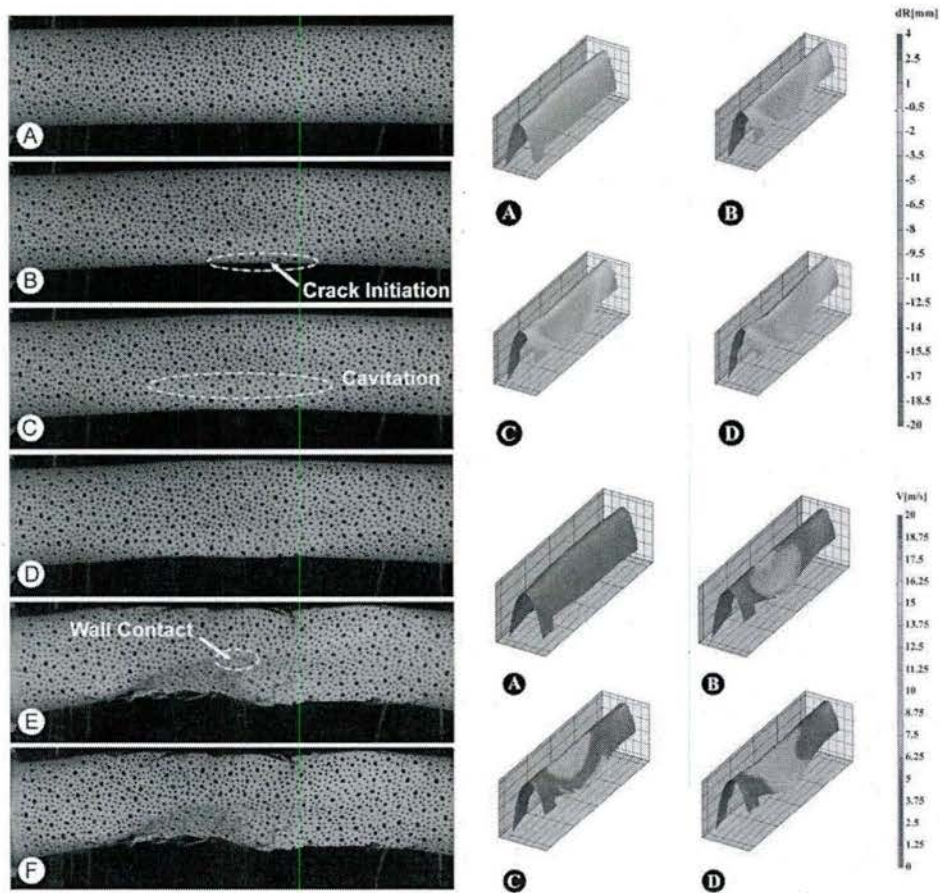


Figure 9: High-speed photographs (left) and DIC contours of radial displacement (top-right) and velocity (bottom-right) for CTRD specimens

This wall-to-wall contact is followed by a high magnitude pressure pulse and a broad region of overpressure as the entirety of the structure collapses. At image F, the tube has fully collapsed circumferentially in a mode 2 shape and after this time the buckle propagates rapidly through the length of the structure.

Post-mortem images of CTRD specimens are included in Figure 10. Much like the larger diameter CT specimens, longitudinal cracking, marked as "A" appears to be the chief mode of failure, however damage is considerable more severe for these tubes. It is seen in these images that through-thickness, longitudinal cracks have completely separated the structure. In addition, the damage appears somewhat less localized to the major cracks, implying a significantly more catastrophic collapse than for larger diameter specimens. Optical microscopic images of the fracture surface show a great deal of interfibrillar cracks branching off of the critical longitudinal cracks, marked as "B", showing these specimens exhibited more energy intensive damage and failure. As these specimens collapsed at a significantly higher pressure than the larger diameter CT specimens, more potential energy was available at the time of collapse. This increased energy resulted in a much more catastrophic collapse and caused the more severe state of damage observed in the post mortem photographs.

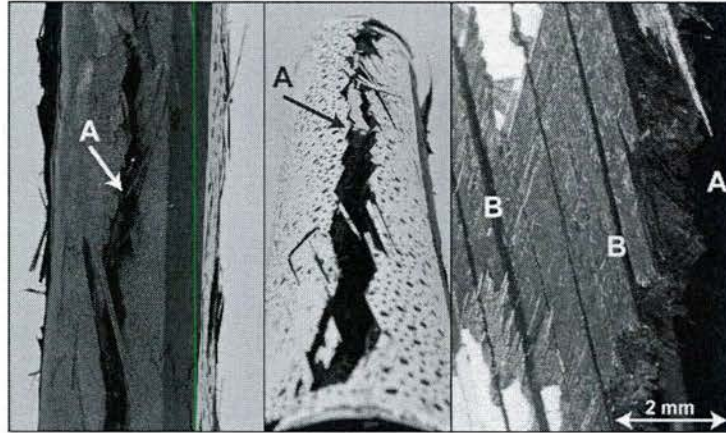


Figure 10: Post-mortem images of CTRD specimens showing: (A) through-thickness longitudinal cracking, and (B) interfibrillar cracking

An interesting feature of CTRD post-mortem specimens is the existence of three longitudinal cracks, spaced at approximately 120° , implying a mode 3 collapse though high-speed images showed a flattened mode 2 collapse shape. As previously mentioned, the collapse of these tubes initiated in a mode 3 shape, causing the formation of three buckle lobes. Longitudinal cracks formed in each of these lobes as in CT specimens, however the resulting loss of structural stiffness in this case caused the reduction of the collapse shape to mode 2. In this way, these specimens were able to exhibit evidence of both mode 3 and mode 2 buckling.

Roll-Wrapped Specimens (RC)

The RC specimens collapsed in a mode 3 buckling shape at 0.75 MPa. The averaged local pressure trace about the midspan of the specimen at a standoff distance of 40.6mm is shown in Figure 11, and high-speed images as well as DIC generated displacement and velocity contours corresponding to key points on the trace are seen in Figure 12. For these specimens, correlation is maintained nearly through the entirety of the collapse.

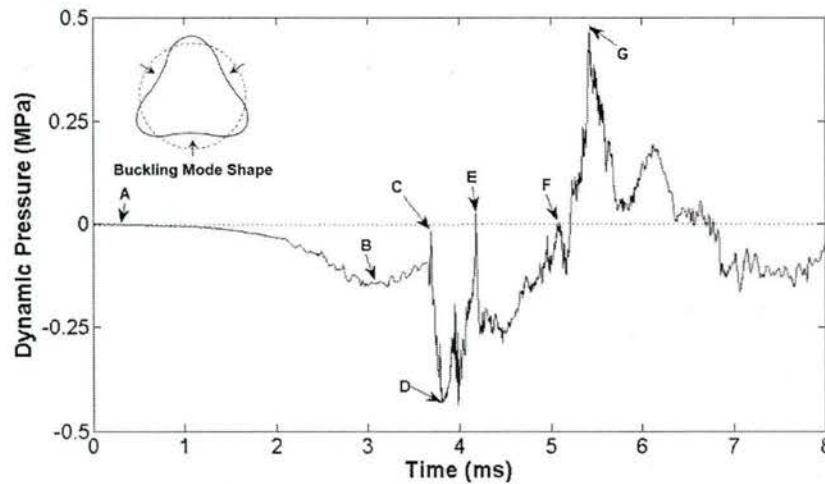


Figure 11: Local pressure history and buckling mode shape about midspan of RC specimens

RC tubes experience quasi-static ovaling of -2.61mm (7% of tube radius) prior to the dynamic implosion event. This is significantly less than seen in filament-wound tubes of the same diameter, mainly due to the enhanced directional stiffness of these specimens as significantly more fibers are oriented along the major axes of the tube. The collapse of these tubes show many similarities to the filament-wound specimens discussed previously. Initially, the local pressure decays rather smoothly up until time B as the structure deforms into a mode 3 shape. At time B, longitudinal cracks are seen to emerge on the apex of a visible buckling lobe, as indicated in the corresponding photograph. However, these cracks do not compromise the structural integrity of the tube significantly at that time as they are simply surface cracks that do not completely penetrate the walls of the tube. The local pressure then rises somewhat until a sharp peak is observed at time C. This corresponds with the opening of cracks as marked in image C in conjunction with the onset of cavitation on the surface of the structure. Following this occurrence, the pressure drops sharply to a minimum at time D. This implies that at time C, the cracks previously formed propagate through the thickness of the tube walls, causing a sudden

loss in stability and rapidly accelerating the collapse. This is reinforced by examining DIC contours at time D, where a region of high velocity ($\sim 14\text{m/s}$) appears adjacent to the buckling lobe, increasing from a relatively moderate velocity of 5 m/s in the previous image at time C.

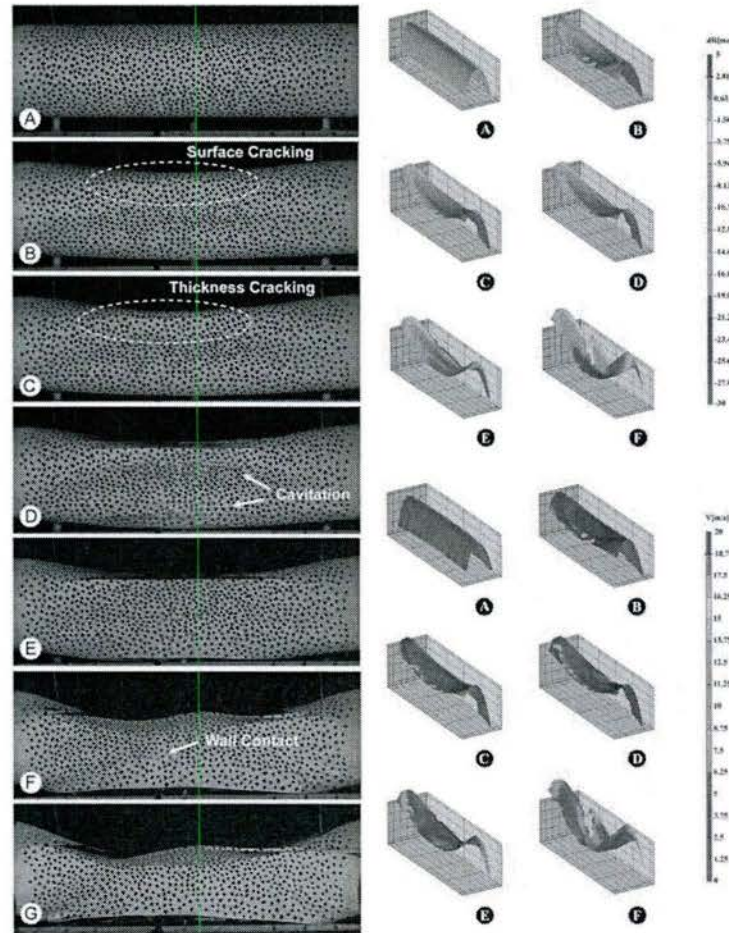


Figure 12: High-speed photographs (left) and DIC contours of radial displacement (top-right) and velocity (bottom-right) for RC specimens

The crack itself releases an acoustic pulse seen at time C and the rapid acceleration of the surrounding fluid manifests in the sharp drop in pressure observed. At time D where pressure is at a minimum, the cavitation bubbles which initiate at time C are seen to be at their maximum

size in the matching image. After this time, those bubbles collapse in on themselves, resulting in the release of a pressure wave observed at time E. It should be noted here that the pressure pulse from the collapse of cavitation bubbles is of significantly greater magnitude for roll-wrapped tubes than for any other architecture, relative to the collapse pressure. This is due to the increased size of cavitation bubbles for these specimens, which resulted in more available energy to be released upon collapse.

The underpressure region continues as the tube collapses inward until time F. At this time, the tube is seen to make wall-to-wall contact (see image in Figure 13) and a small spike in local pressure is observed. DIC velocity contours show regions of zero velocity on the interior of the viewed buckled valley, reinforcing the claim of wall contact at that time. Following wall contact a high magnitude pressure pulse is measured at time G as the surrounding fluid is arrested in an identical manner as the previous two cases. The collapse shape continues then to propagate axially until the entire structure fails. Through-thickness longitudinal cracks are observed through the entire specimen length which caused the separation of the tube into several pieces.

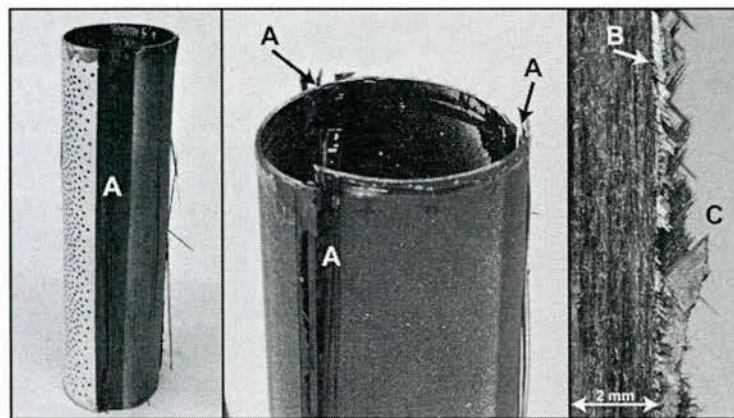


Figure 13: Post-mortem images of RC specimens showing: (A) through-thickness longitudinal cracking, (B) delamination of 0° fiber bundles, and (C) fractured fibers

Post-mortem images of RC specimens are included in Figure 13. Similar to the previous specimens, due to the mode 3 collapse shape, the most prominent damage feature is longitudinal cracking, marked as "A", with three through-thickness cracks located at 120° intervals about the circumference. Like CT tubes, this damage is fairly localized to said cracks, with only small amounts of circumferential cracking. However, unlike the previous two cases, there is also a good deal of delamination of tows in the outer longitudinal ply, marked as "B". Because these tows were parallel to the direction of the major cracks along their entire length, they simply separated from the laminate via matrix cracking rather than fracturing the actual fibers as in the case of angled plies. Optical microscopy of the fracture surface show that internal angle plies experience fiber fracture, marked as "C" parallel to the fiber angle of the outer ply, with relatively small amounts of fiber pull-out. This reinforces the assertion that cracking initiates in the outer ply in the weak interfibrillar region and retains its original orientation as it propagates through the thickness of the laminate.

Braided Specimens (BC)

In both tests of BC tubes, the specimens fail very rapidly at 1.81 MPa, and in both cases, the collapse is so violent that the tube tears free of the sealing end caps and falls from the support structure. In these cases, the collapse mode is an imperfect mode 2 shape, with one wall drawn in toward the other, analogous to an indentation. The averaged local pressure trace about the midspan of the specimen at a standoff distance of 41.0mm is shown in Figure 14, and high-speed images as well as DIC generated displacement and velocity contours corresponding to key points on the trace are seen in Figure 15.

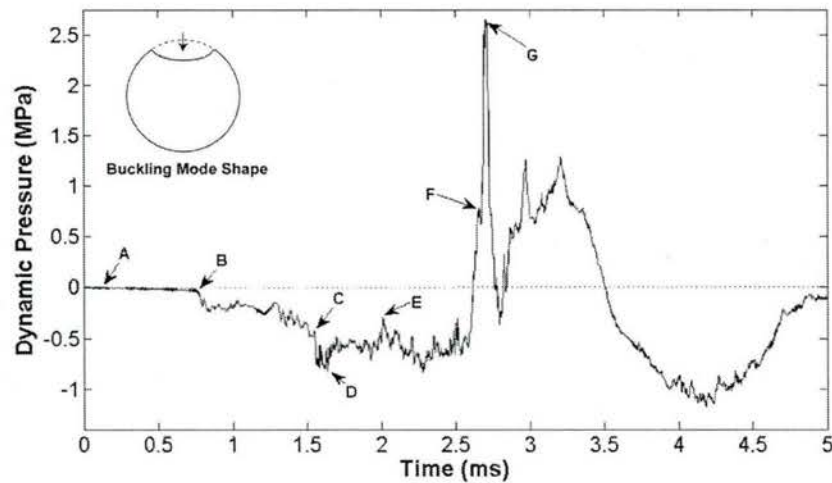


Figure 14: Local pressure history and buckling mode shape about midspan of BC specimens

Braided specimens show the least quasi-static ovaling of all 76.2mm diameter specimens, amounting to -1.39mm (2.6% of tube radius). This shows that braided tubes give the least "warning" before undergoing catastrophic failure. From time A to B, little change is noted in the pressure trace. Similarly, only a small degree of buckling is noted in the high-speed photographs as the tube begins to "oval" slightly. Likewise, very little change is seen in velocity and displacement contours between these times. Following time B, the collapse intensifies as the wall facing the cameras is drawn inward toward the center of the implodable. Pressure then drops fairly slowly until time C, at which point through-thickness cracks are seen to appear in the corresponding high-speed image. It is interesting to note that the structure does not buckle inward with a single smooth valley, but instead with two distinct local indentations as is highlighted by the displacement contour at time C. This phenomenon is a result of axial imperfections in the thickness of the tube walls. Some regions along the length axis of the specimen are somewhat thicker than others, and those regions act as ring stiffeners, inhibiting buckling at that point. This will in turn result in local buckling valleys to form on either side of

the thicker region, which will grow until they can overcome the natural stiffener and coalesce into the more typical global buckling shape. This has the effect of increasing buckling resistance of these materials by raising the critical collapse pressure.

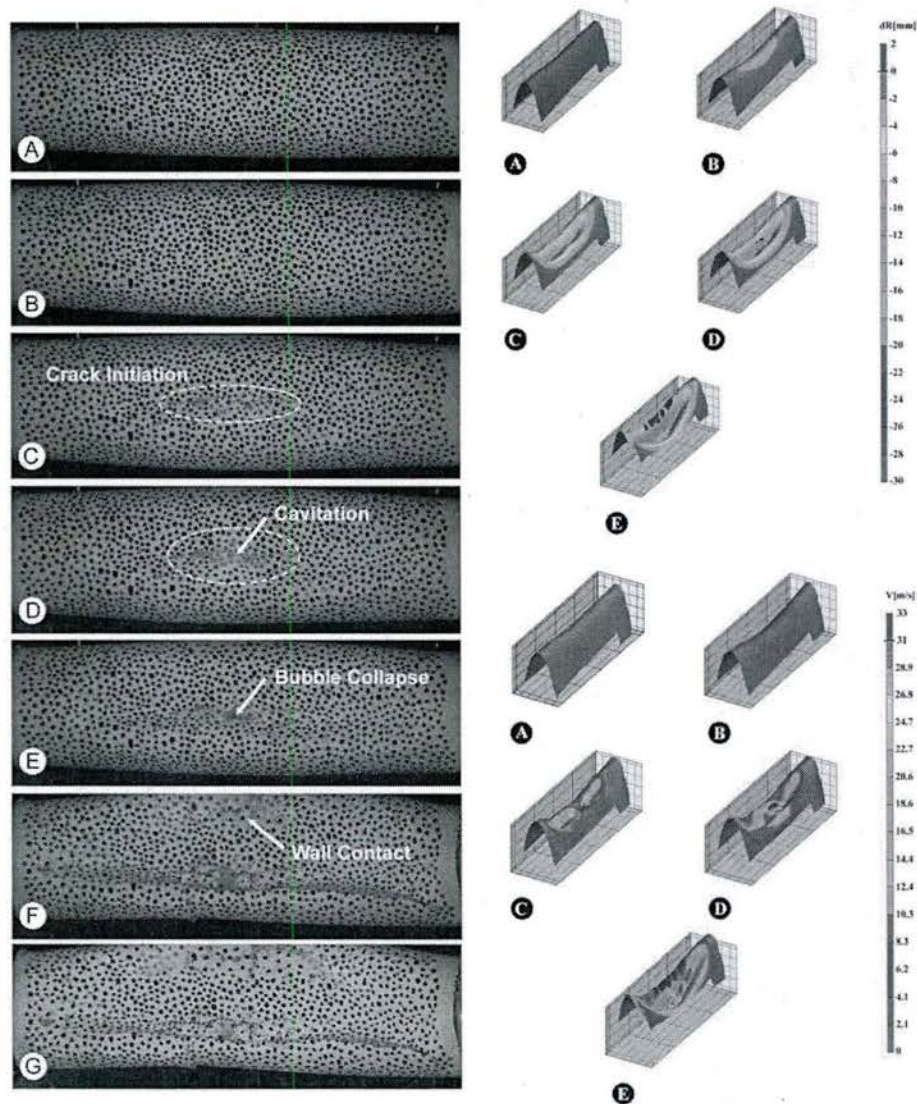


Figure 15: High-speed photographs (left) and DIC contours of radial displacement (top-right) and velocity (bottom-right) for BC specimens

The cracking results in a loss structural integrity, allowing the wall to accelerate rapidly inward and drop local pressure to a minimum at time D. Here only one larger buckling valley is seen, and the velocity across the surface has reached an apex at the center of the buckling valley of ~ 33 m/s. This high velocity causes a very significant drop in local pressure, explaining why the pressure reaches a minimum at this time. Also as a result, the cavitation bubbles initiated in the previous time have reached their maximum size as seen in image D. After reaching a critical size, these bubbles collapse in on themselves, resulting in the release of a pressure pulse observed at time E. Studying the image at this time, it is seen that the cavitation bubbles have collapsed completely in the region indicated by the arrow. The contours corresponding to time E show the further growth of the buckling shape, however due to cracking much data is lost especially at the center of the buckling valley, and after this time correlation is lost nearly completely.

The wall of the tube continues to deform inward until time F, at which point wall-to-wall contact is made at the point indicated by the arrow in the high-speed image. This event is accompanied by a small, sharp peak in pressure, typical of wall-to-wall contact. Identically to the previous specimens, the pressure then rises to a distinct maximum as the surrounding fluid is arrested following this contact. This is followed by a broad overpressure region as the collapse propagates axially, after which the local pressure is seen to oscillate about the hydrostatic value.

One of the starkest differences between the pressure history of the braided tubes and all other specimens is the lack of a region of gradual pressure decay. As discussed, the local pressure remains relatively constant in the initial stages until a sharp drop is seen at time B. This is a result of the deformation behavior characteristic of braided composite tubes. When braided tubes are loaded in tension, interlaced fiber tows attempt to "scissor" and straighten out. The tows then

reach a point where the matrix material prohibits scissoring, causing them to "lock-up" and result in significant stiffening and ultimately brittle and catastrophic failure [27]. Though the loading of the tube in this case is biaxial compression, as the structure buckles some regions in fact experience tension due to bending of the tube walls. Because of this feature of braided reinforcements, the initially smooth deformation seen in filament-wound and roll-wrapped composites is largely eliminated, so that when the structure does fail, it does so abruptly and catastrophically. This is also the reason why the initial, gradual deformation in these structures is minimal in comparison to the other fabric architectures. The abrupt onset of the underpressure region for these specimens is quite similar to those observed by Turner in the case of imploding glass tubes [28]. This reinforces the assertion that these tubes fail in a brittle fashion because the initial stages of the pressure history are characteristic of such a failure.

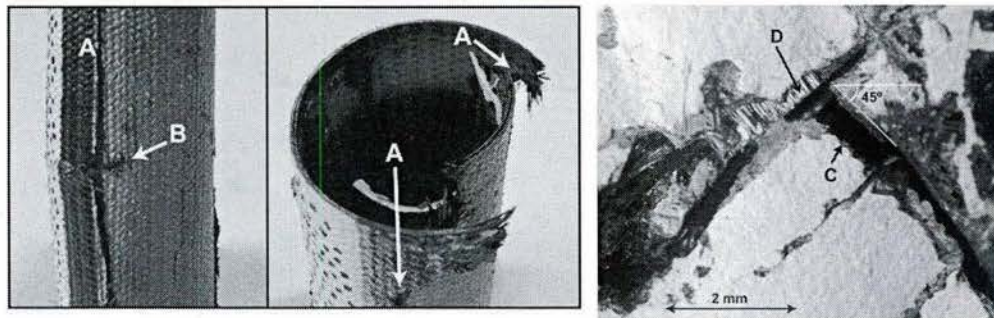


Figure 16: Post-mortem images of BC specimens showing: (A) longitudinal cracking, (B) circumferential cracking, (C) fractured matrix material, and (D) fractured fibers

Post-mortem images of BC specimens are included in Figure 16. As with all previously studied tubes, longitudinal cracking at the lobes of the buckling shape, marked as "A", dominate the failure of the tube. However, since these tubes failed in a mode 2 shape rather than mode 3, there exist only two longitudinal cracks, separated by approximately 180°. BC tubes also show

considerably more circumferential cracking found predominantly about the midspan of the specimens, marked as "B" in the image. This can likely be attributed to the very brittle nature of the collapse of these tubes, which allowed for a more aggressive failure and consequently greater accumulation of damage. Optical microscopy in Figure 16 gives additional insight on the failure of braided specimens. In this image, cracks are seen through the thickness of the tube, oriented parallel with the reinforcing fibers, at 45° to the length axis and marked as "C". Similar to previously discussed observations, this shows that cracks initiated and propagated in the weak, resin-rich interfibrillar regions parallel to the fiber reinforcement. Some exposed fibers are seen on the fracture surfaces, marked as "D", however those fibers protrude only a short distance, showing the absence of fiber pull-out and reinforcing that the through-thickness brittle fracture dominated the failure of BC specimens.

Pressure History Parameters

It is informative to compare the extreme values of local pressure attained by each sample to determine the effect of reinforcement and geometry on those values. However, due to the relatively slow nature of the collapse of these tubes, reflections of the initial underpressure wave may in fact reflect back from the walls of the pressure vessel and artificially reduce the magnitude of some parts of the observed overpressure. As a result, the true magnitude of the pressure peak may be somewhat obscured and reduced. Therefore, this discussion will focus solely on the quantities associated with underpressure region itself. For the specimens discussed in this study, the dynamic portion of the underpressure regions are quite short in duration, and so any reflections of the initial, gradual portions of the underpressure would be negligible in magnitude. Because of this, the magnitude of the underpressure region and other parameters associated with this region may be quantified with confidence.

The minimum gage pressures of the local pressure history, normalized by hydrostatic collapse pressure, are compared for all specimens in Figure 17. Here it is useful to study minimum pressures in terms of dynamic pressure as a percentage of hydrostatic pressure as the collapse pressures varied between specimen types.

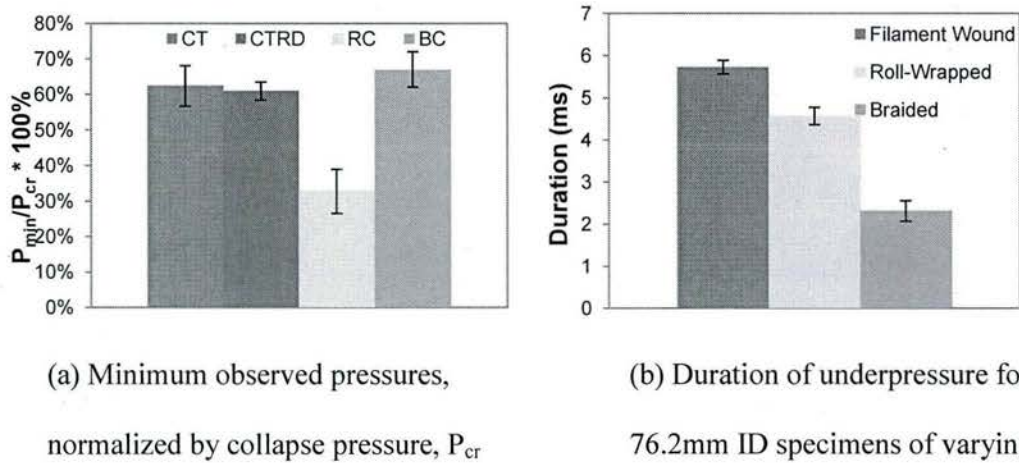


Figure 17: Quantitative parameters related to the underpressure region of the pressure history

It is first observed that all filament-wound and braided specimens reached approximately the same minimum pressure, experiencing a pressure drop of 65% of hydrostatic collapse pressure. In contrast, roll-wrapped tubes reached minimum pressures of 32% of hydrostatic pressure, half that of the other specimens. Because the majority of reinforcements are oriented along the length axis of the roll-wrapped specimens, they are less able to resist the collapse of the structure. This caused less energy to be dissipated in damage during collapse, allowing for greater collapse speed and consequently lower minimum pressure. This also explains why the intensity of cavitation is greatest for roll-wrapped tubes, as the lower pressure created a more favorable environment for this phenomenon.

It is also useful to compare the temporal aspects of the pressure histories for specimens of the same inner diameter. This can give some additional insight on differences in collapse speeds between tubes. The durations of the underpressure regions of the local pressure history are compared for specimens of varying reinforcement architecture in Figure 17.

First it is evident that filament-wound tubes possess the longest suction region of the pressure trace, while braided tubes have the shortest. As the suction region is caused by the collapse of the structure itself, this implies that braided tubes collapse significantly faster than other specimens, and filament-wound tubes significantly slower. Braided tubes collapse with greater speed due to the catastrophic nature of their failure, as previously discussed. It is also important to note that roll-wrapped specimens also had a shorter duration of underpressure than filament-wound tubes. Because the roll-wrapped tubes contain less angle-ply, there is less bridging of the characteristic longitudinal cracks and, consequently, less resistance to deformation.

Impulse

As discussed in the previous section, the relatively long duration of the collapse events leads to some reduction of the overpressure region via reflections of the underpressure wave from the tank boundaries. This in turn would result in the underestimation of the impulse delivered by the pressure wave, and would cause the magnitudes of the impulse of the underpressure and overpressure regions to not be equal, contrary to previous experimental observations [8,9]. This means that the impulse delivered by the overpressure pulse, an important quantity in evaluating damage potential of the wave, may not be accurately measured directly from the pressure history. To overcome this limitation and gain a means to accurately quantify the positive impulse, the fundamental physics involved in this problem are used to show that the negative impulse may be

used to indirectly estimate the positive impulse. First, refer to the definition of particle velocity in a dynamic pressure field, given as [17,25]:

$$u = \frac{\Delta p}{\rho c_0} + \frac{1}{\rho R} \int_0^t \Delta p dt \quad (4)$$

where Δp is the dynamic pressure observed at a standoff distance, R , ρ is the fluid density, and c_0 is the wave speed of the medium. At a certain time, t , after the passing of the shockwave, dynamic pressure and particle velocity will both return to zero. For this to be true, the following condition is required:

$$\int_0^t \Delta p dt = 0 \quad (5)$$

In other words, the net impulse across the entire event must be zero. This in turn implies that the negative impulse of the underpressure region should be equal in magnitude to the positive impulse released in the overpressure region. This phenomenon has been observed in several studies on the implosion of glass spheres as well as the implosion of aluminum tubes [4,8,17]. Therefore, in the present study the impulse of the underpressure region is calculated, and it is assumed that its magnitude will be equivalent to that of the impulse released in the pressure pulse.

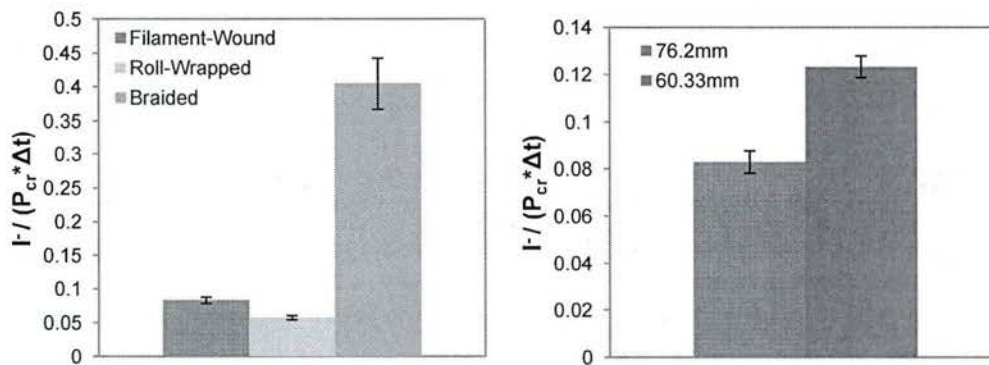


Figure 18: Normalized impulse for 76.2mm tubes of different reinforcement (left) and for filament-wound tubes of varying diameters (right)

The normalized impulse, as previously defined, delivered in the collapse of specimens with varying reinforcement architecture is compared in Figure 18(a). This plot shows that the pressure wave released in the collapse of braided carbon composite tubes possesses a drastically higher impulse than either filament-wound or roll-wrapped tubes. The reason for this is believed to be the stiffening followed by rapid, brittle failure of braided reinforcements as previously discussed. This allows for a greater and more rapid change in momentum to be imparted on the surrounding fluid, resulting in a pressure pulse with greater impulse.

Figure 18(b) compares the normalized impulse measured in the collapse of filament-wound tubes with different diameters. Here it is noted that the normalized impulse for the smaller diameter specimens is 50% greater than that of larger diameter specimens. This difference is likely due to the change in buckling mode shape brought on by the reduction of diameter. This allowed for a significantly greater collapse speed and extent of collapse resulting in greater momentum change in the surrounding fluid and, consequently, a greater magnitude of impulse.

Surface Cavitation

As mentioned earlier, one aspect that made the collapse of these materials particularly unique from previously published work is the presence of cavitation on the surface of the structures, as emphasized in the image in Figure 18 for a braided tube specimen. Cavitation is a known phenomenon in which a fluid subjected to sufficiently low pressure generates voids or bubbles [27,29]. These bubbles are formed as a result of vaporization of the fluid itself and/or expansion of diffused gases in the fluid. In these experiments, bubbles grow in regions of maximum

velocity, as the local fluid pressure will be a minimum in that region. Figure 19 shows a magnified image of a cavitation bubble on the surface of a BC specimen. Bubble growth progresses until a critical size is reached, after which the bubbles become unstable and collapse inward on themselves. For each pressure trace for all specimens, there are distinct pressure spikes in the underpressure region coinciding with the collapse of bubbles on the specimen surface. It is well known that the collapse of cavitation bubbles against a structure result in very high magnitude pressure pulses due to micro-jet formation, therefore giving some justification to these observed peaks [27,29].

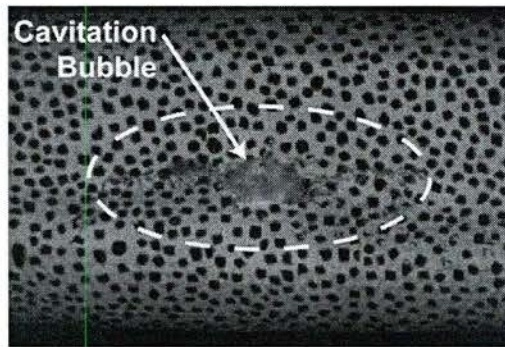


Figure 19: Presence of cavitation on the surface of a typical BC specimen during implosion

Cavitation is ubiquitous in the implosion of these materials due to the specific mechanisms of progressive damage unique to laminated composites. The implosion of homogenous metallic tubes is characterized by a smooth, fairly uniform deformation into the assumed collapse mode. This is reflected in the underpressure region of the pressure history for those materials which is quite smooth up until wall contact is made. This is certainly not the case for the composite tubes in this study. As previously discussed, due to the particular damage and failure mechanisms of each, all specimens eventually suffered a sudden onset of high-velocity collapse due to cracking and loss of structural stiffness at which time cavitation occurred.

A more thorough explanation of the rapid acceleration seen in filament-wound and roll-wrapped tubes is found in the layering of lamina of different fiber orientation. As the collapse initiates, the structure begins to deform into a certain buckling shape characterized by a number of lobes and valleys. As deformation increases, longitudinal cracks are formed at the apex of the lobes where tensile stress is high. In fiber reinforced laminas, the crack will grow most easily in the resin rich area between fibers or on the fiber/resin interface itself where resistance to that crack growth is minimum, and these cracks may grow relatively stably as the collapse continues (see illustration in Figure 20). This is reflected in the initial gradual decay seen in the pressure profile. As the crack continues to grow through the thickness, it encounters a ply of opposite fiber orientation. The fibers of this ply are able to effectively bridge the crack, providing added resistance to its growth and thereby the collapse of the structure. This results in a small deceleration of the structure, which is reflected in the small recovery in pressure seen in the pressure traces at the end of the region of smooth decay (time B for CT and CTRD specimens, time C for RC specimens). The deformation of the structure continues until the resistance of crack growth provided by the bridging fibers is overcome and the crack propagates unstably through the thickness of the tube. This results in a sudden loss of structural stability and causes the specimen to rapidly accelerate inward. This sudden and drastic increase in velocity greatly lowers local pressure at the specimen surface and manifests in the observed cavitation phenomenon.

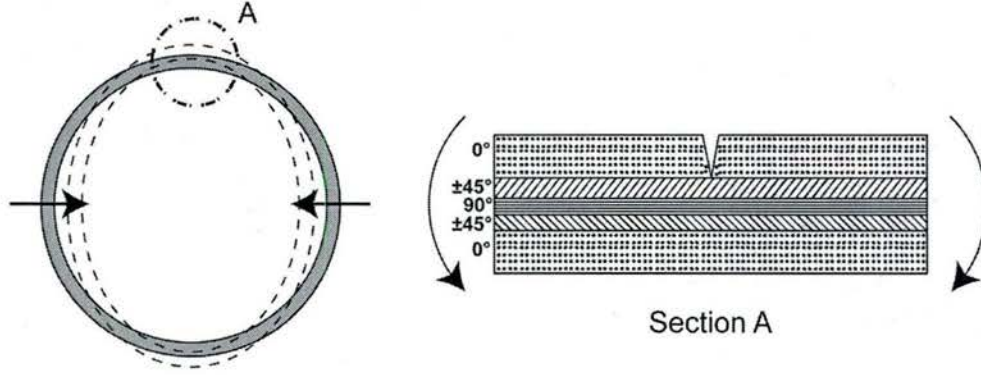


Figure 20: Growth of through-thickness crack in layered composite tubes

This occurrence is further analyzed using the cavitation number. Cavitation number is a dimensionless Euler number relating pressure difference and kinetic energy at a given time in the pressure history, and is defined as:

$$\sigma = \frac{P_{\infty} - P_v}{\frac{1}{2}\rho v^2} \quad (6)$$

where P_{∞} is the far-field hydrostatic pressure, P_v is the vapor pressure of water, ρ is the fluid density, and v is the fluid velocity. Traditionally, this number is used to characterize the potential of fluid in a given flow to cavitate. While there is not a universal cavitation number that implies the onset of cavitation, the lower σ is, the greater the potential for cavitation to initiate or to intensify if already initiated [28].

This analysis seeks to identify an initiation cavitation number, σ_i , or the value of σ at which cavitation is seen to initiate. This value can then be compared between experiments to attempt to find a relationship between material types, dimensions, and cavitation. In every experiment performed on carbon-epoxy composites, cavitation occurred in the initial stages of collapse. However, in some of these experiments, correlation is lost prior to the initiation of cavitation,

preventing the capture of velocity at this time. Accurate initiation cavitation numbers are captured for five experiments, representing both filament-wound and roll-wrapped carbon/epoxy tubes, with 76.4mm and 60.325mm inner diameters. Cavitation is seen to occur in all specimens at roughly the same cavitation number, an average value of $23.6(\pm 1.5)$. Because this value holds for different fiber architecture, fiber alignment, and tube diameter, it is posited that this number is characteristic of the implosion of thin-walled carbon/epoxy tubes. This further suggests that the cavitation number is a valuable parameter to study the collapse of submerged structures along with the DIC technique as outlined previously.

Conclusions

The hydrostatic implosion of carbon/epoxy composite tubes is studied for specimens of varying reinforcement architectures and inner diameters. Using high-speed photography, DIC measurements, and dynamic pressure transducers, the progression of deformation and damage during collapse as well as the local pressure history throughout the implosion event is characterized for each specimen type. The completion of this study has resulted in the following pertinent conclusions:

- The hydrostatic implosion of carbon/epoxy tubes of varying reinforcement architecture and geometry results in the release of a potentially hazardous acoustic pressure pulse.
- The quantitative characteristics of the pressure pulse as well as the nature of the collapse itself are significantly affected by the architecture of reinforcing fibers and geometry of the tube.
- Rapid onset and propagation of through-thickness cracks cause sudden acceleration in the collapse event and result in surface cavitation. The collapse of these cavitation bubbles release additional pressure waves that may be observed in the near-field pressure history

and could potentially cause additional damage to the structure. Cavitation is seen to initiate at approximately the same cavitation number for all filament-wound and roll-wrapped specimens studied.

- Composite tubes with braided reinforcement released pressure waves with the greatest normalized impulse of all specimens studied, and also experienced the least quasi-static pre-deformation prior to implosion. This is a result of the enhanced brittle nature of the failure of these materials, and shows that they have a significantly greater potential to damage neighboring structures in the event of collapse.
- Filament-wound tubes with a large radius-to-thickness ratio are considered optimal for damage mitigation, as their collapse results in one of the lowest normalized impulses, and prior to their collapse they give the greatest "warning" through slow ovaling of the cross-section amounting to approximately 10% of the tube radius. Since this ovaling is elastic, the structure could be saved if pressure is relieved prior to reaching this level of deformation.

Acknowledgements

The authors would like to acknowledge the Office of Naval Research and Dr. Yapa D.S. Rajapakse for providing financial support to conduct this research under Grant No. N00014-10-1-0662.

References

[1] Mouritz AP, Gellert E, Burchill P, Challis K. Review of Advanced Composite Structures for Naval Ships and Submarines. *Compos Struct* 2001; 53(1): 21-42.

- [2] Urick RJ. Implosions as sources of underwater sound. *J Acoust Soc Am* 1963; 35: 2026–2027.
- [3] Orr M, Schoenberg M. Acoustic signatures from deep water implosions of spherical cavities. *J. Acoust. Soc. Am* 1976; 59: 1155–1159.
- [4] Turner SE. Underwater Implosion of Glass Spheres. *J Acoust Soc Am* 2007; 121: 844–852.
- [5] Accident grounds neutrino lab - physicsworld.com [WWW Document], n.d. URL <http://physicsworld.com/cws/article/news/2001/nov/15/accident-grounds-neutrino-lab> (accessed 2.10.14).
- [6] Ling J, Bishai M, Diwan M, Dolph J, Kettell S, Sexton K, Sharma R, Simos N, Stewart J, Tanaka H, Viren B, Arnold D, Tabor P, Turner S, Benson T, Wahl D, Wendt C, Hahn A, Kaducak M, Mantsch P, Sundaram SK. Implosion chain reaction mitigation in underwater assemblies of photomultiplier tubes. *Nucl Instrum Methods Phys Res Sect Accel Spectrometers Detect Assoc Equip* 2013; 729: 491–499.
- [7] Harben PE, Boro C. Implosion Source Development and Diego Garcia Reflections. Presented at the 23rd Department of Defense/Department of Energy Seismic Research Review, Jackson Hole, WY, 2-5 October 2001.
- [8] Turner SE, Ambrico JM. Underwater Implosion of Cylindrical Metal Tubes. *J Appl Mech* 2012; 80(1): 1-11.
- [9] Ikeda CM, Wilkerling J, Duncan JH. The Implosion of Cylindrical Shell Structures in a High-pressure Water Environment. *Proc of the R Soc A: Math, Phys and Eng Sci* 2013; 469: 2160

- [10] Moon CJ, In-Hoon K, Bae-Hyeon C, Jin-Hwe K, Choi JH. Buckling of Filament-wound Composite Tubes Subjected to Hydrostatic Pressure for Underwater Vehicle Applications. *Compos Struct* 2010; 92(9): 2241-251.
- [11] Ross CTF, Little APF, Haidar Y, Waheeb AA. Buckling of Carbon/Glass Composite Tubes Under Uniform External Hydrostatic Pressure. *Strain* 2009; 47: 156-174.
- [12] Smith PT, Ross CTF, Little APF. Collapse of Composite Tubes under Uniform External Hydrostatic Pressure. *J of Phys: Conference Series* 2009; 181: 156-157.
- [13] Hernández-Moreno H, Douchin B, Collombet F, Choqueuse D, Davies P. Influence of Winding Pattern on the Mechanical Behavior of Filament-wound Composite Tubes under External Pressure. *Compos Sci and Technol* 2008; 68(3-4): 1015-024.
- [14] Hur SH, Son HJ, Kweon JH, Choi JH. Postbuckling of Composite Tubes under External Hydrostatic Pressure. *Compos Struct* 2008; 86(1-3): 114-24.
- [15] Yang C, Pang SS, Zhao Y. Buckling Analysis of Thick-Walled Composite Pipe under External Pressure. *J Compos Mater* 1997; 31(4): 409-26.
- [16] Sutton MA, Orteu JJ, Schreier HW. *Image Correlation for Shape, Motion and Deformation Measurements: Basic Concepts, Theory and Applications*. New York, NY: Springer, 2009.
- [17] Gupta S, Parameswaran V, Sutton MA, Shukla A. A study of Underwater Implosion using Digital Image Correlation, *Proc of the R Soc A* 2014; 470(2172): 20140576.
- [18] Maalawi KY. Use of Material Grading for Enhanced Buckling Design of Thin-walled Composite Rings/long Tubes under External Pressure. *Compos Struct* 2011; 93(2): 351-59.

- [19] Rasheed HA, Yousif OH. Stability of Anisotropic Laminated Rings and Long Tubes Subjected to External Hydrostatic Pressure. *J Aerospace Eng* 2005; 18(3): 129-138.
- [20] Timoshenko SP, Gere JM. *Theory of elastic stability*. New York, NY: McGraw-Hill, 1961.
- [21] Von Mises R. The critical external pressure of cylindrical tubes under uniform radial and axial load, translated by D. F. Windenburg. *Stodolas Festschr* 1929: 418–430.
- [22] Koudela, KL, Strait LH. Simplified Methodology for Prediction of Critical Buckling Pressure for Smooth-Bore Composite Cylindrical Shells. *J Reinf Plast Compos* 1993; 12(5): 570-83.
- [23] ABAQUS 6.12 Analysis User Manual. Internet Manual. Dassault Systèmes Simulia Corp., Providence, RI, 2012.
- [24] Cole RH. *Underwater Explosions*. Princeton: Princeton Univ., 1948.
- [25] Arons A, Yennie D. Energy Partition in Underwater Explosion Phenomena. *Rev of Mode Phys* 1948; 20(3): 519-36.
- [26] Brennen CE. *Cavitation and Bubble Dynamics*. New York, NY: Oxford UP, 1995.
- [27] Harte AM, Fleck NA. On the Mechanics of Braided Composites in Tension. *Eur J of Mech - A/Solids* 2000; 19(2): 259-75.
- [28] Turner SE (2004) Small-scale implosion testing of glass and aluminum cylinders. NUWC-NPT technical memorandum 04-061, Naval Undersea Warfare Center Division, Newport, RI
- [29] Rayleigh L. On the pressure developed in a liquid during the collapse of a spherical cavity. *Philos Mag Ser* 1917; 6(34):94–98.

Chapter 2 : Hydrostatic Implosion of GFRP Composite Tubes Studied by Digital Image Correlation

by

Michael Pinto, Sachin Gupta, and Arun Shukla

has been published in the Journal of Pressure Vessel Technology

Corresponding Author: Arun Shukla

Dynamic Photo Mechanics Laboratory

Department of Mechanical, Industrial and Systems Engineering

University of Rhode Island

206 Wales Hall, 92 Upper College Rd Kingston, RI, 02881,

USA Phone: +1-401-874-2283

Email Address: shuklaa@uri.edu

ABSTRACT

The mechanisms and pressure fields associated with the hydrostatic implosion of glass-fiber reinforced polymer (GFRP) tubes with varying reinforcement are investigated using high-speed photography. Experiments are conducted in a large pressure vessel, designed to provide constant hydrostatic pressure throughout collapse. 3-D Digital Image Correlation (DIC) is used to capture full-field displacements, and dynamic pressure transducers measure the pressure pulse generated by the collapse. Results show that braided GFRP tubes release pressure waves with significantly greater impulse upon collapse as compared to filament-wound tubes, increasing their damage potential.

Introduction

Composite materials have gained significant relevance in naval and marine applications due to their many advantages over traditional metals. Composites offer alternatives that are lighter, have improved corrosion resistance, and for submerged structures, boast greater operating depths. Composites have also found unique application in the repair of existing marine structures, particularly due to their excellent resilience against the aggressive sea environment [1]. For these reasons, the presence of composite materials in marine industries is increasing, indicated by their current use in several naval applications, such as sonar domes, masts, and hull sheathings[2]. One of the biggest obstacles to widespread adaptation of composite materials is a lack of complete understanding and simple design rules for these materials, especially under extreme loading conditions[2]. For this reason, the present work looks to expand the current knowledge of composite behavior by examining the problem of implosion of glass fiber reinforced composite tubes.

The implosion of an enclosed submerged structure occurs when external pressure reaches a critical value, causing an instability in the structure and resulting in a rapid and often catastrophic collapse. During this collapse, the boundaries of the structure and surrounding fluid are accelerated to high velocities and stop suddenly once the collapse is completed. This abrupt change in momentum releases a pressure wave into the surrounding fluid, which can have the potential to damage nearby structures[3-5]. For this reason, the implosion problem has gained much attention in recent decades. The implosion of glass spheres has been studied by several authors who characterized the pressure pulse emitted during collapse as well as its damage potential to nearby structures[3-7]. The implosion of aluminum tubes has also been studied in recent work[8-10]. Turner and Ambrico identified key stages of the implosion event in relation

to the local pressure about the collapsing structure [9]. In this work, the implosion of aluminum tubes resulted in (i) an initial period of underpressure as the implodable volume is reduced, (ii) a small, sharp peak corresponding to the wall-to-wall contact at the completion of collapse, (iii) a larger positive pressure peak resulting from the change in momentum of surrounding fluid, and (iv) a broad overpressure period as the collapse propagates through the length of the tube. Most recently, Ikeda et. al studied the free-field implosion of aluminum and brass tubes with varying geometries [10]. This work examined the effect of different modes of collapse on the emitted pressure pulse, and used bubble dynamic scaling laws to compare these changes.

Few experimental studies on the implosion of composite structures have been reported in recent works. Moon et al. examined implosion of filament-wound carbon/epoxy composite tubes with different winding angles both experimentally and computationally to determine collapse pressures and modes[11]. Both Ross and Smith performed experiments on carbon/E-glass tubes to determine critical buckling pressure, buckling modes, and create design tables[12,13]. Hernandez-Moreno et al. studied filament-wound glass/epoxy composite tubes with a winding angle of 55° to examine effects of winding pattern on the collapse pressure[14]. Olivas et al. experimentally evaluated the buckling of glass/vinylester tubes under external pressure to test predictions and design criteria related to the collapse [15]. Hur et al. examined the buckling modes, loads, and play failure of carbon/epoxy tape layup tubes both experimentally and computationally[16]. Yang et al. developed an analytic model for critical buckling pressure based on anisotropic laminate theory and performed experiments on E-glass/epoxy tubes to test predictions[17]. Ramirez and Englehardt experimentally characterized the effect of delaminations on the buckling of large carbon fiber cylindrical risers subjected to external pressure [18]. However, in none of these studies is the pressure pulse from the collapse

measured, nor are high speed images of the collapse event captured. Furthermore, their implosion experiments were not conducted in a large enough vessel to maintain hydrostatic pressure constant through collapse, thereby changing the conditions seen in open ocean.

Following a previous study on the implosion of carbon/epoxy tube[19], The current study seeks to add to the current understanding of composite materials by investigating the implosion of glass-fiber reinforced polymer (GFRP) tubes. Among different composite systems, GFRPs are of particular interest to the naval industry due to their low cost and excellent resistance to both corrosion and water absorption. Specimens of varying geometry and reinforcement architecture are studied to examine the effects of these parameters on the damage and failure progression of the structure as well as the emitted pressure pulse. High-speed photography coupled with 3-D digital image correlation is used to capture real-time deformation throughout the implosion event, while dynamic pressure transducers are employed to characterize the effect of collapse on local pressure fields. It is shown that the implosion of GFRP tubes results in the release of a potentially hazardous pressure pulse to the environment, and the nature of that pulse will be dictated by the damage and failure mechanisms dominating the collapse event. Filament-wound tubes are shown to release a significantly less damaging shockwave than similar braided tubes, as more energy intensive damage mechanisms dominate the failure process.

Experimental Details

A specially designed 2.1m diameter spherical pressure vessel is used to conduct all implosion experiments (see Fig. 1). The vessel has a maximum pressure rating of 6.89MPa and provides a constant hydrostatic pressure throughout the collapse event. Several acrylic windows mounted about the midspan of the pressure vessel allow the specimens to be viewed by cameras and adequately lit by two high intensity light sources.

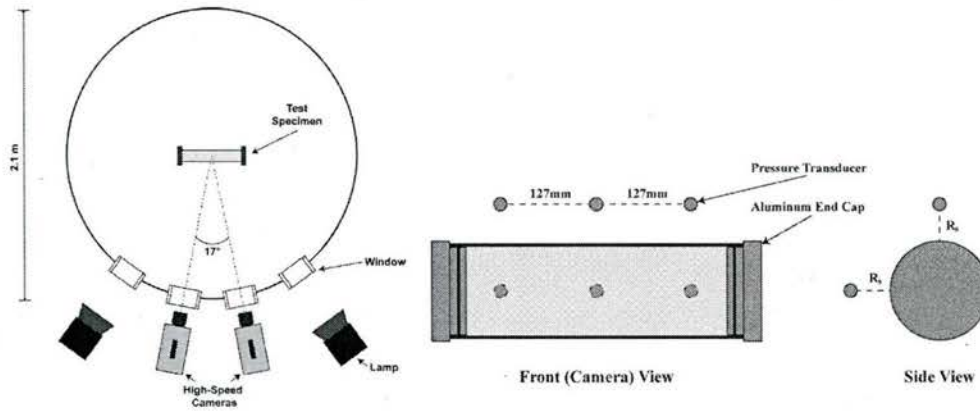


Fig. 1: Experimental apparatus (left) and specimen configuration (right)

Two different material systems are studied, filament-wound glass fiber/polyester(PE) and braided glass fiber/epoxy. Filament-wound glass/PE tubes consist of three unidirectional glass fiber reinforcement plies arranged in a $[\pm 55/90]$ orientation. These tubes are manufactured by Nor'Easter Yachts Inc. (Milford,CT) with a nominal wall thickness of 2.08mm and inner diameter of 57.2mm for the smaller tubes referred to as RT, and 101.8mm for larger tubes referred to as GT. Braided glass/epoxy tubes (referred to as BG) are manufactured with a $[\pm 55]_3$ layup by Polygon Composites (Walkerton, IN) with a nominal wall thickness of 2.03mm and inner diameter of 60.1mm. All specimens have an unsupported length of 381mm. The dimensions are selected as to provide specimens with a low expected collapse pressure, and a high radius-to-thickness ratio (>14) so that thin-wall assumptions may be utilized. At least three experiments were performed for each case to ensure repeatability of results. The material properties of the specimens studied are listed in Table 1.

Specimen	Reinforce- ment	Inner Diameter	Wall Thickness	L/D	Effective Modulus	P_{cr} (MPa)

		(mm)	(mm)		$\left[\sqrt{E_{11}^2 + E_{22}^2} \right]$ (GPa)	
RT	Filament-Wound	57.2	2.08	6.4	35.4	2.05[±0.01]
GT	Filament-Wound	101.8	1.91	3.7	20.2	0.68[±0.03]
BG	Braided	60.1	2.03	6.3	14.7	1.94[±0.08]

Table 1: Geometric and material properties of studied specimens

Prior to set-up, all composite tube specimens were sealed using two aluminum end caps fitted with rubber O-rings, and quick setting epoxy is applied to the seam between the end cap and the tube. The specimen is then suspended horizontally in the center of the pressure vessel using several steel cables attached to the inner walls of the vessel. The tubes are secured in such a way that they cannot move or float during the filling process and the painted surface is faced toward the viewing windows. To measure the changes in local pressure during the collapse event, several tourmaline dynamic pressure sensors (PCB 138A05, PCB Piezotronics, Inc., Depew, NY) are mounted at different locations about the midspan. All sensors are mounted such that the standoff distance between the sensing element and the outer surface of the specimen is nominally equal to the radius of the specimen. The amplified outputs of these sensor are captured by an

Astro-med Dash® 8HF-HS portable data recorder (Astro-Med Inc., West Warwick, RI) at a sampling rate of 2 MHz.

The pressure vessel is then flooded with water that is first filtered for maximum optical clarity, leaving a small air pocket at the top. Later, nitrogen gas is introduced into the air pocket to pressurize the enclosed water. The pressure inside the vessel is increased at a gradual rate (0.083 MPa/min) until the specimen collapsed. At this point, the cameras and pressure sensors are end triggered to record the data occurring 1 second prior to triggering, effectively capturing data over the entire collapse event.

DIC Technique

3-D Digital image correlation (DIC) is a well known experimental tool used to determine real-time, full-field displacements across the viewable surface of a specimen during static as well as dynamic events[20]. This technique is very simple to implement in typical laboratory environments where the only viewing medium between the subject and the camera lens is air, however, when multiple media are present in the viewing path, the application of this optical method becomes difficult. In the experiments discussed in this study, between the camera lens and the specimen is air, a thick acrylic window, and a large quantity of water. Due to the difference in refractive index between these media, the image viewed by the camera will experience magnification and refraction, introducing significant error to image measurements. To overcome these problems, the 3-D DIC method is calibrated for underwater experiments based on previous work [21] for good confidence in the accuracy of measured displacements and velocities. Here the basic methodology and results of that work are summarized.

Calibration experiments are conducted by imaging a submerged calibration specimen within a small tank, designed in a way to replicate the optical effects of submersion using a more accessible smaller tank. A schematic of the setup is shown in Fig. 2. The setup is approximately 600 mm long and 200 mm wide with height of 150 mm. Two acrylic windows, of same thickness to those used in the pressure chamber are installed with a stereo angle of $\sim 20^\circ$ for viewing purpose. A 76 mm x 51 mm (3 in x 2 in) speckled flat aluminum specimen is mounted inside the tank on a precision translation stage, which can provide both in-plane and out-of-plane translation with 0.01 mm accuracy.

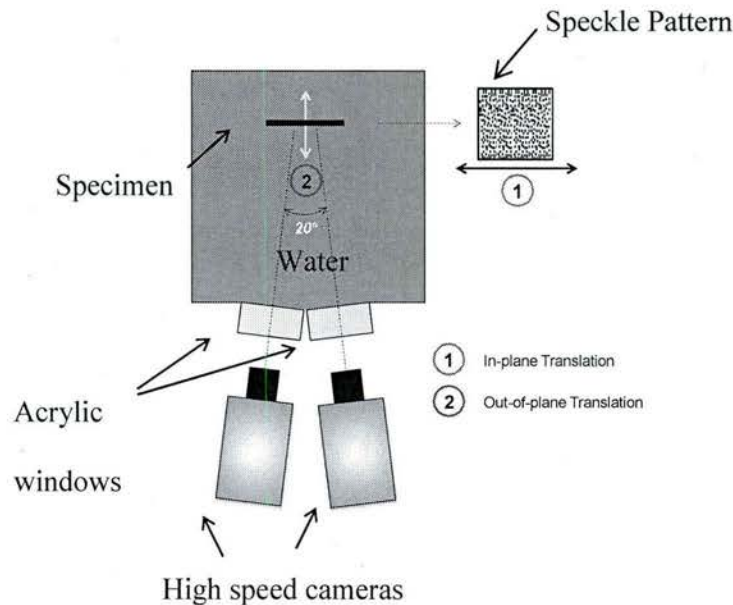


Fig. 2: Calibration experiment for 3D DIC of submerged structures

High-speed cameras are placed outside the tank such that the surface normal of each window is aligned with the optical axis of the respective camera. The specimen is placed at approximate the intersection point of the two camera axes inside the tank (450 mm deep in water), a location that is consistent with implosion experiments. Using the translation stage, the specimen is translated

in 1 mm increments in both in-plane and out-of-plane direction and the corresponding images are captured. Displacement at each translation increment is estimated with Vic-3D software.

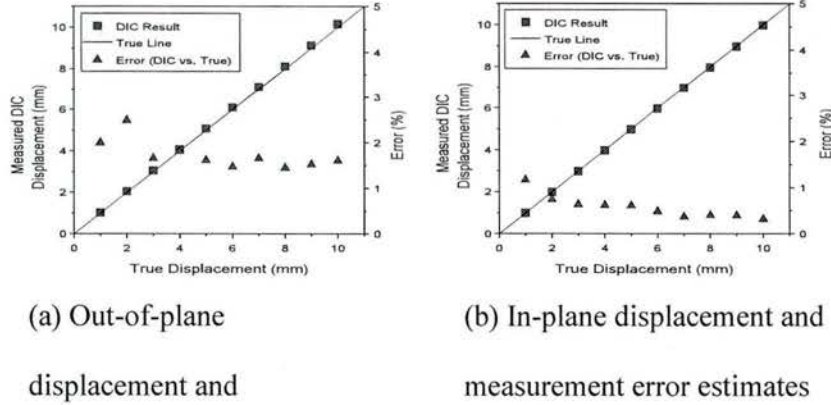


Fig. 3: Calibration results for out-of-plane and in-plane translation

A plot of the actual out-of-plane displacement and the measured average displacement of the specimen is shown in Fig. 3(a). The measured average surface displacements are in good agreement with the true displacements and the percentage error between true and measured out-of-plane displacement is $\sim 1.5\%$ to 2.5% , showing that the out-of-plane displacements can be accurately captured ($< 3\%$ error).

A comparison of given in-plane displacement and measured average DIC displacement as shown in Fig. 3(b) indicates that the two are in very good agreement. The absolute magnitude of error is nearly constant ~ 0.02 to 0.03 mm for the range of given displacement and therefore the percentage error shown in Fig. 3(b) decreases (from 1.2% to 0.5%) with increase in displacement. Therefore, when the optical axis of cameras is aligned with the normal of the viewing windows, both in-plane and out-of-plane displacements can be measured with good accuracy for submerged objects by using the camera and stereo parameters obtained using a submerged calibration grid.

A random speckle pattern is applied to a region covering the entire length of the specimen and approximately half of the circumference using flat black paint marker. This region is painted white prior to speckling to enhance the contrast of the pattern. Features of the pattern were made sufficiently large as to occupy at least 3x3 pixels in the recorded images for optimal quality and DIC measurements [20]. In addition, the paint was selected to provide perfect bonding with the material surface through large deformations. Two high-speed cameras (Photron SA1, Photron USA, Inc.), offset by 17° are used to capture stereo images of the patterned region of the specimen at 20,000 frames/s for RT tubes, 50,000 frames/s for BG tubes, and 40,000 frames/s for GT tubes. The stereo images are analyzed using a commercially available image correlation software, VIC3D 2012(Correlated Solutions, Inc., Columbia, SC).

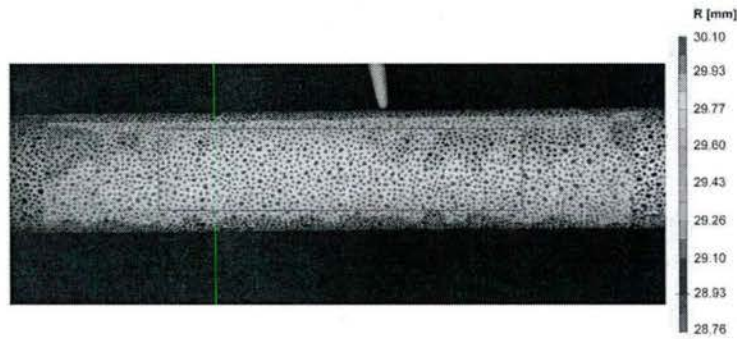


Fig. 4: Example of radius reconstruction of submerged RT composite tube

To further validate the DIC technique for underwater experiments, the outer radii of each specimen is reconstructed using DIC software. In each case, the calculated outer radius is within 5% of the measured value. As an example, an image of a typical RT specimen with reconstructed radius is shown in Fig. 4. In the region indicated by the box, the average calculated radius is 29.42mm with a standard deviation of 0.18mm. This is quite close to the true outer radius of 30.66mm and gives confidence in the accuracy of DIC in this application.

Collapse Pressure Predictions

To properly design experiments, accurate predictions of the collapse pressure of composite tubes is necessary. In this study, two methods of prediction were used, one empirical based, and one numerical. Koudela and Strait [22] developed a procedure to create design formulae for laminated and sandwich composite tubes under hydrostatic pressure. These authors started with the von Mises solution[23] for isotropic tubes and made several empirical modifications to the above formula to account for the anisotropy of the laminates and the non-uniform distribution of stress through the thickness of the laminate, resulting in the following modified design equation:

$$P_{critical,ani} = \frac{0.85\sqrt{E_1 E_2} t^{2.5}}{(1-\nu_{12}\nu_{21})^{0.75} L R_c^{0.5} R_o} * \frac{1}{1 + \frac{\sqrt{E_1 E_2} t^2}{12 R_c R_o G}} \quad (1)$$

Here, E_1 and E_2 are the longitudinal and transverse moduli, respectively, ν_{12} and ν_{21} are Poisson's ratios of the two major axes, R_c and R_o are the mean and outer radii of the laminate, respectively, and G is the shear modulus.

Finally, the expected collapse pressure and shape are also predicted using Finite Element Analysis (FEA) with commercially available ABAQUS software (Dassault Systèmes Americas Corp., Waltham, MA). A linearized buckling analysis [24] is conducted using this software package to obtain the first buckling mode and pressure. Here, an eighth-symmetry model of the tube is created, with the end caps represented by pinned boundary conditions and 4-node shell elements used to define the material. This analysis is performed to increase confidence in the validity and repeatability of experimental observations.

For the tubes in this study, the analytic and empirical predictions of buckling pressure described above provided a useful means of estimating the magnitude of the collapse pressure and provided

an upper bound for that parameter. The predictions obtained from FE linearized buckling analyses are much more accurate, predicting the collapse typically within 10% of the observed value.

Specific and Total Impulse

Another parameter important to the analysis of pressure pulses from various sources is the impulse of the wave. The impulse delivered by the pulse is often just as if not more indicative of damage potential than the peak pressure at which it is delivered [25]. This is because the impulse combines the effect of both pressure magnitude and the duration of that pulse, which heavily influences the response of a structure. For this reason, the specific impulse of the local pressure history is calculated for each specimen type. The specific impulse delivered up to an arbitrary time, t , is defined simply as [25]:

$$I = \int_0^t \Delta p dt \quad (2)$$

where Δp is the dynamic pressure at time t . To form a better means of comparing impulses between specimens with different collapse pressures, a normalized impulse is defined as follows:

$$\bar{I} = \frac{\int_0^t \Delta p dt}{\int_0^t P_0 dt} \quad (3)$$

Where P_0 is the hydrostatic pressure during the collapse event.

Time-Frequency Analysis

Frequency analysis is often useful in classifying and comparing acoustic signals such as those generated in the implosion event. However, typical frequency analysis tools such as Fast Fourier Transform (FFT) have the disadvantage of lacking temporal data, and thus are best suited to long

duration, stationary signals. The signals measured in this study are highly transient by nature, and have a very short duration, making FFT less appropriate. As an alternative, time-frequency analysis is explored by using continuous wavelet transform (CWT).

Wavelet transform is performed by fitting a series of wavelets to a signal rather than a series sine or cosine waveforms as in the case of FFT. Wavelets are waveforms with a finite duration, zero mean, and a small range of frequencies over their length [26]. This allows the retention of time data, allowing the visualization of the frequency content of various events in the time history, and making this method better suited to the present study. The CWT method seeks to find an array of "scales" as a function of time which relate to the frequency content of the signal at that time. This is accomplished using the following algorithm:

$$C(a, b, f(t), \Psi(t)) = \int_{-\infty}^{\infty} f(t) \frac{1}{\sqrt{a}} \Psi^* \left(\frac{t-b}{a} \right) dt \quad (4)$$

Where $f(t)$ represents the signal in question, $\Psi(t)$ is the function definition of the specific wavelet family used and $\Psi^*(t)$ is its complex conjugate, a is a scaling parameter, and b is a temporal shifting parameter. This shows that in this type of transform, the finite wavelets are scaled in magnitude and shifted in time to fit the input signal, which is how both time and frequency data are simultaneously obtained.

For the analysis in this study, the time series are first denoised using a discrete wavelet transform with Daubechies wavelets (db4), and the denoised signal is processed through a CWT using the Morlet wavelet family.

Results and Discussion

57.2mm Filament-Wound Tube (RT)

The smaller diameter filament-wound specimens fail at 2.05 MPa in a mode 2 buckling shape, forming two lobes. The tubes flattened completely during the dynamic failure event, but were seen to rebound to a nearly cylindrical shape following the release of pressure. The local pressure history measured about the midspan of these specimens is seen in Fig. 5. In this study, dynamic pressure is defined as the gage pressure minus the hydrostatic pressure in the tank at the time of collapse. High-speed photographs as well as DIC generated displacement and velocity contours corresponding to marked events on that trace are included in Fig. 6 and 7, respectively.

Qualitatively, this pressure trace at first appears very much like those measured for aluminum tubes by previous researchers [8-10], with a gradual decay in pressure followed by a pressure spike and a broad overpressure region.

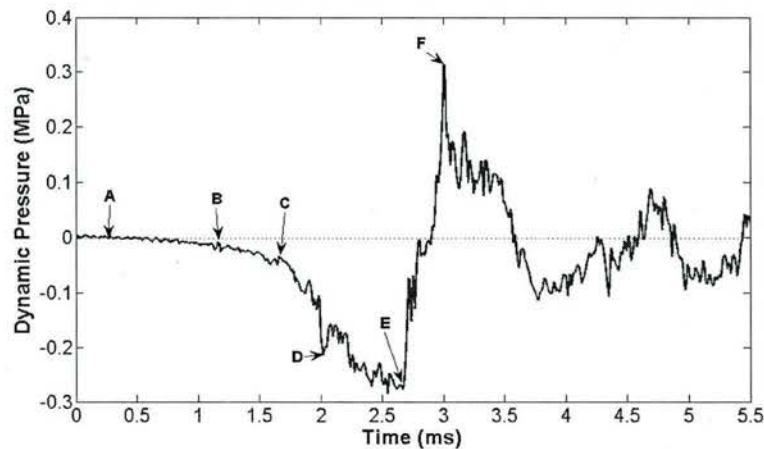


Fig. 5: Average dynamic pressure measure about the midspan of RT specimens

Prior to the dynamic collapse event, these specimens begin to oval significantly in a quasi-static manner. The DIC displacement contour shows a maximum radial deflection of -3.9mm (13.6%

of specimen radius) at time A, indicating that this initial slow ovaling is quite significant for these tubes. From time A to B, DIC contours reflect the observed smooth deformation with relatively low radial displacement and velocity at time B. The unstable collapse appears to initiate at this time, where a steady drop in pressure is seen marking the beginning of the underpressure region of the pressure history. Examining the corresponding high-speed photograph, it is observed that damage also initiates at this time as indicated by the white arrow. This damage comes in the form of interfibrillar cracking/debonding, which will come to dominate the damage behavior of these materials. Pressure decays steadily until time C where the rate of decay increases suggesting an intensification of the collapse. The matched image in Fig. 6 shows the appearance of a dimple near the initiation of collapse, characteristic of the mode 2 buckling shape. The contours at time C also clearly show the dimple developed in the midspan of the specimen at that time. This region shows highly localized displacement of -12mm and much higher velocity of 18m/s, while the area outside of the dimple is largely unchanged from the previous key point. This shows that in the initial stages, this instability is a highly localized phenomenon.

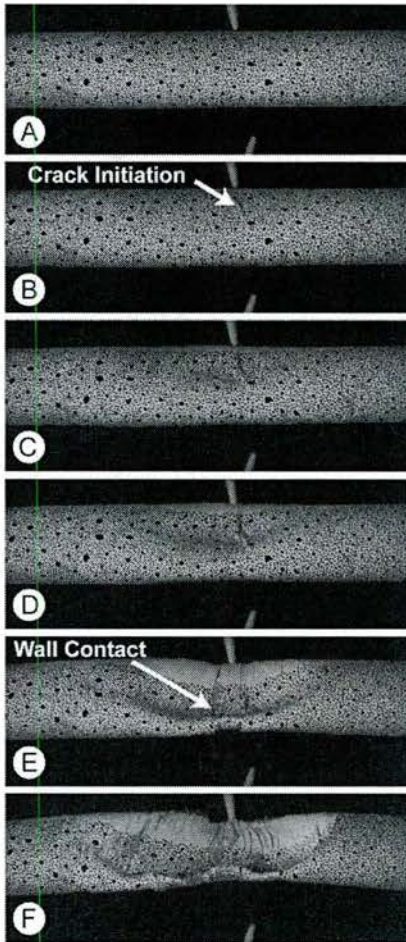


Fig. 6: High-speed photographs of key events for RT specimens

This new rate of pressure decay is maintained fairly constant until time D where the pressure is seen to drop quite suddenly. The photograph at this time shows that the dimple formed previously has grown significantly, and that additional fiber/matrix debonding is apparent on the specimen surface. This accumulated damage effectively reduces the stiffness and structural integrity of the tube, allowing for more rapid deformation and as a result steeper pressure drops. DIC contours show an intensification of both radial displacement and collapse velocity in the region of the observed dimple. The displacement and velocity are quite high at this time, 18mm

and 20m/s respectively, however they are still localized to the small region of the dimple, while the rest of the structure maintains a near zero velocity. This rapid increase in displacement and velocity explains the further change in slope of the pressure decay as the collapse further hastens. After this time, image correlation is lost completely due to the destruction of the speckle pattern on the surface of the specimen. The beginning of this destruction can be seen in the contours at times C and D as increasingly large regions are devoid of data. It should be noted that due to this loss in DIC data, the maximum velocity prior to wall contact is not captured.

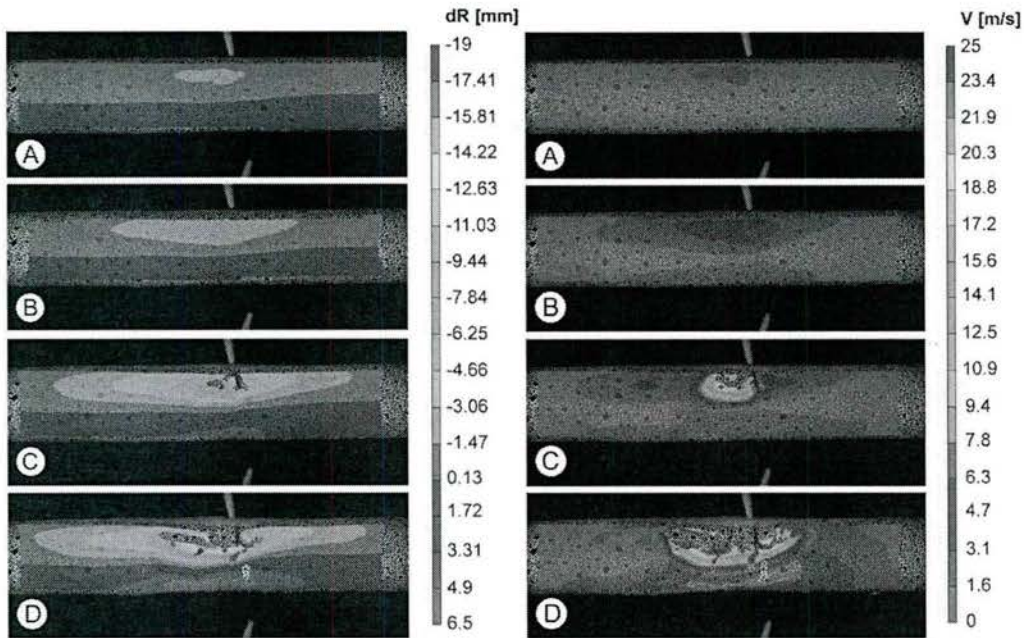


Fig. 7: DIC contours of radial displacement (left) and velocity (right) for RT specimens

After this time, pressure continues to decay until a minimum value is reached. Shortly thereafter, a distinct, fairly small peak is observed at time E as pressure steeply rises. This peak is consistent with observations on the implosion of aluminum tubes [8-10] and represents initial contact of the walls of the structure. This is confirmed using high-speed photography, as the tube is seen to

make wall contact at that time in the location indicated by the white arrow. Pressure continues to rise until a maximum is reached at time F. The image at this time shows the propagation of the wall contact both circumferentially as well as axially. This peak is followed by a broad overpressure region as the collapse continues to propagate through the length of the specimen, after which the pressure returns to oscillate about the hydrostatic value.

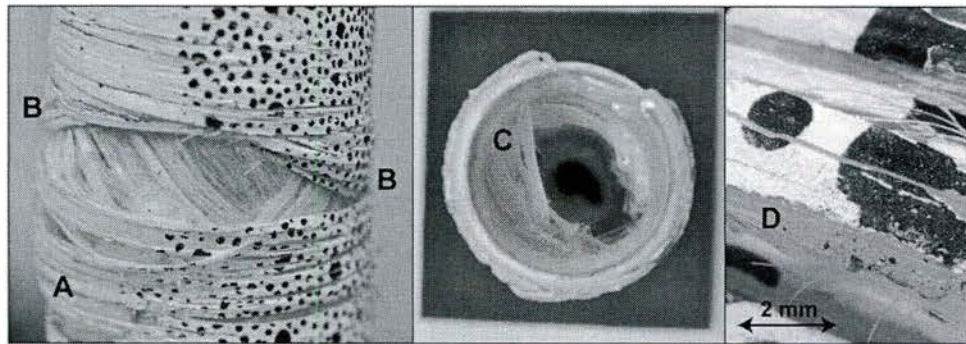


Fig. 8: Post-mortem images for glass/PE specimens, showing (A) matrix cracking, (B) delamination of outer hoop ply, (C) delamination of inner helical ply, and (D) long pulled-out glass fibers

Post-mortem images of RT specimens, shown in Fig. 8, give a clearer view of the types and scales of damage incurred on the structure. In these images, the damage present is seen to be overwhelmingly delamination, matrix cracking, marked as "A", and fiber pull-out. Delamination of the outer ply, marked as "B" exposes the helical plies beneath, and much of the inner-most ply has also delaminated and is seen pushed in on the interior of the tube, marked as "C".

Composites with unidirectional reinforcement are typically quite weak in terms of delamination as compared to other reinforcement types, as the reinforcing plies simply lay upon one another with little interply interaction [27]. For this reason, when the tubes experience large deformations during collapse, delamination initiates in the early stages of the event and continues to dominate

through collapse. Optical micrographic investigation of the fracture surface also shows very long intact glass fibers protruding from fracture surfaces, indicated by "D". This shows that fiber pull-out does indeed play a very significant role in the failure of these tubes. These major modes of damage explains the many jumps and changes in slope in the underpressure region. The nature of the underpressure region can be compared with the physical "stick-slip" phenomenon seen in the delamination of composite materials as well as in fiber pull-out [27].

101.8mm Filament-Wound Tube (GT)

The larger diameter filament-wound specimens fail at 0.68 MPa in a mode 2 buckling shape. As with the smaller specimens, these tubes regain much of their initial circularity following the collapse, and also recover significant structural stability. The local pressure history measured about the midspan of these specimens is seen in Fig. 9 and high-speed photographs as well as DIC generated displacement and velocity contours corresponding to marked events on that trace are included in Figs 10 and 11, respectively.

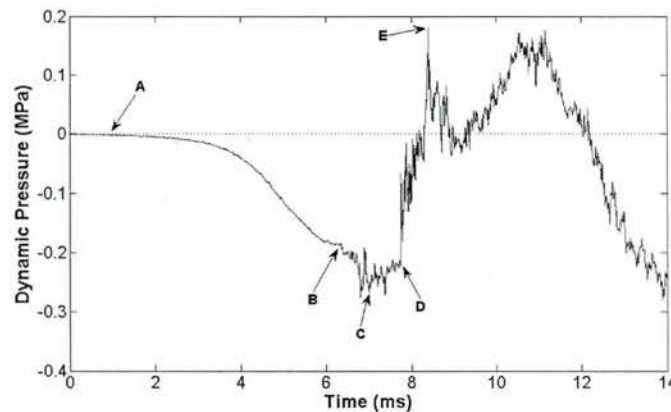


Fig. 9: Average dynamic pressure measure about the midspan of GT specimens

As is the case with the smaller RT tubes, the larger diameter GT specimens experience a significant amount of gradual ovaling prior to dynamic collapse. The DIC displacement contour shows a maximum radial deflection of -4.1mm (8.1% of specimen radius) at time A, similar in magnitude to that seen in the smaller specimens. After the dynamic collapse initiates, a rather smooth and gradual decay in pressure is observed between times A and B as the structure deforms in on itself without noticeable damage on the surface. DIC contours at time B indicate that over the course of this smooth deformation, large displacements of up to 36mm are achieved and the structure accelerates to a velocity of approximately 17m/s.

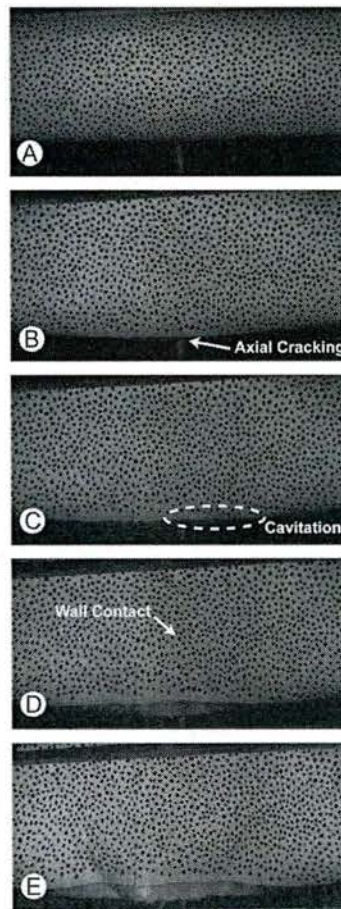


Fig. 10: High-speed photographs of key events for GT specimens

After time B, a more abrupt drop in pressure is observed. This is a result of longitudinal cracks that form along the apexes of the buckle lobes, causing a more abrupt increase in velocity and drop in pressure in the vicinity of the cracks due to a loss of structural integrity. At time C, the pressure at the surface of the structure drops low enough to initiate cavitation bubbles (see high speed image in Fig. 10), which grow to a critical size and then collapse on themselves. It is well known that the collapse of cavitation bubbles against a surface results in the release of very peaky pressure waves [28], and the superposition of these waves with the underpressure region results in their observed "peaky" period between times B and D. At time D, a very sharp spike is seen in the local pressure trace and wall-to-wall contact is observed in the region indicated by the arrow in the matched high-speed photograph. Wall contact is confirmed by examining the DIC velocity contour at this time which shows a small region of zero velocity at the center of the midspan. This point contact results in the release of the acoustic pressure spike recorded at time D. Additionally, the displacement contour at that time shows a maximum radial displacement of -49.4mm, which is quite close to the inner radius of the structure of 50.8mm. The maximum structural velocity prior to wall contact is measured by DIC as 18 m/s.

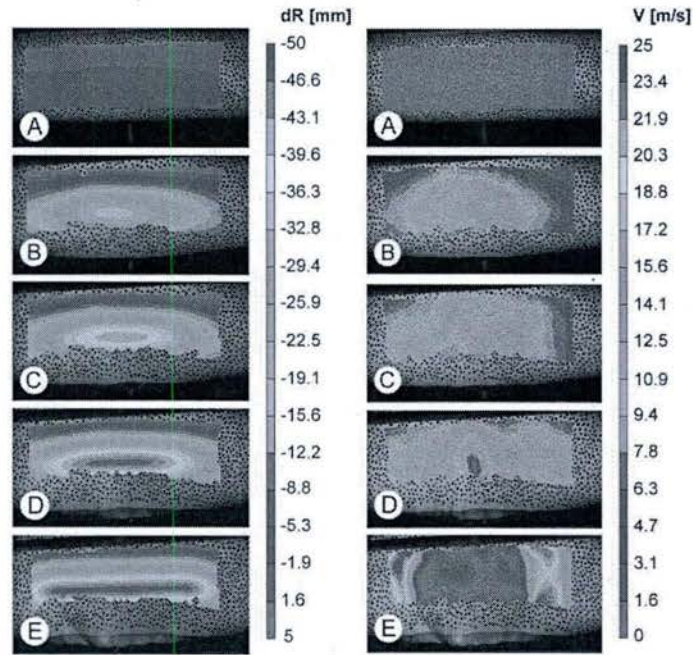


Fig. 11: DIC contours of radial displacement (left) and velocity (right) for GT specimens

Following wall contact, pressure rises rapidly to a maximum at time E as a result of the sudden momentum change imparted to surrounding fluid. DIC displacement and velocity contours show that the midspan of the specimen has flattened completely, and this buckle begins to propagate axially. This is evidenced by the expanded area of zero velocity combined with the greater region of near 50mm radial displacement. An interesting observation at this time is the development of a "buckle front", or a region of high velocity ($\sim 25\text{m/s}$) immediately ahead of the collapsed, zero velocity zone. This corroborates with previous buckling experiments performed on long pipes which showed the propagation velocity of the buckle is significantly greater than the initial radial collapse velocity attained in the formation of the buckle [29]. After time E, the buckle shape continues to propagate through the length of the structure and pressure measurements are dominated by reflections from the tank boundaries.

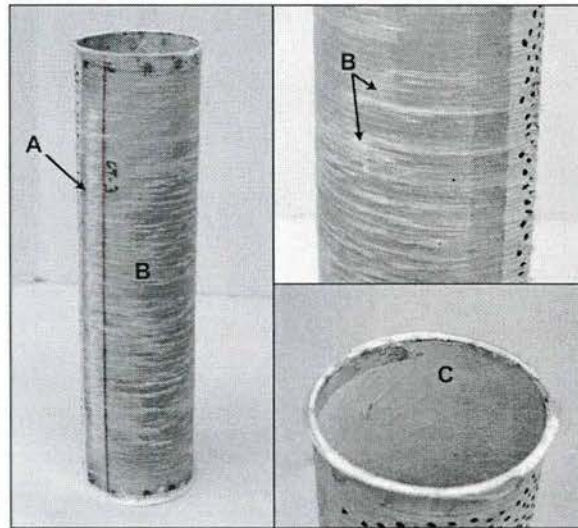


Fig. 12: Post-mortem images of GT specimens, showing (A) longitudinal cracking, (B) internal delamination, and (C) matrix cracking in the innermost ply

Post-mortem images of GT tubes, included in Fig. 12, show the dominating damage and failure mechanisms present in these materials. In these tubes, damage is largely confined to two longitudinal cracks corresponding to the two buckling lobes, marked as "A", and large areas of whitening implying internal delamination, indicated by "B". An amount of interfibrillar matrix cracking is evident in the internal ply of these tube, marked as "C", though it is fairly minor in comparison. Overall, the extent of damage in these specimens is remarkably less than for the smaller diameter RT specimens of the same make. This is due to the larger size of the GT specimens, coupled with a much lower collapse pressure. Therefore, the potential hydrostatic energy at collapse may be dissipated in the deformation of the structure without resulting in catastrophic damage.

Braided Tube (BG)

Braided glass specimens fail at 1.94 MPa in a mode 2 buckling shape, flattening to a similar degree as aluminum specimens [8-10]. Like other specimens, circularity and structural integrity is regained following the release of pressure though to an even larger degree. The average local pressure history measured about the midspan of a typical specimen is seen in Fig. 13 and high-speed photographs as well as DIC generated displacement and velocity contours corresponding to marked events on that trace are included in Figs 14 and 15, respectively. The pressure trace for these specimens appears quite different from filament-wound glass/PE tubes discussed previously. Because dimensions and collapse pressures are very similar, this can be attributed to the change in reinforcement architecture.

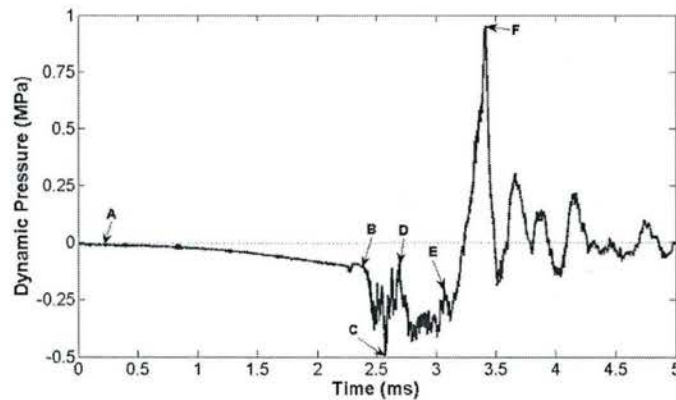


Fig. 13: Average dynamic pressure measure about the midspan of BG specimens

An amount of initial ovaling did occur in these specimens, although it is considerably less than either filament-wound specimen. The DIC displacement contour records a maximum deflection of -1.3mm (4.3% of specimen radius) prior to the implosion event. The dynamic collapse begins with a relatively slow decay in pressure from time A to time B, lasting ~2.25ms. This is much longer than the initial gradual decay seen in RT tubes, which lasted ~1ms before intensifying. At

time B, a slight recovery in pressure is seen followed by a very sharp drop to a minimum at time C. This is accompanied by the initiation of longitudinal cracking at the location indicated in the matched image. This suggests a very sudden loss in structural stability occurs at time B, resulting in the rapid acceleration of the structure and, consequently, an equally rapid drop in pressure. The velocity contour at this time displays a highly localized region of high velocity (11 m/s) appearing in the vicinity of that crack, confirming this hypothesis. The underpressure region continues until time E where a distinct peak is observed followed by a rapid increase in pressure, indicating wall contact. This is confirmed by examining the corresponding high speed image in which contact is observed in the marked region.

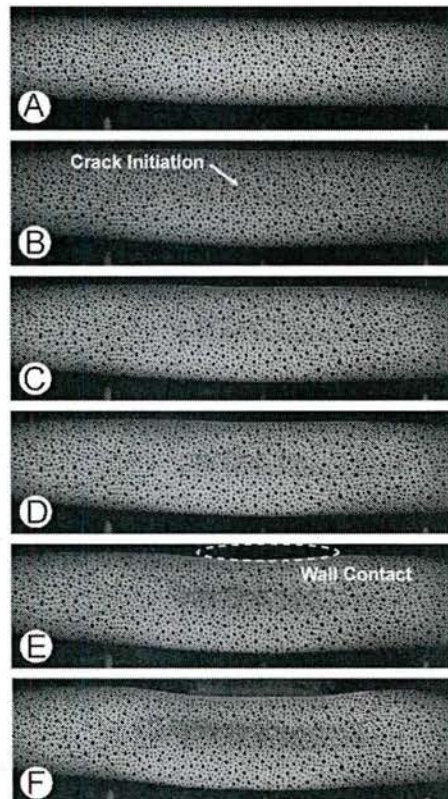


Fig. 14: High-speed photographs of key events for BG specimens

DIC contours at this time show the velocity at the nadir of the buckle valley suddenly drops and higher velocity regions are seen to either side of this point. This further reinforces the previous observation of wall contact at this time as deformation will halt wherever contact is made. However, due to the orientation of the buckle shape along with some loss of correlation from damage, the actual zero velocity region as well as the maximum collapse velocity are not captured. The high velocity regions to either side of the arrested area indicate the beginning of axial propagation of the buckle shape. After wall contact is made the high magnitude pressure pulse typical of the implosion arrives at time F. DIC contours show that axial propagation continues through time F where high velocity regions progress further away from the initial contact point and the area of near-zero velocity expands. After time F, extensive damage caused complete loss of useful data capture as the speckle pattern is critically obscured. It is interesting to note that as the buckle propagates axially, the magnitude of the high velocity regions appear to increase, reaching a maximum of 23 m/s before total loss of correlation. This is consistent with observations made on the buckling of the larger diameter GT specimens discussed previously.

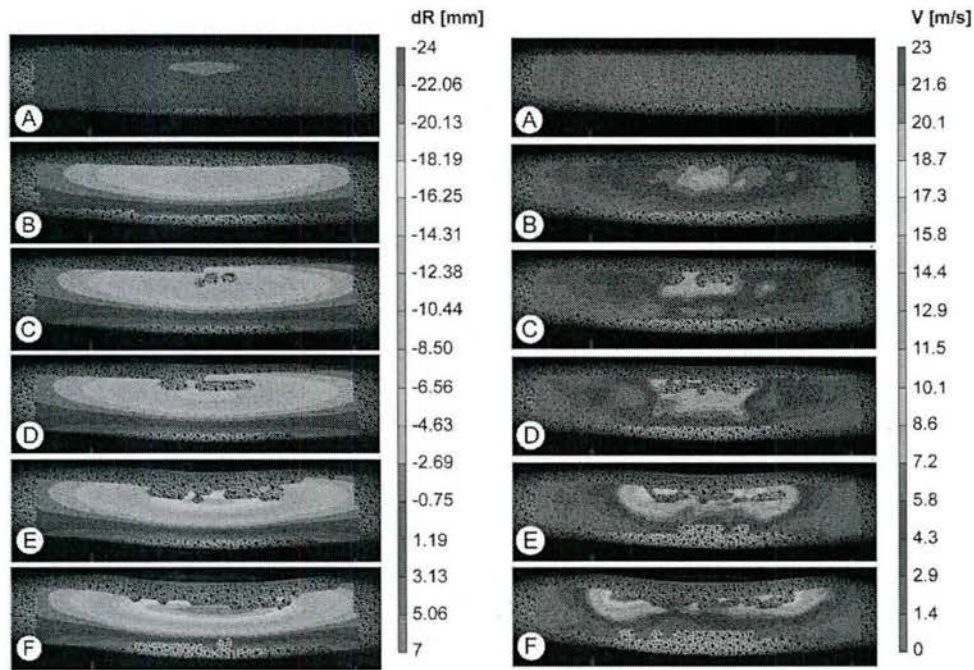


Fig. 15: DIC contours of radial displacement (left) and velocity (right) for BG specimens

Post-mortem images of BG tubes are included in Fig. 16, and show stark contrast compared to filament-wound specimens of similar geometry. First, although during collapse they flattened completely, these tubes are seen to regain nearly all of their original shape after the event.

Additionally, the only damage evident on the surface of the specimen are two cracks in the outer- and inner-most plies, spaced approximately 180° circumferentially. These cracks are marked in Fig. 16 with "A". The longitudinal cracks correspond to the two lobes of the buckle shape, and are formed in the regions of high tensile stress in these lobes. There are also large areas of "whitening" apparent on the non-painted surface of the specimen in the vicinity of the cracks marked as "B". This indicates delamination between some of the internal plies in that region. Though delamination is present, it does not exist on nearly the same scale as for filament-wound tubes, and this is a direct result of the reinforcing architecture. It is well known that composites

with woven fabric reinforcements show much greater resistance to delamination than those with unidirectional reinforcement [27]. This allows delaminations to be arrested through the interaction of adjacent plies in the thickness direction, therefore containing this damage mode.

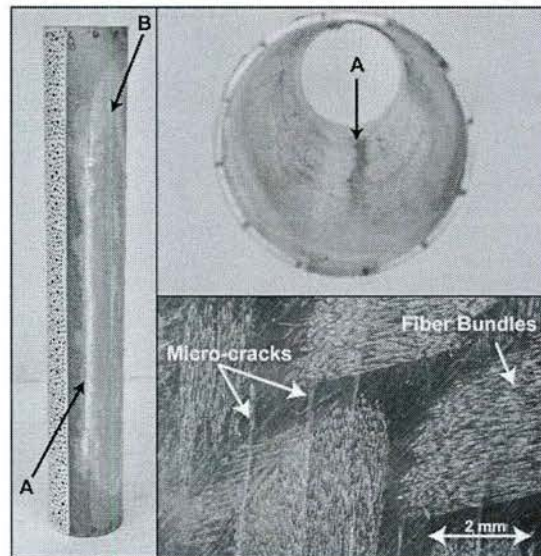


Fig. 16: Post-mortem images of BG specimens, showing (A) longitudinal cracking, and (B) internal delamination

Optical microscopy shows the presence of very many microcracks near the main cracks, each parallel with the nearest fiber bundle. It is clear that these cracks initiated in either the resin-rich regions between the fibers or in the fiber/matrix interface itself, however each crack is relatively short, signaling that they were arrested prior to unstable propagation. This arresting of the microcracks is also a characteristic of woven reinforcement of the braided preform. These cracks initiated in the interfibrillar region are able to propagate easily in the resin-rich regions parallel to fiber bundles, however they soon encounter fibers perpendicular to the direction of propagation. Due to their orientation relative to the propagation direction, these fibers are able to bridge the crack, effectively reducing the stress at the crack tip and arresting the crack. The arresting of

these cracks effectively reduces the extent of damage to the composite structure and is a feature unique to woven architectures.

Pressure Parameters

To evaluate the quantitative effect of reinforcement and geometry on the recorded pressure histories it is useful to compare the extreme values of local pressure attained in each experiment. However, due to the relatively slow nature of the collapse of these tubes, reflections of the initial underpressure wave may in fact reflect back from the walls of the pressure vessel and artificially reduce the magnitude of some parts of the observed overpressure. As a result, the true magnitude of the pressure peak may be somewhat obscured and reduced. Therefore, this discussion will focus solely on the quantities associated with underpressure region itself. For the smaller diameter specimens discussed in this study, the dynamic portion of the underpressure regions are quite short, and so any reflections of the initial, gradual portions of the underpressure would be very small. Because of this, the magnitude of the underpressure region and other parameters associated with this region may be quantified with confidence for these specimens.

Specimen	Minimum Pressure, P_{min} (MPa)	$(P_{min} / P_{cr}) \times 100\%$	Underpressure Duration (ms)	Normalized Negative Impulse, \bar{I}	Potential Hydrostatic Energy (J)
RT	1.72 [± 0.03]	78 [± 2] %	2.653 [± 0.106]	0.0450 [± 0.005]	2011 [± 23]
BG	1.24	76 [± 3]	3.135	0.0703	2096 [± 174]

	[±0.09]	%	[±0.212]	[±0.007]	
--	---------	---	----------	----------	--

Table 2: Summary of experimental results for RT and BG specimens, 95% confidence interval in brackets

However, in the case of the larger diameter GT specimens, there is a region of significantly high magnitude underpressure lasting approximately 4ms, raising the concern of reflections corrupting even latter parts of the underpressure region itself. Therefore, discussions on quantitative aspects of the pressure profiles will be limited to RT and BG specimens, to observe differences caused by reinforcement architecture.

The equivalent minimum pressures at a distance of 0.1m from the center of the tube for all studied specimens are compared in Table 2, normalized by the hydrostatic pressure at collapse. This table shows that for specimens of similar geometry, changing reinforcement from filament wound to braided has little to no effect on either the minimum pressure observed in the near field during the implosion event. For both specimens, a minimum pressure of approximately 77% of the hydrostatic pressure is reached.

To further analyze the effect of reinforcement architecture, the duration of the underpressure region of the pressure histories are compared in Table 2 for tubes of similar geometry. It is observed that the underpressure region for specimens with braided reinforcements lasts, on average, 18% longer than for those with filament-wound reinforcement. This is a result of the two distinct sub-regions of the underpressure for BG tubes, due to the unique deformation characteristics of braided composites. As tensile strain is applied to these structures, the interlaced tows attempt to scissor, restricted by the surrounding matrix material. The restriction

imposed by the matrix causes the tows to lock up, resulting in significant stiffening in the preform [30]. Though the loading of the tube in this case is biaxial compression, as the structure buckles some regions will in fact experience tension, namely outer plies near the apex of buckling lobes and inner plies at the nadir of valleys.

The manifestation of this behavior can be observed in the underpressure region of the braided specimens which appears to exhibit two distinct phases, the first from time A to time B, and the second from time B to time E. The first phase represents deformation prior to damage initiation in the structure. During this stage of the collapse, The interwoven fiber tows are able to scissor, until they lock up resulting in the slight recovery in pressure right at time B. Once the tows lock up, they fail in a brittle manner fairly quickly resulting in the appearance of longitudinal cracks and causing sudden loss of structural stability and rapid pressure drop.

Impulse

The reduction of the overpressure region via reflections of the underpressure wave from the tank boundaries can also lead to the underestimation of the impulse delivered by the overpressure wave. This causes the magnitudes of the impulse of the underpressure and overpressure regions to not be equal, contrary to previous experimental observations [8,9]. This means that the impulse delivered by the overpressure pulse, an important quantity in evaluating damage potential of the wave, may not be accurately measured directly from the pressure history. To overcome this limitation and gain a means to accurately quantify the positive impulse, the fundamental physics involved in this problem are used to show that the negative impulse may be used to indirectly estimate the positive impulse, by showing that at the conclusion of the event, the net impulse must vanish. The details of this derivation may be found in the referenced study [21]. This phenomenon has been observed in several studies on the implosion of glass spheres as

well as the implosion of aluminum tubes [8,9]. Therefore, in the present study the impulse of the underpressure region is calculated, and it is assumed that its magnitude will be equivalent to that of the impulse released in the pressure pulse.

The normalized impulse, as previously defined, delivered in the collapse of each specimen is listed in Table 2. Comparing tubes of similar diameter, it is noted that specimens with braided reinforcement release pressure waves with a 56% greater impulse than those with unidirectional, filament-wound reinforcement. This is a result of the more brittle nature of the failure of braided preforms. As previously discussed, the "locking-up" of braided tows causes significant stiffening in the laminate, and results in a more sudden and brittle failure than in the case of unidirectional wound reinforcements. In fact, the secondary and more rapid region of pressure drop in the underpressure region for these specimens is quite similar to that seen in the implosion of glass tubes [31]. In addition, the damage modes present in RT specimens caused the initial collapse to be very localized to the center of the specimen. DIC generated velocity contours show that throughout the initial stages of the implosion, the deformation of the specimen is characterized by a small region of relatively high velocity, while velocity of the rest of the surface remains near zero. Matrix cracking and delamination in the centralized region caused a severe loss in structural stability, and allowing just the limited area at this location to accelerate. This means that less volume of the surrounding fluid will be accelerated in this case, and consequently, the impulse will be reduced. In addition, RT specimens experienced significantly greater ovaling than BG specimens prior to the dynamic collapse, 13.6% of the original tube radius as compared to 4.3%, respectively. This effectively reduces the distance the walls of RT tubes accelerate prior to contact, and thereby reduces the impulse generated in the surrounding fluid.

Wavelet Analysis

Typical midspan pressures along with the matched scalogram generated using wavelet analysis are plotted for RT and BG specimens in Figs 17(a) and 17(b), respectively.

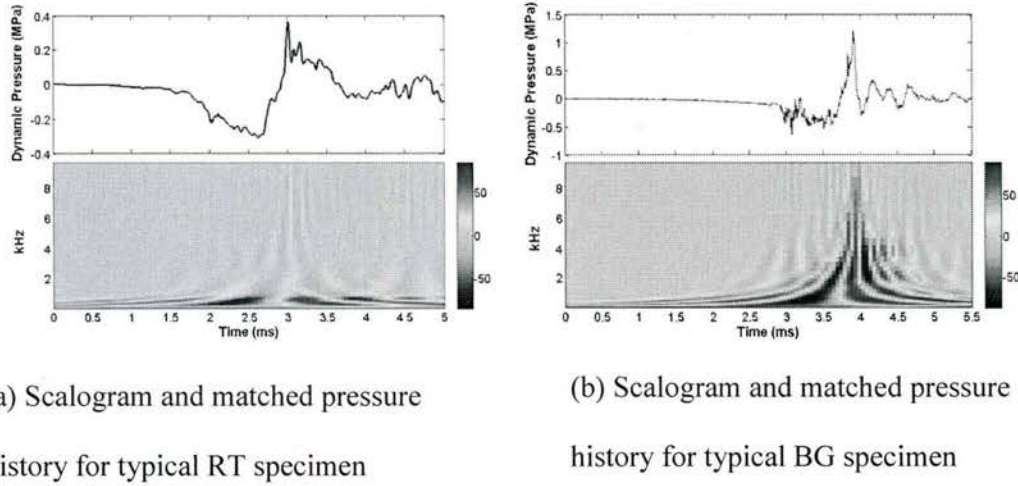


Fig. 17: Wavelet analysis of wound and braided GFRP tubes of similar geometry. Colors represent scaled power levels

In these Figures, the frequency content of the signal is easily correlated to events in the pressure profile, and therefore the frequency content of the high pressure pulse may be identified. The most important difference noted here is that the pulse released by braided specimen has a more broader band of frequency content, up to an in excess of 10 kHz. In contrast, the majority of the energy in the pulse released by filament-wound tubes is confined to the fairly narrow band upper bounded at approximately 1 kHz, with relatively little energy in higher frequencies. This has important implications in the response of structures loaded by this pressure pulse. A pulse with a broadband frequency content will effectively excite a greater range of frequencies in the structure that it is loading. This increases the likelihood of triggering a resonant response, resulting in large deformation and increasing damage potential [32,33]. The reason for this

difference in frequency content is caused by the failure behaviors specific to each reinforcement architecture. Due to the less sudden and more localized initial failure of RT tubes, the initial wall contact spreads more slowly in the circumferential direction as compared to BG tubes which showed a more sudden and less localized collapse. This results in the more gradual transference of momentum change to the surrounding fluid, thereby reducing the high-frequency content in the wave released by the collapse of filament-wound RT specimens. This phenomenon is analogous to differences in frequency content of impact hammer strikes using hammer tips of different degrees of stiffness. Strikes with hammers with softer tips have lessened high-frequency content since the duration of contact is longer than for stiffer tips [33].

Conclusions

The hydrostatic implosion of glass fiber reinforced composite tubes is studied for specimens of varying reinforcement architectures and inner diameters. Using high-speed photography, DIC measurements, and dynamic pressure transducers, the progression of deformation and damage during collapse as well as the local pressure history throughout the implosion event is characterized for each specimen type. The completion of this study has resulted in the following conclusions:

Differences in the dominating failure mechanisms present in each material produce significant differences in the pressure pulse released during the implosion of GFRP composite tubes.

Due to the enhanced brittle nature of their failure, coupled with less energy intensive damage modes, the collapse of braided tubes results in the release of a pressure wave with a significantly greater impulse, implying an increased damage potential to nearby structures as compared to filament-wound tubes.

Continuous Wavelet Transform (CWT) is used to identify the frequency signatures of the pressure pulse released by the implosion events, and shows the acoustic signals generated by braided specimens possess significantly greater high-frequency content than filament-wound specimens.

References

- [1] Esmaeel, Ramadan A., Mohamed A. Khan, and Farid Taheri. "Assessment of the Environmental Effects on the Performance of FRP Repaired Steel Pipes Subjected to Internal Pressure." *J. of Press. Vessel Technol.* 134.4 (2012): 041702.
- [2] Mouritz, A.P, E. Gellert, P. Burchill, and K. Challis., 2001. "Review of Advanced Composite Structures for Naval Ships and Submarines," *Compos. Struct.* 53(1), pp. 21-42.
- [3] Urick, R.J., 1963. "Implosions as sources of underwater sound," *J. Acoust. Soc. Am.* 35, pp. 2026–2027. DOI: 10.1121/1.1918898
- [4] Orr, M., and Schoenberg, M., 1976. "Acoustic signatures from deep water implosions of spherical cavities," *J. Acoust. Soc. Am.* 59, pp. 1155–1159.
- [5] Turner, S.E., 2007. "Underwater Implosion of Glass Spheres," *J. Acoust. Soc. Am.* 121, pp. 844–852.
- [6] Ling, J., Bishai, M., Diwan, M., Dolph, J., Kettell, S., Sexton, K., Sharma, R., Simos, N., Stewart, J., Tanaka, H., Viren, B., Arnold, D., Tabor, P., Turner, S., Benson, T., Wahl, D., Wendt, C., Hahn, A., Kaducak, M., Mantsch, P., Sundaram, S.K., 2013. "Implosion chain reaction mitigation in underwater assemblies of photomultiplier tubes," *Nucl. Instrum. Methods Phys. Res. Sect. Accel. Spectrometers Detect. Assoc. Equip.* 729, pp. 491–499.

- [7] Harben, P.E., and Boro, C., 2001. "Implosion Source Development and Diego Garcia Reflections," Presented at the 23rd Department of Defense/Department of Energy Seismic Research Review, Jackson Hole, Wyoming.
- [8] Turner, S. E., and Ambrico, J.M., 2012. "Underwater Implosion of Cylindrical Metal Tubes," *J. Appl. Mech.* 80(1), pp 1-11.
- [9] Farhat, C., C. G. Wang, A. Main, S. Kyriakides, L. H. Lee, K. Ravi-Chandar, and T. Belytschko., 2013. "Dynamic Implosion of Underwater Cylindrical Shells: Experiments and Computations," *Int. J. Solids Struct.* 50(19), pp. 2943-961.
- [10] Ikeda C.M., Wilkerling J., Duncan J.H., 2013. "The Implosion of Cylindrical Shell Structures in a High-pressure Water Environment," *Proc. of the R. Soc. A: Math, Phys. and Eng. Sci.*, 469(2160).
- [11] Moon, C.J., In-Hoon K., Bae-Hyeon C., and Jin-Hwe K., Choi J.H., 2010. "Buckling of Filament-wound Composite Tubes Subjected to Hydrostatic Pressure for Underwater Vehicle Applications," *Compos. Struct.* 92(9), pp. 2241-251.
- [12] Ross C.T.F., Little A.P.F., Haidar Y., and Waheeb A.A., 2009. "Buckling of Carbon/Glass Composite Tubes Under Uniform External Hydrostatic Pressure," *Strain*, 47, pp. 156-174.
- [13] Smith, P.T., C.T.F. Ross, and A.P.F. Little., 2009. "Collapse of Composite Tubes under Uniform External Hydrostatic Pressure," *J. of Phys.: Conference Series* 181, pp. 156-157.
- [14] Hernández-Moreno, H., B. Douchin, Collombet F., Choqueuse D., and Davies P., 2008. "Influence of Winding Pattern on the Mechanical Behavior of Filament-wound Composite Tubes under External Pressure," *Compos. Sci. and Technol.* 68(3-4), pp. 1015-024.

- [15] Olivas, J. D., K. Ravi-Chandar, J. Bustillos, and Craigie, L., 1996. "Buckling of Filament-Wound Cylindrical Vessels Subjected to External Pressure." *J. of Press. Vessel Technol.* 118(2), pp 216.
- [16] Hur, S.H., Son H.J, Kweon J.H., and Choi J.H., 2008. "Postbuckling of Composite Tubes under External Hydrostatic Pressure," *Compos. Struct.* 86(1-3), pp. 114-24.
- [17] Yang, C., Pang S.S., and Zhao Y., 1997. "Buckling Analysis of Thick-Walled Composite Pipe under External Pressure," *J. Compos. Mater.* 31.4, pp. 409-26.
- [18] Ramirez, Guillermo, and Michael D. Engelhardt. "Experimental Investigation of a Large-Scale Composite Riser Tube Under External Pressure." *J. of Press. Vessel Technol.* 131.5 (2009): pp 1-8.
- [19] Pinto, M., Gupta, S., Shukla, A. "Study of Implosion of Carbon/Epoxy Composite Hollow Cylinders Using 3-D Digital Image Correlation." *Compos. Struct.* 119 (2014): pp 272–286.
- [20] Sutton, M.A., Orteu J.J., and Schreier H.W., *Image Correlation for Shape, Motion and Deformation Measurements: Basic Concepts, Theory and Applications.* New York, NY: Springer, 2009.
- [21] Gupta, S., Parameswaran, V., Sutton, M.A., Shukla, A. "Study of Dynamic Underwater Implosion Mechanics using Digital Image Correlation." *Proc. of the Royal Soc. A*, 470.2172 (2014), DOI: 10.1098/rspa.2014.0576.
- [22] Koudela, K.L., and Strait L.H., 1993. "Simplified Methodology for Prediction of Critical Buckling Pressure for Smooth-Bore Composite Cylindrical Shells," *J. Reinf. Plast. Compos.* 12.5, pp. 570-83.

- [23] Von Mises R., 1929. "The critical external pressure of cylindrical tubes under uniform radial and axial load," translated by D. F. Windenburg. Stodolas Festschr, pp. 418–430.
- [24] "ABAQUS 6.12 Analysis User Manual". Internet Manual. Dassault Systèmes Simulia Corp., Providence, RI, 2012.
- [25] Cole, R.H. *Underwater Explosions*. Princeton: Princeton Univ., 1948.
- [26] Fugal, D.L. *Conceptual Wavelets in Digital Signal Processing*. San Diego, CA: Space & Signals Technical Pub., 2009.
- [27] Sridharan, Srinivasan. *Delamination Behaviour of Composites*. Cambridge, England: Woodhead, 2008.
- [28] Brennen, Christopher E. *Cavitation and Bubble Dynamics*. New York: Oxford UP, 1995.
- [29] Kyriakides, S., and Netto, T.A., 2000. "On the Dynamics of Propagating Buckles in Pipelines." Int. J. Solids Struct. 37(46-47), pp. 6843-867.
- [30] Harte, A.M., and Fleck, N.A., 2000. "On the Mechanics of Braided Composites in Tension," Eur. J. of Mech. - A/Solids 19(2) , pp. 259-75.
- [31] Turner S.E., 2004. "Small-scale implosion testing of glass and aluminum cylinders," NUWC-NPT technical memorandum 04-061, Naval Undersea Warfare Center Division, Newport, RI
- [32] Reid, W.D., 1996. "The Response of Surface Ships to Underwater Explosions," Tech. no. DSTO-GD-0109. Melbourne: DSTO Aeronautical and Maritime Research Laboratory.
- [33] Inman, D.J. *Engineering Vibration*. Upper Saddle River, NJ: Prentice Hall, 2001.

Chapter 3 : Experimental Investigation on Underwater Buckling of Thin-walled Composite and Metallic Structures

by

Michael Pinto, Helio Matos, Sachin Gupta, and Arun Shukla

has been published in the Journal of Pressure Vessel Technology

Corresponding Author: Arun Shukla

Dynamic Photo Mechanics Laboratory

Department of Mechanical, Industrial and Systems Engineering

University of Rhode Island

206 Wales Hall, 92 Upper College Rd Kingston, RI, 02881,

USA Phone: +1-401-874-2283

Email Address: shuklaa@uri.edu

ABSTRACT

An experimental study on the underwater buckling of composite and metallic tubes is conducted to evaluate and compare their collapse mechanics. Experiments are performed in a pressure vessel designed to provide constant hydrostatic pressure through the collapse. Filament-wound carbon-fiber/epoxy, glass/polyester (PE) tubes, and aluminum tubes are studied to explore the effect of material type on the structural failure. 3-D Digital Image Correlation technique is used to capture the full-field deformation and velocities during the implosion event. Local pressure fields generated by the implosion event are measured using dynamic pressure transducers to evaluate the strength of the emitted pressure pulse. The results show that glass/PE tubes release the weakest pressure pulse, and carbon/epoxy tubes release the strongest upon collapse. In each case, the dominating mechanisms of failure control the amount of flow energy released.

Introduction

The implosion of a sealed, thin-walled structure occurs when external pressure reaches a critical value, causing an instability, and resulting in the rapid collapse of the structure. During this collapse, the surrounding fluid accelerates, causing a drop in local pressure. The complete collapse of the structure causes the opposite walls to make contact with each other leading the walls and contact fluid to quickly arrest. This abrupt change in momentum of fluid releases a pressure wave of considerable strength into the surrounding fluid. [1-4].

The problem of implosion has been studied from many decades, with some of the first work focusing on using emitted pressure pulses as explosive-less underwater acoustic sources [3-5]. Recently, there has been a renewed interest in implosion due to a 2001 accident in Japan at Super-Kamiokande neutrino observatory. In this accident, the implosion of a single photomultiplier tube released a shockwave powerful enough to trigger a chain reaction of collapse, resulting in the implosion of nearly 7000 adjacent tubes, causing \$20-30m of damage [6]. This accident led to multiple efforts to characterize the pressure pulse emitted during collapse of glass spheres, as well as their potential to damage nearby structures [7,8]. The implosion of aluminum tubes has also gained attention from researchers in the Naval community. Turner and Ambrico identified key stages of the implosion event in relation to the local pressure about the collapsing structure [2]. Also in this work, robust fluid-structure computational models were developed which agreed with the experimental data. Farhat et al. studied the implosion of aluminum tubes with varying L/D ratios to produce both mode 2 and mode 4 failures, and used these experiments to verify computational models [9]. Most recently, Ikeda et. al studied the free-field implosion of aluminum and brass tubes with varying geometries. This work examined

the effect of different modes of collapse on the emitted pressure pulse, and used bubble dynamic scaling to compare these changes [10].

In comparison, the implosion of composite structures has received fairly little attention. Several analytical treatments exist on the subject, but few experimental studies have been performed.

Moon et al. examined implosion of filament-wound carbon/epoxy composite tubes with different winding angles both experimentally and computationally to determine critical buckling pressures and collapse modes [11]. Both Ross and Smith performed experiments on carbon/E-glass tubes to determine critical buckling pressure, collapse modes, and create design tables [12, 13].

Hernandez-Moreno et al. studied the effects of winding pattern on the collapse pressure in filament-wound glass/epoxy composite tubes [14]. Hur et al. examined the buckling modes, loads, and ply failure of carbon/epoxy tape layup tubes both experimentally and computationally [15]. Yang et al. developed an analytic model for critical buckling pressure based on anisotropic laminate theory and performed experiments on E-glass/epoxy tubes to verify predictions [16].

However, in none of these studies is the pressure pulse from the collapse measured, nor are high speed images of the collapse event captured. Previous work by the current authors aimed to address this gap in knowledge by examining the pressure pulses emitted during the collapse of carbon-fiber and glass-fiber reinforced composite tubes and capturing full-field displacements during the implosion events [17, 18]. These studies showed that the implosion of carbon/epoxy and glass/PE tubes also produces similar pressure waves as seen earlier [2,9], and the type of composite architecture used in the materials plays a significant role in determining the strength of the that wave. However, it is still not clear how the implosion pulse released from composite structures differs from metallic structures.

The use of composites has attracted attention in underwater marine applications due to the array of advantages offered by these materials. Composite materials offer alternatives with reduced weight, improved corrosion resistance, and for submerged structures, greater potential operating depths in comparison to metallic structures. In addition, these materials provide improved stealth qualities by having very low thermal, acoustic, and magnetic signatures, increasing their appeal for military applications. For these reasons, the presence of composite materials in marine industries is increasing, and they are currently used in several naval applications, such as sonar domes, masts, and hull sheathings [19]. One of the biggest obstacles to widespread adaptation of composite materials is a lack of complete understanding and simple design rules for these materials, especially under extreme loading conditions [19]. For this reason, the present work looks to expand the current knowledge of composites and the implosion problem by characterizing the differences in the mechanics of collapse and local pressure fields in the implosion of tubes of composite and metallic materials.

Experimental Details

Specimen Geometry

The impodable volumes in this study are aluminum 6061-T6 tubes, and carbon/epoxy and glass/polyester (PE) filament wound composite tubes. The carbon/epoxy tubes consist of seven layers of unidirectional carbon fabric reinforcement arranged in a $[\pm 15/0/\pm 45/\pm 15]$ layup with a 60.3mm inner diameter and a 381mm unsupported length. These cylinders are manufactured by Rock West Composites (West Jordan, UT) with a nominal wall thickness of 1.63mm and are thoroughly sanded for excellent surface finish and tolerances. The glass/PE tubes consist of five layers of unidirectional E-glass fabric reinforcement arranged in a $[\pm 55/\pm 55/0]$ layup with a 57.2mm inner diameter and 381mm unsupported length. These cylinders are manufactured by

Nor'Easter Yachts (Milford, CT) with a nominal wall thickness of 2mm. The reinforcements for both composite tubes are continuous, micron diameter filaments. Aluminum 6061-T6 tubes were cut from commercially available extruded tubing, with an inner diameter of 61.5mm, a wall thickness of 1.24mm, and a length of 381mm. The dimensions are selected to provide specimens with a relatively low collapse pressure, and a high radius-to-thickness ratio so that thin-wall assumptions may be utilized.

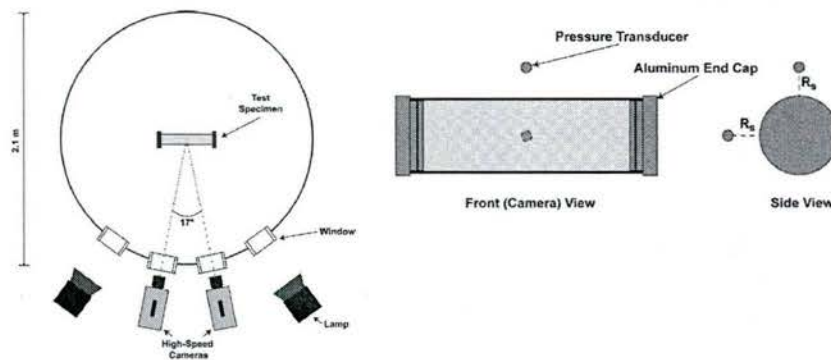


Figure 1: Experimental facility (left) and test specimen configuration (right)

All implosion experiments are conducted in a 2.1m diameter spherical pressure vessel, designed to provide constant hydrostatic pressure throughout the collapse event (see Figure 1). Several acrylic windows mounted about the midspan of the pressure vessel allow the specimens to be viewed by high-speed cameras and adequately lit by two high-powered lights.

The specimens are sealed using two aluminum end caps, and are then suspended horizontally in the center of the pressure vessel. To measure the changes in local pressure during the collapse event, several high pressure blast transducers (PCB 138A05, PCB Piezotronics, Inc., Depew, NY) are mounted along the axis of the tube at a standoff distance equal to the diameter of the

tube. The conditioned signal outputs of the sensors are recorded by an Astro-med Dash® 8HF-HS portable data recorder (Astro-Med Inc., West Warwick, RI) at a sampling rate of 2 MHz.

The vessel is then flooded with filtered water, leaving a small air pocket at the top. Once the vessel is filled, nitrogen gas is introduced into the air pocket to pressurize the enclosed water. The pressure inside the vessel is increased at a gradual rate (0.083 MPa/min) until the specimen collapsed. At this point, the cameras and pressure transducers are end triggered to record the data occurring 1 second prior to triggering. In this way, data is collected for the entire collapse event by all recording devices.

2.2 DIC Technique

Prior to experiments, a random, high-contrast speckle pattern is applied by hand to a region spanning the entire length of the specimen and approximately half of the circumference using flat black and white paint. Features of the pattern were made sufficiently large as to occupy at least 3x3 pixels in the recorded images for optimal DIC measurements. Two high-speed cameras (Photron SA1, Photron USA, Inc.) positioned at a stereo angle of 17°, are used to capture images of the patterned region of the specimen at a frame rate of between 40,000 and 50,000 frames/second. The stereo images are analyzed using a commercially available DIC software, VIC3D 2012 (Correlated Solutions, Inc., Columbia, SC) to measure full-field displacements/velocities across the viewable surface of the specimen. 3-D Digital image correlation (DIC) is a well known non-contact optical technique to determine real-time, full-field displacements across the viewable surface of a specimen [20]. This technique is calibrated for underwater experiments based on previous work [21] for confidence in the accuracy of measured displacements and velocities. Using the referenced calibration method, in-plane and out-of-plane displacements may be determined within 1.2% and 2.5% error, respectively.

In the Section 3, DIC data is presented as color map contours of displacements/velocities along the length of the tube over time. A horizontal line is drawn, parallel to the length axis of the tube, and at the center of its viewable area, and data is extracted from points along this line for each successive recorded image. In this way, a contour plot could be generated showing the evolution of displacement and velocity across the length of the structure throughout the event. For the "Axial Position" axis in these plots, zero represents the longitudinal center of the tube.

Flow Energy

In order to define an energy term to evaluate the strength of the implosion pulse, assumptions must be made about the shape of the pulse. During the implosion, the flow of water rushes toward the center of the structure, converging approximately where initial wall contact occurs. Therefore the high pressure wave emitted from the abrupt change in water momentum also initiates at the center of the specimen. This leads to an approximately spherical wave originating at the point of wall contact. Turner et. al have demonstrated the spherical nature of the implosion wave in experiments on the collapse of aluminum tubes [2]. For these reasons, a spherical wave assumption is made, allowing the development of energy analysis based off of underwater explosion theory.

In many cases, the area under the pressure-time curve (pressure-impulse) is an important parameter to determine the strength of pressure pulse [22]. This parameter combines the effect of both pressure magnitude and the duration of that pulse to evaluate the damage potential of the pressure pulse. This area directly relates to the flow energy of the local pressure pulse generated in the implosion event. This flow energy is calculated for the underpressure region of each specimen type. Here, the energy flux through a surface at distance, R , up to an arbitrary time, t , is defined simply as [23]:

$$E_F = \frac{1}{2\rho_0 R_s} \left[\int_0^t \Delta p dt \right]^2 \quad (1)$$

Where Δp is the dynamic pressure at time t , R_s is the standoff distance, and ρ_0 is the density of the fluid. Knowing that the time integral of pressure is equal to impulse, I , the above may be simplified to:

$$E_F = \frac{I^2}{2\rho_0 R_s} \quad (2)$$

To find the total flow energy, a spherical wave is assumed and the flux is multiplied by the area of an imaginary sphere with radius equal to the standoff distance of the pressure sensor as follows:

$$E_A = 4\pi R_s^2 E_F \quad (3)$$

To normalize this measure for differences in the collapse pressure of different materials, the total flow energy is divided by the potential hydrostatic energy available just prior to the collapse, defined as:

$$E_H = P_{cr} V_{tube} \quad (4)$$

Where P_{cr} is the hydrostatic collapse pressure and V_{tube} is the internal volume of the tube. In this way, the flow energy released in the pressure pulse may be presented as a percentage of the available hydrostatic energy at the collapse pressure.

Due to knowledge of the shape of the pulse, the signal of a single sensor may be used to calculate the flow energy as described above. The sensor at the mid-span is used to calculate this parameter because viscous losses are minimized by reading closer to the source, and higher readings are made closer to the source, improving signal-to-noise ratio.

Results

Table 1: Summary of experimental results

Specimen	Collapse Pressure, P_{cr} (MPa)	P_{min}/P_{cr}	P_{max}/P_{cr}	Maximum Collapse Velocity (m/s)	Pre-Buckling Displacement (mm)
Aluminum	1.68 [± 0.01]	0.69 [± 0.04]	1.70 [± 0.17]	20.0 [± 2.0]	2.5 [± 0.2]
Carbon/Epoxy	0.97 [± 0.03]	0.51 [± 0.05]	2.57 [± 0.56]	16.5 [± 2.3]	1.7 [± 0.5]
Glass/PE	2.05 [± 0.01]	0.84 [± 0.02]	1.24 [± 0.06]	27.2 [± 1.4]	3.9 [± 0.2]

Aluminum Tubes

Aluminum tubes are observed to fail at 1.68 MPa in a mode 2 shape, forming two lobes across the circumference. The local pressure history measured about the midspan of these specimens is seen in Figure 2 and DIC contours of displacement and velocity across the length of the tube are plotted in Figure 3. The DIC contours show the displacement and velocity extracted across a line along the length axis of the tube as shown in the figure.

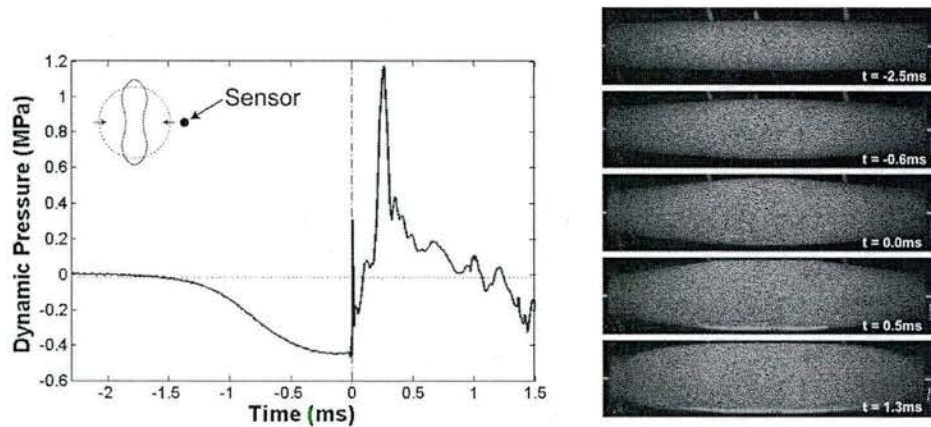


Figure 2: Representative pressure data and high-speed photographs recorded in the implosion of aluminum tubes

The pressure history measured for these specimens is quite consistent with reports of previous studies [2,9,10]. At the start of the collapse, the local pressure decays smoothly to a minimum just prior to $t = 0.00\text{ms}$. This corresponds to an acceleration of the center of the tube to a maximum velocity of 20 m/s, as shown by DIC contours. At $t = 0.00\text{ms}$, contact initiates between opposing walls of the tube, shown by the sudden drop in wall velocity at the center of the tube. This is accompanied by a very sharp spike in the local pressure at this time, indicating the acoustic pulse released due to wall contact. A second acoustic spike is observed as another wall contact is made when the buckle propagated circumferentially. Shortly thereafter, a large spike in pressure is observed with considerable impulse. This pulse is caused by the change in momentum of the surrounding fluid, which accelerated inward along with the walls of the structure. Following this pulse is a lower magnitude pressure tail that corresponds to the axial propagation of the buckle through the length of the tube, as seen in the displacement and velocity contours.

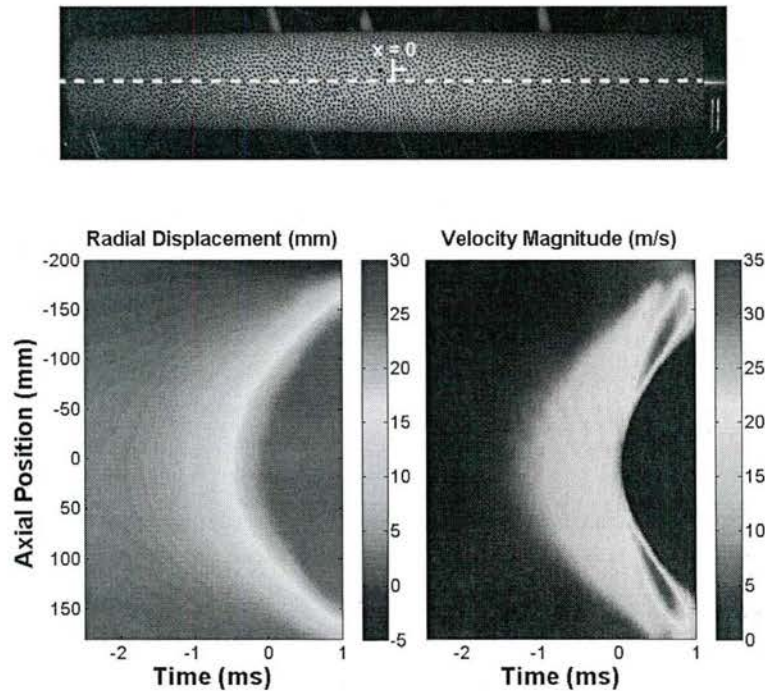


Figure 3: DIC contours of displacement and velocity across the length of aluminum specimens.

Data is extracted from the dotted line shown in the image

An interesting feature seen in the velocity contour is the acceleration of the collapse as the buckle propagates. Starting at approximately $t = 0.2\text{ms}$, the velocity of the region just behind the zero velocity zone increases to 35 m/s, significantly higher than the maximum velocity at the center of the tube

Filament-Wound Carbon

The carbon fiber reinforced specimens fail at 0.97 MPa in a mode 2 buckle shape. The local pressure history measured about the midspan of these specimens and high-speed photographs corresponding to key events are seen in Figure 4. DIC generated contours of radial displacement and velocity along the length of the tube are plotted in Figure 5. The DIC contours show the displacement and velocity extracted across a line along the length axis of the tube as shown in the figure.

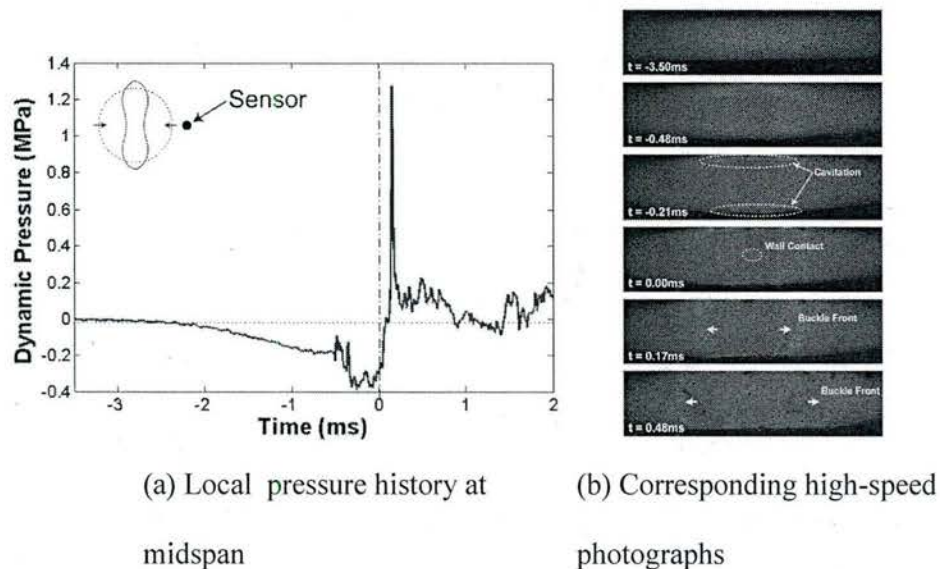
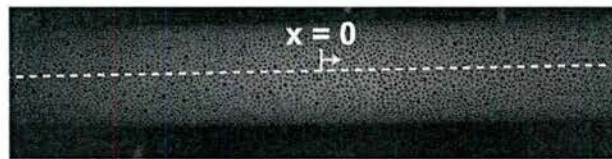


Figure 4: Representative pressure data and high-speed photographs recorded in the implosion of carbon/epoxy tubes.

Initially, the instability is characterized by a smooth and gradual decay in pressure up to $t = -0.5ms$. At this time, a distinct spike in pressure is recorded followed by a sharp drop to a minimum of -0.4 MPa. This spike is a result of longitudinal cracks that initiate at the apexes of the two buckling lobes, releasing an acoustic pulse. This cracking causes a sudden and severe loss of structural stability, allowing the tube walls to accelerate and, consequently, causing a more rapid drop in pressure. The remainder of the underpressure region sustains a minimum pressure, similar to observations made in the implosion of brittle glass tubes by Turner [25]. The drop in pressure seen in this region is sufficient to initiate cavitation near the apexes of the buckle lobes, as highlighted in Figure 4 at $t = -0.21ms$. This phenomenon leads to the formation of cavitation bubbles. These bubbles grow to a critical size and then collapse upon themselves, releasing acoustic pressure pulses upon collapse in the near field which are recorded as minor pressure spikes observed between $t = -0.48ms$ and $t = 0.00ms$.



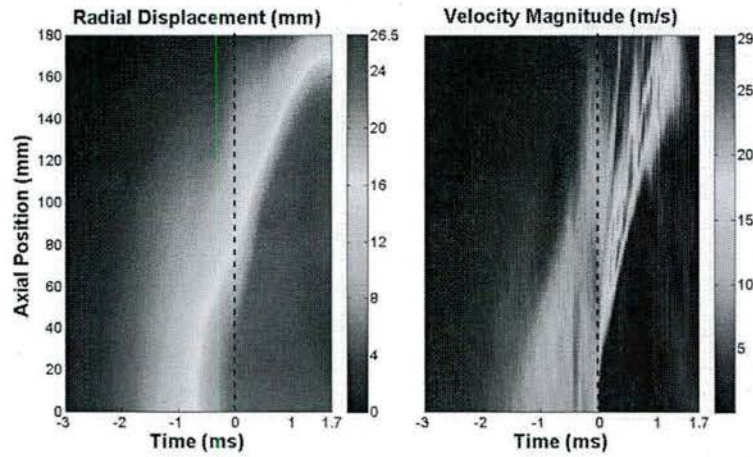


Figure 5: DIC contours of displacement and velocity across the length of carbon/epoxy specimens. Data is extracted from the dotted line shown in the image

Wall-to-wall contact occurs at $t = 0.00\text{ms}$ in the location indicated in the matched high-speed photograph. The occurrence of wall contact is confirmed by the DIC generated velocity contour at that time which shows zero velocity at the center of the specimen. The maximum velocity recorded just prior to wall contact is 16 m/s, which represents the maximum wall velocity in the radial direction.

Following wall contact, pressure rises rapidly to a maximum, and the buckle has begun to propagate axially, as evidenced by the expanded area of zero velocity combined with the greater region of radial displacement close to the inner radius of the tube. After this, the buckle shape continues to propagate through the length of the structure and pressure measurements are dominated by reflected pressure waves from the pressure vessel boundaries.

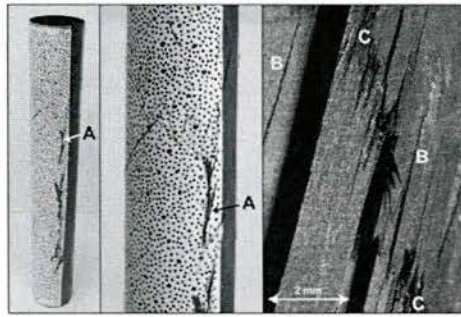


Figure 6: Post-mortem images of carbon/epoxy tubes, showing (A) through-thickness longitudinal cracking, (B) interfibrillar matrix cracking, and (C) fractured fibers

Post-mortem images of these specimens are included in Figure 6. These images show that the dominating mode of failure is nearly exclusively two longitudinal cracks spaced at approximately 180° , corresponding with the lobes of the mode 2 buckling shape. While small amount of circumferential cracking is observed in the vicinity of these larger cracks, they are relatively minor in comparison. Additionally, the tube is seen to regain much of its original shape, and no significant delamination is observed. Optical microscopy of the fracture surfaces show the major cracks are aligned parallel with the fiber angle of the outer ply, $\pm 15^\circ$ from the length axis, denoted by "A" in the figure. This implies that these cracks initiated in regions of high tensile strength in the outer ply, and propagated through the relatively weak, resin-rich interfibrillar region parallel to the reinforcing fibers. Fractured fibers in underlying plies are also seen in this micrograph, denoted as "C" in Figure 6. The fracture surfaces of these plies are also parallel to the $\pm 15^\circ$ outer ply, showing that the cracking initiated in the outer ply retains its original orientation as it propagates through the thickness of tube. In addition, the large gaps seen in the micrograph show that these longitudinal cracks did indeed penetrate through the thickness of the tube.

Filament-Wound Glass

Filament-wound glass fiber specimens fail at 2.05 MPa in a mode 2 buckling shape. The tubes flatten completely during the dynamic failure event, but are seen to rebound to a nearly circular shape following the depressurization. The local pressure history measured about the midspan of these specimens and high-speed photographs are included in Figure 7. DIC generated contours of radial displacement and velocity along the length of the tube are plotted in Figure 8. The DIC contours show the displacement and velocity extracted across a line along the length axis of the tube as shown in the figure.

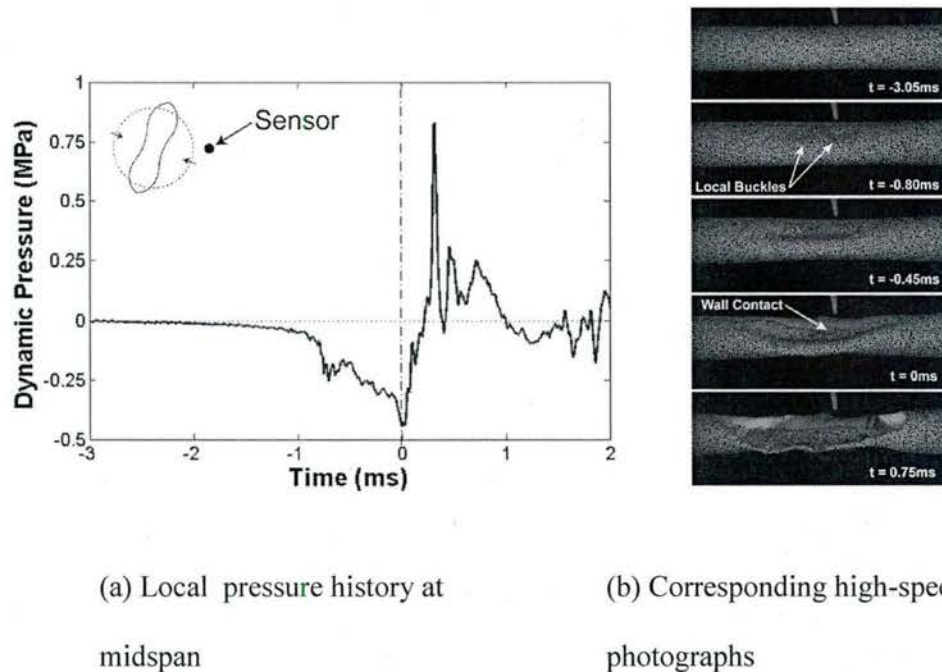


Figure 7: Representative pressure data and high-speed photographs recorded in the implosion of glass/PE tubes

Qualitatively, this pressure trace at first appears to be similar to those measured for aluminum tubes with a gradual decay in pressure followed by a pressure spike and a broad overpressure

region. However, the underpressure region shows some unique characteristics not present in metallic tubes.

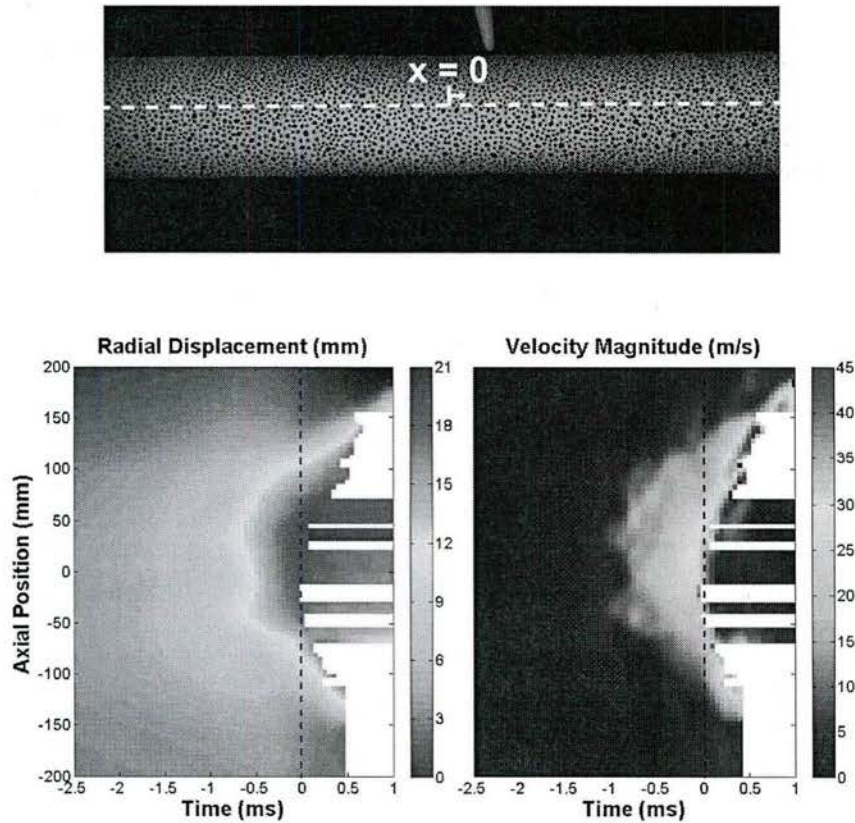


Figure 8: DIC contours of displacement and velocity across the length of glass/PE specimens.

White regions indicate loss of correlation due to material damage. Data is extracted from the dotted line shown in the image

Prior to the dynamic collapse, these specimens begin to oval significantly in a quasi-static manner. The DIC displacement data shows a maximum radial deflection of 3.9mm (13.6% of

initial radius) at $t = -3.05ms$. From the start of the dynamic event to $t = -0.80ms$, a slow and gradual decay in pressure is observed, as reflected in the slow ovaling seen in this period. The unstable rapid collapse initiates after $t = -0.80ms$, where a sharp drop in pressure is seen. In the corresponding high-speed photograph, as well as the DIC contours, it is observed that multiple local buckles form at this time, creating regions of high velocity, which results in a steep drop in local pressure.

These local buckles converge into a single global buckle at $t = -0.45ms$, as evidenced by the high-speed images and DIC contours, and pressure continues to drop at a near-constant rate as the center of the tube accelerates to a maximum velocity of 27m/s. At $t = 0.00ms$, wall contact is made and is followed by a small acoustic pulse and subsequent high magnitude pressure pulse recorded at $t = 0.30ms$, similar to the previous cases.

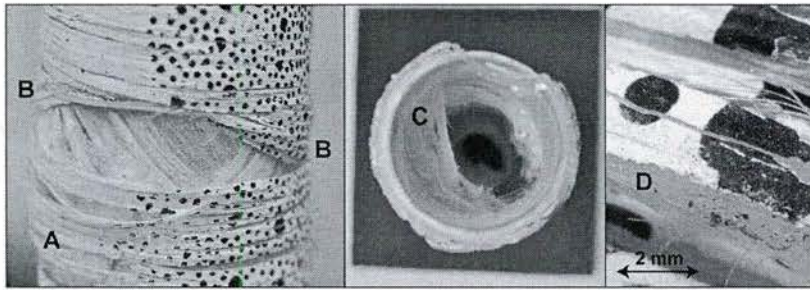


Figure 9: Post-mortem images for glass/PE specimens, showing (A) matrix cracking, (B) delamination of outer hoop ply, (C) delamination of inner helical ply, and (D) long pulled-out glass fibers

Post-mortem images of RT specimens, shown in Figure 9, give a clear view of the types and scales of damage incurred in this material type. In these images, the damage is overwhelmingly delamination, matrix cracking, and fiber pull-out. Delamination of the outer- ply exposes the

helical plies beneath, and much of the inner-most ply has delaminated and is seen pushed in on the interior of the tube. Composites with unidirectional reinforcement are typically weak in terms of delamination as compared to other reinforcement types, as the reinforcing plies simply lay upon one another with little inter-ply interaction [26]. For this reason, when the tubes experience large deformations during collapse, delamination initiates in the early stages of the event and continues to propagate. Optical micrographic investigation of the fracture surface also shows very long intact glass fibers protruding from fracture surfaces. This shows that fiber pull-out plays a significant role in the failure of these tubes. These major modes of damage explain the many jumps and changes in slope in the underpressure region. The nature of the underpressure region can be compared with the physical "stick-slip" phenomenon seen in the delamination of composite materials and in fiber pull-out [26].

Discussion

Suction Region

One of the most striking differences between the pressure profiles of these specimens is in the underpressure or suction region occurring as the specimen walls accelerate inward. This region is plotted for all material types in Figure 10. The underpressure region for aluminum specimens shows a very smooth decay in pressure up until wall contact is made. This reflects the near constant acceleration of the tube walls without damage until the end of the collapse. Glass/PE tubes also possess a relatively smooth decay in pressure; however there are some small jumps, or changes in slope, corresponding with the "stick-slip" nature of delamination which dominates the failure of these structures [26].

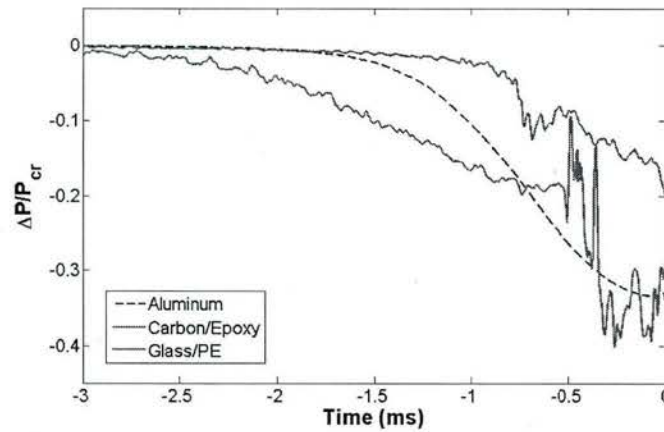


Figure 10: Comparison of underpressure regions for different material types

In contrast to both previous specimens, the underpressure regions for carbon/epoxy specimens appears to have two distinct phases: a fairly slow and smooth decay up to approximately $t = -0.5$ ms followed by a very steep drop in pressure and then a fluctuating plateau region up until wall contact. This difference is a result of different damage mechanisms caused by the differences in reinforcing fibers. For glass-reinforced tubes, damage initiates from the very beginning stages of collapse, mainly in the form of matrix cracking and delamination, which is the reason for the "stick-slip" nature of the underpressure region as previously discussed.

The difference in these damage mechanics is a result of differences in the behavior of carbon and glass fibers. Carbon fibers exhibit significantly greater tensile modulus and tensile strength than glass fiber, while glass fibers possess higher failure strains in both tensile and compressive loading [26]. The enhanced stiffness of carbon fibers allows tubes reinforced with this material to have higher collapse pressures than glass-reinforced tubes of the same wall thickness. The greater failure strain of glass fibers causes fiber pull-out and delamination to dominate the damage progression of these composites, as these mechanisms are able to initiate prior to fiber

failure. Conversely, the more brittle carbon fibers fractured before other more energy intensive damage mechanisms could take over. This causes the failure of carbon fiber tubes to be significantly more catastrophic in nature than glass fiber tubes.

Pressure Parameters

The relevant quantitative parameters of the pressure history are summarized for each material type in Table 1. As the collapse pressures differ between materials, the minimum and maximum values of dynamic pressure are normalized by the critical pressure. It is seen that the carbon/epoxy tubes result in the lowest minimum pressure and highest peak pressure, while glass/PE tubes have the highest minimum pressure and lowest peak pressure. This suggests that the collapse of carbon/epoxy tubes is significantly more dramatic than the other two materials, causing more extreme changes to local pressure. This gives some evidence that carbon/epoxy tubes release the strongest pressure waves and glass/PE the weakest.

Total Flow Energy

For the relatively long duration of the collapse of some of these specimens, the overpressure region may be corrupted by reflections of the underpressure region from the tank walls. To overcome this limitation, fluid dynamics may be used, detailed in previous work by the authors [17,18,21]. Here it was shown that the negative impulse of the underpressure region should be equal in magnitude to the positive impulse of the overpressure region. This phenomenon has been observed in several studies on the implosion of glass spheres as well as the implosion of aluminum tubes [2,9,21]. In the present study the impulse of the underpressure region is calculated, and it is assumed that its magnitude will be equivalent to that of the impulse released in the pressure pulse. This will then be used to calculate flow energy following Equations 2 and 3.

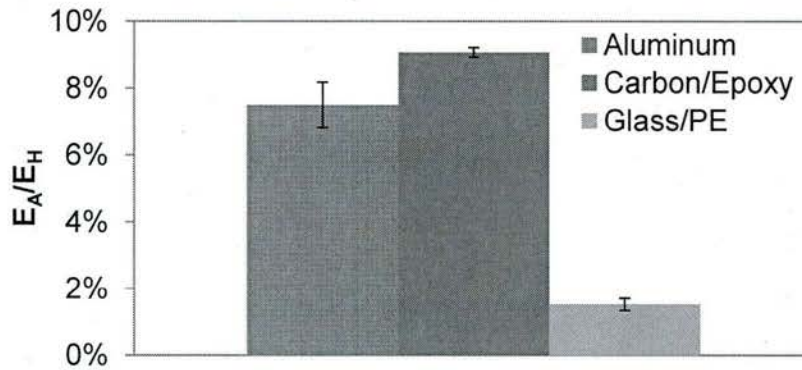


Figure 11: Flow energy as a percentage of potential hydrostatic energy for each material type

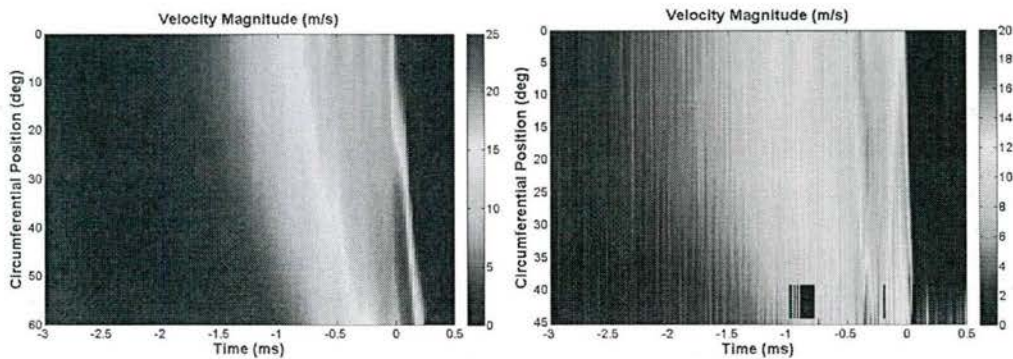
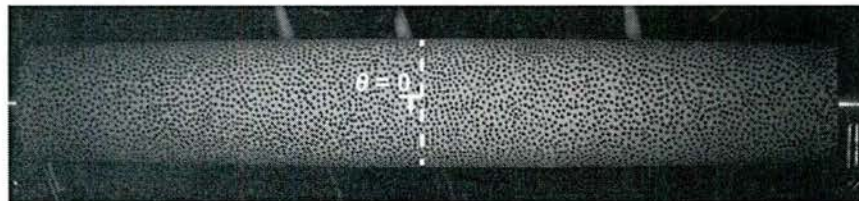
The flow energy as a percentage of the total available hydrostatic potential energy is plotted for the different material cases in Figure 11. The first observation is that the collapse of carbon/epoxy tubes results in a 20% stronger pressure pulse than the collapse of aluminum tubes, as a percentage of hydrostatic energy. This implies that more energy is dissipated in the deformation and failure of aluminum tubes than carbon/epoxy tubes. This is consistent with the post mortem analysis of the specimens. Carbon/epoxy tubes experience a largely brittle failure, with two through-thickness axial cracks at the lobes of the buckling shape, while in contrast, aluminum tubes experience large scale plastic deformation. The new surface area created in cracking the carbon/epoxy tubes is relatively small compared to the amount of plastic deformation experienced in metallic tubes. This indicates that significantly more energy is absorbed in the plastic deformation of aluminum tubes than in the brittle failure of carbon/epoxy tubes, thereby reducing the energy released in the form of the pressure pulse.

Conversely, the energy released in the collapse of glass/PE tubes is by far the least of all specimens studied presently: 80% less than aluminum tubes and 85% less than carbon/epoxy tubes. Post mortem analyses show that the failure of glass/PE tubes is dominated by

delamination and fiber pull-out. These are very energy intensive processes, and cause less residual energy to be released in the pressure pulse than either of the other materials under study.

Circumferential DIC Results

The DIC contours of velocity across the circumference of the midspan of aluminum and carbon/epoxy tubes are plotted in Figure 12. In these plots, a circumferential position of "0" is the location at which buckling is first initiated and where primary wall contact is made, and data is extracted from the dotted line shown in the image. Due to excessive damage, correlated data is not available for the full visible circumference of glass/PE tubes, so this analysis will focus on unique aspects of the carbon/epoxy tubes alone.



(a) DIC contour of aluminum
tube

(b) DIC contour of
carbon/epoxy tube

Figure 12: DIC contours of velocity across the circumference of the center of aluminum and carbon/epoxy tubes. Data is extracted from the dotted line shown in the image

A clear difference between the velocity profiles of these two materials exists. For aluminum tubes, the specimen begins to accelerate from the center and continues to accelerate until wall contact occurs at $t = 0\text{ms}$. At this time, the velocity at the center point rapidly drops to zero and that zero velocity region quickly spreads to cover the entire visible circumference as the tube flattens. For carbon/epoxy tubes, the velocity contour appears quite similar at first, with the velocity picking up at the center point first and then continuing to accelerate. However, at $t = -0.5\text{ms}$, the velocity at the center point appears to stall between 10 and 12 m/s, while simultaneously localized regions of very high velocity appear towards the edges of the visible area, with magnitudes of up to 20m/s. Examining high-speed images, it is seen that this coincides with the appearance of through-thickness longitudinal cracks along the lobes of the buckling shape. This shows that the cracking causes a loss in stability, resulting in rapid acceleration of the region near those cracks. This in turn is responsible for the previously discussed cavitation on the surface of the specimen occurring at this time, as a sudden increase in velocity will cause a proportional drop in pressure.

Conclusions

The hydrostatic implosion of metallic and composite tubes is studied to examine differences caused by material type. High-speed photography, DIC measurements, and dynamic pressure sensors are used to characterize the mechanisms of collapse for each case, and to evaluate the

strength of the emitted pressure wave. The completion of this work has resulted in the following important conclusions:

- The mechanics of the implosion of composite tubes differ greatly from the collapse of aluminum tubes due to complex damage mechanisms characteristic of composite materials.
- The collapse of carbon/epoxy tubes results in the release of significantly stronger pressure pulses than aluminum and glass/PE tubes due to the enhanced brittle nature of their failure.
- The flow energy can be obtained directly as a function of pressure and is a good representation for the total energy emitted during the implosion process.
- Due to the energy intensive damage processes involved in the failure of glass/PE tubes, the energy released in the pressure pulse is much less than that for the case of aluminum and carbon/epoxy tubes.

Acknowledgements

The authors would like to acknowledge the Office of Naval Research and Dr. Yapa D.S. Rajapakse for providing financial support to conduct this research under Grant No.s N00014-10-1-0662 and N00014-15-1-2046.

References

- [1] Turner SE. Underwater Implosion of Glass Spheres. J Acoust Soc Am 2007; 121: 844–852.
- [2] Turner SE, Ambrico JM. Underwater Implosion of Cylindrical Metal Tubes. J Appl Mech 2012; 80(1): 1-11

- [3] Urick, R.J., 1963. "Implosions as sources of underwater sound," J. Acoust. Soc. Am. 35, pp. 2026–2027. DOI: 10.1121/1.1918898
- [4] Orr, M., and Schoenberg, M., 1976. "Acoustic signatures from deep water implosions of spherical cavities," J. Acoust. Soc. Am. 59, pp. 1155–1159.
- [5] Harben PE, Boro C. Implosion Source Development and Diego Garcia Reflections. Presented at the 23rd Department of Defense/Department of Energy Seismic Research Review, Jackson Hole, WY, 2-5 October 2001.
- [6] Accident grounds neutrino lab - physicsworld.com [WWW Document], n.d. URL <http://physicsworld.com/cws/article/news/2001/nov/15/accident-grounds-neutrino-lab> (accessed 2.10.14).
- [7] Ling J, Bishai M, Diwan M, Dolph J, Kettell S, Sexton K, Sharma R, Simos N, Stewart J, Tanaka H, Viren B, Arnold D, Tabor P, Turner S, Benson T, Wahl D, Wendt C, Hahn A, Kaducak M, Mantsch P, Sundaram SK. Implosion chain reaction mitigation in underwater assemblies of photomultiplier tubes. Nucl Instrum Methods Phys Res Sect Accel Spectrometers Detect Assoc Equip 2013; 729: 491–499.
- [8] Diwan, Milind, Jeffrey Dolph, Jiajie Ling, Rahul Sharma, Kenneth Sexton, Nikolaos Simos, Hidekazu Tanaka, Douglas Arnold, Philip Tabor, and Stephen Turner. "Underwater Implosions of Large Format Photo-multiplier Tubes." Physics Procedia 37 (2012): 715-21.
- [9] Farhat, C., C. G. Wang, A. Main, S. Kyriakides, L. H. Lee, K. Ravi-Chandar, and T. Belytschko., 2013. Dynamic Implosion of Underwater Cylindrical Shells: Experiments and Computations. Int. J. Solids Struct. 50.19, 2943-961.

- [10] Ikeda CM, Wilkerling J, Duncan JH. The Implosion of Cylindrical Shell Structures in a High-pressure Water Environment. *Proc of the R Soc A: Math, Phys and Eng Sci* 2013; 469: 2160
- [11] Moon CJ, In-Hoon K, Bae-Hyeon C, Jin-Hwe K, Choi JH. Buckling of Filament-wound Composite Tubes Subjected to Hydrostatic Pressure for Underwater Vehicle Applications. *Compos Struct* 2010; 92(9): 2241-251.
- [12] Ross CTF, Little APF, Haidar Y, Waheeb AA. Buckling of Carbon/Glass Composite Tubes Under Uniform External Hydrostatic Pressure. *Strain* 2009; 47: 156-174.
- [13] Smith PT, Ross CTF, Little APF. Collapse of Composite Tubes under Uniform External Hydrostatic Pressure. *J of Phys: Conference Series* 2009; 181: 156-157.
- [14] Hernández-Moreno H, Douchin B, Collombet F, Choqueuse D, Davies P. Influence of Winding Pattern on the Mechanical Behavior of Filament-wound Composite Tubes under External Pressure. *Compos Sci and Technol* 2008; 68(3-4): 1015-024.
- [15] Hur SH, Son HJ, Kweon JH, Choi JH. Postbuckling of Composite Tubes under External Hydrostatic Pressure. *Compos Struct* 2008; 86(1-3): 114-24.
- [16] Yang C, Pang SS, Zhao Y. Buckling Analysis of Thick-Walled Composite Pipe under External Pressure. *J Compos Mater* 1997; 31(4): 409-26.
- [17] Pinto, M., Gupta, S., Shukla, A. "Study of Implosion of Carbon/Epoxy Composite Hollow Cylinders Using 3-D Digital Image Correlation." *Compos. Struct.* 119 (2014): pp 272–286.
- [18] Pinto M, Gupta S, Shukla A. Hydrostatic Implosion of GFRP Composite Tubes Studied by Digital Image Correlation. *J of Press Vess Technol* 2015: 051302.

- [19] Mouritz, A.P, E. Gellert, P. Burchill, and K. Challis., 2001. "Review of Advanced Composite Structures for Naval Ships and Submarines," *Compos. Struct.* 53(1), pp. 21-42.
- [20] Sutton MA, Orteu JJ, Schreier HW. *Image Correlation for Shape, Motion and Deformation Measurements: Basic Concepts, Theory and Applications*. New York, NY: Springer, 2009.
- [21] Gupta S, Parameswaran V, Sutton MA, Shukla A. A study of Underwater Implosion using Digital Image Correlation, *Proc of the R Soc A* 2014; 470(2172): 20140576.
- [22] Cole RH. *Underwater Explosions*. Princeton: Princeton Univ., 1948.
- [23] Arons A, Yennie D. Energy Partition in Underwater Explosion Phenomena. *Rev of Mode Phys* 1948; 20(3): 519-36.
- [24] Kyriakides, S., and Netto, T.A., 2000. "On the Dynamics of Propagating Buckles in Pipelines." *Int. J. Solids Struct.* 37(46-47), pp. 6843-867.
- [25] Turner SE (2004) Small-scale implosion testing of glass and aluminum cylinders. NUWC-NPT technical memorandum 04-061, Naval Undersea Warfare Center Division, Newport, RI
- [26] Sridharan, Srinivasan. *Delamination Behaviour of Composites*. Cambridge, England: Woodhead, 2008.
- [27] Wonderly, Christopher, Joachim Grenestedt, Göran Fernlund, and Elvis Čepus. "Comparison of Mechanical Properties of Glass Fiber/vinyl Ester and Carbon Fiber/vinyl Ester Composites." *Composites Part B: Engineering* 36.5 (2005): 417-26.

Chapter 4 : Dynamic Collapse Mode Evolution in Carbon Composite Tubes

by

Michael Pinto and Arun Shukla

has been published in Extreme Mechanics Letters

Corresponding Author: Arun Shukla

Dynamic Photo Mechanics Laboratory

Department of Mechanical, Industrial and Systems Engineering

University of Rhode Island

206 Wales Hall, 92 Upper College Rd Kingston, RI, 02881,

USA Phone: +1-401-874-2283

Email Address: shuklaa@uri.edu

ABSTRACT

An experimental study on the hydrostatic implosion of carbon-fiber reinforced epoxy composite tubes is conducted to explore unique failure and damage mechanisms of collapse. Experiments are performed in a pressure vessel designed to provide constant hydrostatic pressure through the collapse. Filament-wound carbon-fiber/epoxy tubes are studied using high-speed photography to explore the effect of complex damage on the modes of failure. 3-D Digital Image Correlation technique, which is first calibrated for the underwater environment, is used to capture the full-field deformation and velocities during the implosion event. Fourier Series deformation models are used to extract buckling modes from displacement data. The results reveal that the presence of damage in the structure can cause the mode shape to change as the structure deforms.

Introduction

Composite materials have attracted significant attention in underwater marine applications due to their promise of reduced weight, improved corrosion resistance, and for submerged structures, greater potential operating depths. These advantages drive an increase in the presence of these materials in marine industry, such as in sonar domes, masts, and hull sheathings [1]. One of the greatest obstacles to widespread adaptation of composites is a lack of complete understanding of these materials, especially under extreme loading conditions [1]. Recent work by the authors has sought to expand the current knowledge of composite behavior by examining the problem of implosion [2].

An implosion is a structural failure that can happen to a thin-walled structure that contains a low pressure fluid and is subjected to high external pressure. When the external pressure reaches a critical value, instability in the structure occurs, resulting in a rapid and often catastrophic collapse. During this collapse, the boundaries of the structure and surrounding fluid are accelerated to high velocities and suddenly stop once the collapse is completed. This abrupt change in momentum releases a pressure wave into the surrounding fluid, which can damage nearby structures[3-5]. The implosion of glass spheres as well as metallic tubes has been studied by several authors who characterized the pressure pulse emitted during collapse as well as the mechanics of the collapse itself [5-10]. However, significantly less understanding exists of the implosion of composite materials, and existing studies mainly focused on determining critical pressures [11-14]. In none of these studies were deformations studied in real-time during the implosion event.

This work seeks to expand understanding of the mechanics of the collapse of composite tubes by investigating the dynamic evolution of the collapse shape throughout the implosion event, and in

the presence of damage. It is demonstrated that due to changes in stiffness brought about by large-scale damage, the collapse shape may change dramatically, which can have consequences in the resulting pressure field.

Materials

The composite structures in this study are filament-wound carbon/epoxy tubes with an inner diameter of 60.3mm. These tubes consist of seven layers of unidirectional carbon fabric reinforcement arranged in a $[\pm 15/90/\pm 45/\pm 15]$ layup, and are manufactured by Rock West Composites (West Jordan, UT) with a nominal wall thickness of 1.52mm and an unsupported length of 279.4mm. The dimensions are selected as to provide specimens with a relatively low expected collapse pressure, and a high R/t ratio (>18) so that thin-wall assumptions may be used. Two experiments are performed in this series to demonstrate repeatability.

Experimental Procedure

A 2.1m diameter spherical pressure vessel with a maximum pressure rating of 6.89MPa is used to provide constant hydrostatic pressure to perform implosion experiments. Several Plexiglass windows mounted about the midspan of the pressure vessel allow the specimens to be viewed by high-speed cameras and adequately lit by two high intensity lights.

Prior to set-up, all composite tube specimens are sealed using aluminum end caps. The specimen is suspended in the center of the pressure vessel using several steel cables. A random, high-contrast speckle pattern is applied to a region covering the entire length of the specimen and approximately half of the circumference using flat black paint. Two high-speed cameras (Photron SA1, Photron USA, Inc.), offset by 17° are used to capture stereo images of the

patterned region of the specimen at 36,000 frames/s throughout the implosion event. The stereo images are analyzed using commercially available image correlation software, VIC3D.

3-D Digital image correlation (DIC) is a well known experimental tool used to determine real-time, full-field displacements across the viewable surface of a specimen [15]. This technique is calibrated for underwater experiments based on previous work [16] for confidence in the accuracy of measured displacements and velocities. Using the referenced calibration method, in-plane and out-of-plane measurements may be determined within 1.2% and 2.5% error, respectively.

The vessel is then flooded with water that is filtered for maximum optical clarity, leaving a small air pocket at the top. Once the vessel is filled, nitrogen gas is introduced into the air pocket to pressurize the vessel. The pressure inside the vessel is increased at a gradual rate (0.083 MPa/min) until the specimen collapses, at which time the data acquisition system is triggered.

Results and Discussion

The two composite tubes in this study collapsed dynamically at a hydrostatic pressure of 1.54MPa and 1.66MPa. The collapse pressures and the process of collapse in both the tubes were very similar, thus, data is presented of a single representative case. Upon completion of the implosion, the tubes are seen to collapse in a completely flat mode 2 shape (see Fig. 1).

However, it is observed in high-speed images that deformation initiates in a higher order shape early in the event. In addition, post-mortem inspection revealed three longitudinal, through-thickness cracks spaced evenly about the circumference of the tubes at 120° intervals (see Fig. 1). This damage pattern implies a mode 3 collapse shape, which is characterized by three

symmetric lobes of maximum deflection spaced at equal intervals about the circumference of the tube (see Fig. 1).

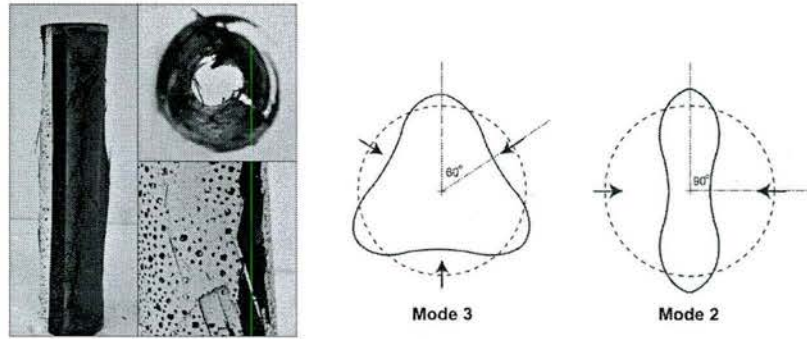


Figure 1: Post-mortem of imploded carbon/epoxy tube (left) and illustrations of buckling mode shapes (right)

FEA of this specimen, as reported in previous work [2], reproduces the observed critical pressure with excellent accuracy, but also predicts a pure mode 3 collapse shape. This represents the initial stages of collapse quite well, but fails to capture the fully flattened shape of the final collapse. To address these apparent contradictions, DIC is used to generate displacement contours for the entire surface for each recorded image.

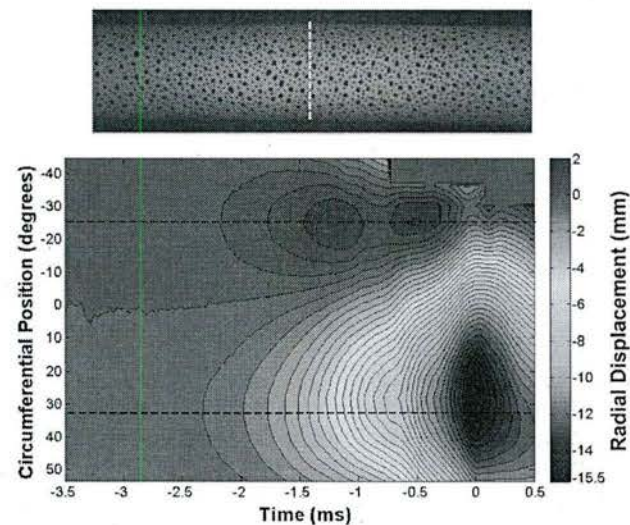


Figure 2: (Bottom) Contour of radial displacement across the midspan of the tube through the implosion event. Location of data indicated by the dashed line in the top image

The radial displacement across the visible circumference of the tube at its midspan is plotted over the duration of the implosion event in Fig. 2. The dashed line in the image in Figure 2 illustrates where data was extracted from. In this figure, $t = 0\text{ms}$ represents the moment of wall contact at the center of the tube.

In this figure, additional evidence of the observed mode-switching phenomenon is found. Between $t = -3\text{ms}$ and $t = -1\text{ms}$, there appears to form a lobe of positive displacement and a valley of negative displacement separated by approximately 60° . A pure mode 3 buckling shape consists of three lobes equally spaced around the circumference of the tube by 120° . This implies that the separation between a lobe and adjacent valley would be 60° (Fig. 1), showing that in the initial stages of deformation, the tube conforms to a mode 3 shape. Following this time, the lobe centered at $\theta = 32^\circ$ appears to spread until it covers the majority of the visible circumference at $t = 0\text{ms}$. This gives evidence that as one lobe begins to dominate the viewable surface, a mode 2 deformation pattern dominates the structure.

To further examine the evolution of the mode shape during collapse, a Fourier Series decomposition of the displacement at each time step is performed. Using thin-wall assumptions, the radial displacement of the tube at a certain axial location as a function of angular position is [18]:

$$u_r(\theta) = a_0 + a_1 \cos(w\theta) + b_1 \sin(w\theta) \quad \text{Eq. (1)}$$

Where a_0 , a_1 , and b_1 are constants relating to the magnitude of displacement, and w is the mode number of the buckling shape. The model of Eq. 1 is fit to the displacement profile taken from each image, recorded at $28\mu\text{s}$ intervals, using a least-squares fitting algorithm. In this way, the constants of the model could be extracted for each time step in the deformation history. The

primary constant of interest for this analysis is the mode number, w , and the value for this parameter is plotted against time in Fig. 3.

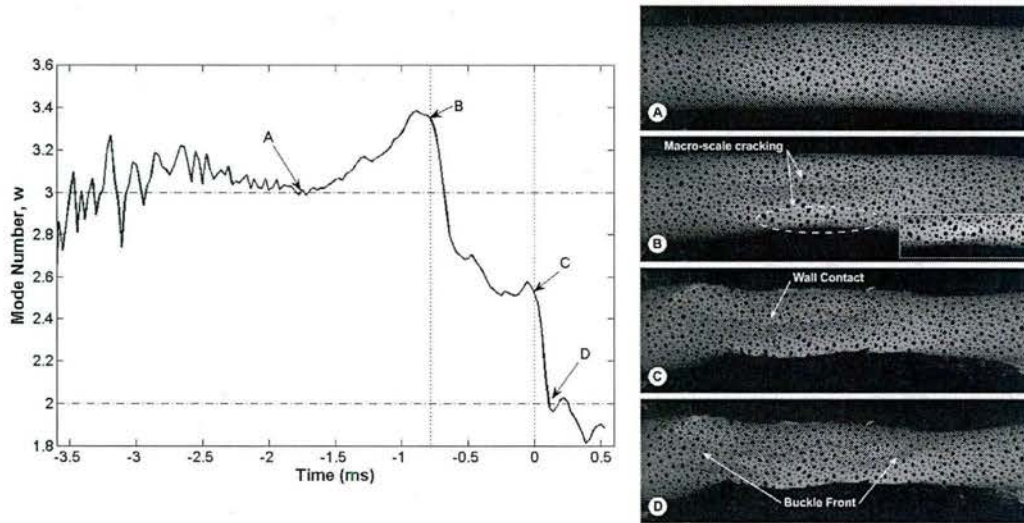


Figure 3: Mode number, w , over the collapse event (left) and corresponding high-speed images (right)

From the beginning of the collapse event until time B (~ 0.8 ms prior to wall contact), the mode number, w , remains approximately 3. This demonstrates that up until this time, the structure deforms in a mode 3 buckling shape, as inferred by the deformation contour and the matched high-speed images (image A in Fig. 3). Following time B, there is a dramatic change in the mode number, as it falls sharply and appears to settle at about 2.5 just before time C. This suggests that during this time period, the structure begins to transition from a pure mode 3 to a lower mode. The cause of this transition can be found by examining the high-speed image corresponding to time B. At this time, macro-scale cracks appear in several locations on the surface of the tube. Zooming in and increasing contrast on image B in Fig. 3 shows that this damage initiates as interfibrillar cracks parallel to fibers in the outer ply, which then coalesce to form through-thickness cracks. This effectively reduces the stiffness of the structure, changing the mechanics

of the deformation. The result is a rapid acceleration of the tube walls and a transition of the mode shape.

At time C in the deformation history, the next major change in the mode number is observed. Here, mode number again drops steeply, settling to ~ 2 for the remainder of the implosion event. This indicates the end of the transition region of the previous time period, completing the reduction of the deformation shape. Time C corresponds to $t = 0\text{ms}$ which is the moment at which opposing walls of the tube contact each other. This shows that following wall contact, the tube flattens in a perfect mode 2 shape which then propagates along the length of the specimen (see image D).

Since the proposed phenomenon of collapse in this study is a structural response, it depends both on the geometry of the structure as well as the composite material lay-up and properties. In previous work by the authors [2], carbon/epoxy tubes of the same layup and wall thickness were studied with different length-to-diameter ratios. Mode transition during collapse was seen only in tubes with the geometry discussed here. This mode change during collapse is important when considering the damage potential of the shockwave emitted from these structures. It was shown in previous work that composite tubes collapsing in higher modes release a comparably weaker pressure pulse than lower modes [2]. By transitioning to a mode 2 collapse shape, the implosion of these tubes could release a significantly stronger pressure pulse than would be expected if it remained a mode 3. The particular pressure pulse released in the collapse of these tubes may also be found in reference [2].

Conclusions

The hydrostatic implosion of filament-wound carbon/epoxy composite tubes is studied for specimens experiencing a dynamic mode change. Using high-speed photography and DIC measurements, the progression of deformation and damage during collapse throughout the implosion event is characterized and tied to the evolution of the mode shape. The completion of this study has resulted in the following conclusions:

- Due to the onset of damage, carbon/epoxy tubes of certain geometries may experience a change in mode shape during collapse.
- For this special case, the collapse may be divided in to three time domains: (i) pure mode 3 in an undamaged state, (ii) a transition region after damage has initiated, and (iii) pure mode 2 following wall contact.
- This change in mode shape is not predicted by simple numerical tools, and it can have significant effects on the resulting local pressure field in the surrounding fluid.

Acknowledgements

The authors would like to acknowledge the Office of Naval Research and Dr. Yapa D.S. Rajapakse for providing financial support to conduct this research under Grant No. N00014-10-1-0662

References

- [1] Mouritz AP, Gellert E, Burchill P, Challis K. Review of Advanced Composite Structures for Naval Ships and Submarines. *Compos Struct* 2001; 53(1): 21-42.
- [2] Pinto M, Gupta S, Shukla A. Study of Implosion of Carbon/Epoxy Composite Hollow Cylinders Using 3-D Digital Image Correlation. *Compos Struct* 2014; 119: 272–286.

- [3] Urlick RJ. Implosions as sources of underwater sound. *J Acoust Soc Am* 1963; 35: 2026–2027.
- [4] Orr M, Schoenberg M. Acoustic signatures from deep water implosions of spherical cavities. *J. Acoust. Soc. Am* 1976; 59: 1155–1159.
- [5] Turner SE. Underwater Implosion of Glass Spheres. *J Acoust Soc Am* 2007; 121: 844–852.
- [6] Accident grounds neutrino lab - physicsworld.com [WWW Document], n.d. URL <http://physicsworld.com/cws/article/news/2001/nov/15/accident-grounds-neutrino-lab> (accessed 2.10.14).
- [7] Ling J, Bishai M, Diwan M, Dolph J, Kettell S, Sexton K, Sharma R, Simos N, Stewart J, Tanaka H, Viren B, Arnold D, Tabor P, Turner S, Benson T, Wahl D, Wendt C, Hahn A, Kaducak M, Mantsch P, Sundaram SK. Implosion chain reaction mitigation in underwater assemblies of photomultiplier tubes. *Nucl Instrum Methods Phys Res Sect Accel Spectrometers Detect Assoc Equip* 2013; 729: 491–499.
- [8] Harben PE, Boro C. Implosion Source Development and Diego Garcia Reflections. Presented at the 23rd Department of Defense/Department of Energy Seismic Research Review, Jackson Hole, WY, 2-5 October 2001.
- [9] Turner SE, Ambrico JM. Underwater Implosion of Cylindrical Metal Tubes. *J Appl Mech* 2012; 80(1): 1-11.
- [10] Ikeda CM, Wilkerling J, Duncan JH. The Implosion of Cylindrical Shell Structures in a High-pressure Water Environment. *Proc of the R Soc A: Math, Phys and Eng Sci* 2013; 469: 2160

- [11] Moon CJ, In-Hoon K, Bae-Hyeon C, Jin-Hwe K, Choi JH. Buckling of Filament-wound Composite Tubes Subjected to Hydrostatic Pressure for Underwater Vehicle Applications. *Compos Struct* 2010; 92(9): 2241-251.
- [12] Ross CTF, Little APF, Haidar Y, Waheeb AA. Buckling of Carbon/Glass Composite Tubes Under Uniform External Hydrostatic Pressure. *Strain* 2009; 47: 156-174.
- [13] Smith PT, Ross CTF, Little APF. Collapse of Composite Tubes under Uniform External Hydrostatic Pressure. *J of Phys: Conference Series* 2009; 181: 156-157.
- [14] Hur SH, Son HJ, Kweon JH, Choi JH. Postbuckling of Composite Tubes under External Hydrostatic Pressure. *Compos Struct* 2008; 86(1-3): 114-24.
- [15] Sutton MA, Orteu JJ, Schreier HW. Image Correlation for Shape, Motion and Deformation Measurements: Basic Concepts, Theory and Applications. New York, NY: Springer, 2009.
- [16] Gupta S, Parameswaran V, Sutton MA, Shukla A. A study of Underwater Implosion using Digital Image Correlation, *Proc of the R Soc A* 2014; 470(2172): 20140576.
- [17] ABAQUS 6.12 Analysis User Manual. Internet Manual. Dassault Systèmes Simulia Corp., Providence, RI, 2012.
- [18] Hoo Fatt MS, Pothula SG. Dynamic Pulse Buckling of Composite Shells Subjected to External Blast. *Compos Struct* 2010; 92(7): 1716-727.

Chapter 5 : Mitigation of Pressure Pulses from Implosion of Hollow Composite (CFRP) Cylinders

by

Michael Pinto and Arun Shukla

has been published in the Journal of Composite Materials

Corresponding Author: Arun Shukla

Dynamic Photo Mechanics Laboratory

Department of Mechanical, Industrial and Systems Engineering

University of Rhode Island

206 Wales Hall, 92 Upper College Rd Kingston, RI, 02881,

USA Phone: +1-401-874-2283

Email Address: shuklaa@uri.edu

ABSTRACT

An experimental study on the underwater collapse of composite tubes with polymeric coatings is conducted in an attempt to mitigate the implosion pressure pulse released. Experiments are performed in a pressure vessel designed to provide constant hydrostatic pressure during collapse. Filament-wound carbon-fiber/epoxy tubes are studied with polyurea coatings of different thicknesses on the interior and exterior of the tube to explore the effects of these configurations on implosion pulse mitigation. 3-D Digital Image Correlation (DIC) technique is used to capture the full-field deformation and velocities during the implosion event. Local pressure fields generated by the implosion event are measured using dynamic pressure transducers to evaluate the strength of the emitted pressure pulses. Local pressure data and DIC results are used to obtain a measure of normalized energy released during implosion. Results show that thick interior coatings significantly reduce the energy released in the pressure pulse by slowing the collapse and softening the initial wall-to-wall contact. In contrast, thick exterior coatings increase this energy by suppressing damage, thereby reducing the energy absorption capacity of the structure.

Introduction

The implosion of a thin-walled cylinder occurs when an applied external pressure reaches a critical value, resulting in the rapid collapse of the structure. During this collapse, the contacting fluid is accelerated, causing a drop in local pressure via Bernoulli's Principle. When opposing walls of the structure make contact with one another their velocities rapidly drop to zero. This abrupt change in momentum is transferred to the surrounding fluid, causing the release of a pressure wave, which can have considerable strength [1, 2].

The pulse released following an implosion has been studied for many decades, with some of the first work focusing on explosive-less underwater acoustic sources [3-5]. Recently, interest in implosion has been rekindled due to a 2001 accident in a Japanese neutrino observatory. Here, at the Super-Kamiokande facility, the implosion of a single photomultiplier tube released a shockwave powerful enough to trigger a chain reaction of collapses, resulting in the implosion of nearly 7000 adjacent tubes, causing \$20-30m of damage [6]. This accident reinvigorated efforts to characterize the pressure pulse released during the collapse of glass spheres and tube structures, as well as their potential to damage nearby structures [7,8]. Turner and Ambrico identified key stages of the implosion event in relation to the local pressure about the collapsing structure and developed robust fluid-structure computational models which agreed with experimental data [2]. Farhat et al. studied the implosion of aluminum cylinders with varying lengths to produce both mode 2 and mode 4 failures, and used these experiments to verify computational models [9]. Most recently, Ikeda et. al studied the free-field implosion of aluminum and brass tubes with varying geometries, to examine the effect of collapse mode on the emitted pressure pulse [10].

Over the past decade, attention has shifted toward the implosion of composite structures as interest in using these materials in marine applications has increased. Several authors performed both experimental and analytic studies to determine critical collapse pressures and mode shapes for composite tubes under external hydrostatic pressure [11-16]. More recently, the authors have performed experimental studies on the hydrostatic collapse of composite tubes, with special attention given to measurements of real-time deformations and local pressure history. The hydrostatic implosion of both carbon-fiber and glass-fiber composite tubes was characterized for different geometries and reinforcement architecture [17,18]. This work was then extended to study the shock-initiated implosion of composite tubes to reveal failure mechanisms unique to these materials [19]. However, no studies have been performed to mitigate the pressure pulse released in the collapse of these materials. This study seeks to address this problem with the addition of polymeric layers.

In recent decades, several authors have examined the usefulness of polymeric coatings on blast mitigation in composite materials, particularly polyurea (PU). Tekalur et al. [20] studied E-Glass composites coated with PU subjected to air blast loading, and showed that the coating reduced deflection and damage levels as compared to the uncoated material. Sandwich composites have also been studied with PU interlayers by multiple authors. Bahei-El-Din et al. [21] showed PU interlayers reduce the kinetic energy and core damage as compared to control panels. Gardner et al. [22] studied the effect of location of the PU in relation to a graded foam core in sandwich composites, and showed PU layers located near the back face of the panel dramatically improved blast resistance.

This study seeks to mitigate the strength of the pressure pulse released in the implosion of composite tubes using PU coatings. Layers of controlled thicknesses were applied to

carbon/epoxy tubes on both the interior and exterior of the tube to determine the effect of coating thickness on the composite structure. Results show that thick interior coatings significantly reduce the energy released in the pressure pulse, at the cost of an increase in overall mass of the structure. Surprisingly, thick exterior coatings increase the energy released, thus making the collapse more dangerous. These findings provide useful guidelines in the design of marine composite structures susceptible to implosion.

Experimental Details

The impodable volumes studied are filament wound carbon/epoxy composite tubes. The carbon/epoxy tubes consist of seven layers of unidirectional carbon fabric reinforcement arranged in a $[\pm 15/0/\pm 45/\pm 15]$ layup with a 60mm inner diameter and a 381mm unsupported length. This layup gives the structure an effective hoop modulus of 73 GPa, and an effective axial modulus of 27 GPa. These values were determined using classical laminate theory in conjunction with modulus data of a single carbon-epoxy ply. These cylinders are manufactured by Rock West Composites (West Jordan, UT) with a nominal wall thickness of 1.63mm and are thoroughly sanded for excellent surface finish and tolerances. The dimensions are selected as to provide specimens with a relatively low expected collapse pressure, and a high radius-to-thickness ratio so that thin-wall assumptions may be utilized.

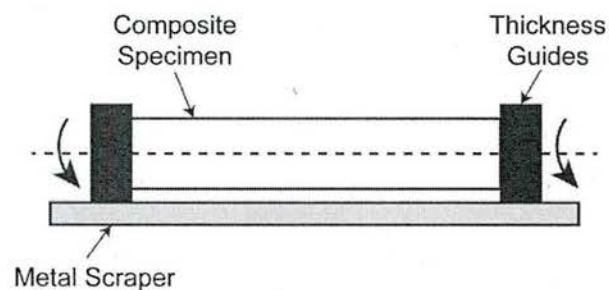


Figure 1: Schematic of polyurea coating fixture. Specimen is rotated as uncured PU is poured by hand. A metal scraper on guides controls the thickness of the applied coating.

Specimens were coated with a two-part polyurea (PU) supplied by Specialty Products, Inc. (Lakewood, WA). The specific blend used was the HM-VK handmix series, which has a long enough gel time to be applied manually. This material has a low stiffness ($\sim 10\text{MPa}$), but very high elongation of approximately 500%. For this reason, polyurea is very attractive for energy absorption applications. A simple fixture was built to coat both exterior and interior of the composite tubes with a controlled thickness of the mixed polymer, and is shown in Figure 1. A small motor continuously rotates the specimen while the PU is applied by hand, and a scraper is used to create the desired thickness. In this study, two coating thicknesses were used: a "thin" coating having equal volume to the tube walls, and a "thick" coating, with double the thickness of the "thin" coating. It should be noted that the interior and exterior coatings have slightly different thicknesses due to their locations on the tube, but their volumes, and therefore masses, are approximately the same (as shown in Table 1).

All implosion experiments are conducted in a 2.1m diameter spherical pressure vessel with a maximum pressure rating of 6.89MPa designed to provide constant hydrostatic pressure throughout the collapse event (see Figure 2). Several Plexiglass windows mounted about the midspan of the pressure vessel allow the specimens to be viewed by cameras and adequately lit by two high-powered lights.

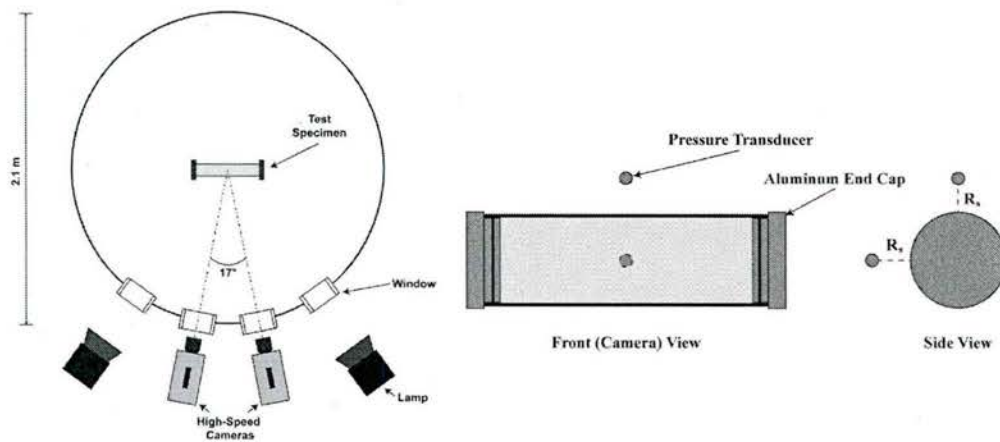


Figure 2: Experimental facility (left) and test specimen configuration (right)

The specimens are sealed using two aluminum end caps and suspended horizontally in the center of the pressure vessel. To measure the changes in local pressure during the collapse event, several high pressure blast transducers (PCB 138A05, PCB Piezotronics, Inc., Depew, NY) are mounted at different locations about the specimen both axially and circumferentially. The amplified outputs of this sensor are monitored by an Astro-med Dash® 8HF-HS portable data recorder (Astro-Med Inc., West Warwick, RI) at a sampling rate of 2 MHz.

The vessel is then flooded with filtered water, leaving a small air pocket at the top. Once the vessel is filled, nitrogen gas is introduced into the air pocket to pressurize the enclosed water. The pressure inside the vessel is increased at a gradual rate (0.083 MPa/min) until the specimen collapses.

DIC Technique

Prior to experiments, a random, high-contrast speckle pattern is applied by hand to a region spanning the entire length of the specimen and approximately half of the circumference using flat black and white paints. Features of the pattern were made sufficiently large as to occupy at least

3x3 pixels in the recorded images for optimal DIC measurements. Two high-speed cameras (Photron SA1, Photron USA, Inc.) positioned at a stereo angle of 17°, are used to capture images of the patterned region of the specimen at a frame rate of 50,000 frames/second. The stereo images are analyzed using commercially available DIC software, VIC3D 7 (Correlated Solutions, Inc., Columbia, SC) to measure full-field displacements across the viewable surface of the specimen. 3-D Digital image correlation (DIC) is a well-known, non-contact optical technique to determine real-time, full-field displacements across the viewable surface of a specimen [23]. This technique was calibrated for underwater experiments based on previous work [24] for confidence in the accuracy of measured displacements and velocities. Using the referenced calibration method, in-plane and out-of-plane displacements may be determined within 1.2% and 2.5% error, respectively.

Total Flow Energy

In many cases, the area under the pressure-time curve is as important as or even more important than the magnitude of the pressure pulse alone [25]. This necessitates a measure that combines the effect of both pressure magnitude and the duration of that pulse to properly evaluate the damage potential of the pressure pulse. For this reason, the flow energy of the local pressure history is calculated for the underpressure region of each specimen type. Here, the energy flux through a surface at distance, R_s , up to an arbitrary time, t , is defined simply as [26]:

$$E_F = \frac{1}{2\rho_0 R_s} \left[\int_0^t \Delta p dt \right]^2 \quad (1)$$

Where Δp is the dynamic pressure at time t , R_s is the standoff distance, and ρ_0 is the density of the fluid. Knowing that the time integral of pressure is equal to impulse, I , the above may be simplified to:

$$E_F = \frac{I^2}{2\rho_0 R_s} \quad (2)$$

To find the total energy, a spherical wave is assumed and the flux is multiplied by the area of an imaginary sphere with radius equal to the standoff distance of the pressure sensor as follows:

$$E_A = 4\pi R_s^2 E_F \quad (3)$$

To normalize this measure for differences in the collapse pressure of different materials, the total flow energy is divided by the potential hydrostatic energy available just prior to the collapse, defined as:

$$E_H = P_{cr} V_{tube} \quad (4)$$

Where P_{cr} is the hydrostatic collapse pressure and V_{tube} is the volume of fluid displaced by the tube. In this way, the flow energy released in the pressure pulse may be presented as a percentage of the available hydrostatic energy at the collapse pressure.

Results and Discussion

All coatings provided a moderate increase in collapse pressure of the structure. The coatings increase both the effective thickness of the tube walls as well as the mass of the structure, thereby altering the critical collapse pressure. Results also show that all coatings have some effect on the minimum and maximum pressures. The details of how these parameters change are discussed in depth in the following sections.

Table 1: Summary of experimental results

Case	% Mass Increase	P_{cr} (MPa)	P_{min} (MPa)	P_{max} (MPa)

Uncoated	N/A	0.97 (± 0.03)	0.52 (± 0.05)	2.5 (± 0.6)
Thin Interior	50 (± 2) %	1.02 (± 0.1)	0.71 (± 0.04)	1.77 (± 0.4)
Thick Interior	90 (± 1) %	1.17 (± 0.1)	0.92 (± 0.09)	1.76 (± 0.2)
Thin Exterior	43 (± 6) %	1.18 (± 0.04)	0.75 (± 0.02)	2.56 (± 0.4)
Thick Exterior	80 (± 6) %	1.2 (± 0.01)	0.73 (± 0.03)	3.38 (± 0.6)

Underpressure Comparison

Previous work by this group has emphasized particular characteristics of the underpressure portion of the pressure history, both to evaluate the strength of the pressure spike released following collapse and to reveal information on the collapse mechanics. The pressure history for each case in this study is plotted in Figures 3 and 4 below. To scale for differences in collapse pressure, classic bubble dynamics was used [27], where a scaled time parameter is defined as:

$$\bar{t} = t/R_i\sqrt{\rho_0/P_{cr}} \quad (5)$$

Where R_i is the internal tube radius. Here, the time is scaled by the collapse time of a spherical bubble with radius R_i , collapsing under an external pressure equal to the collapse pressure of the tube under study. This method of temporal scaling has been used successfully for the implosion of metallic cylinders in recent work [10]. In these plots in Figure 3, $\bar{t} = 0\text{ms}$ represents the moment of wall contact.

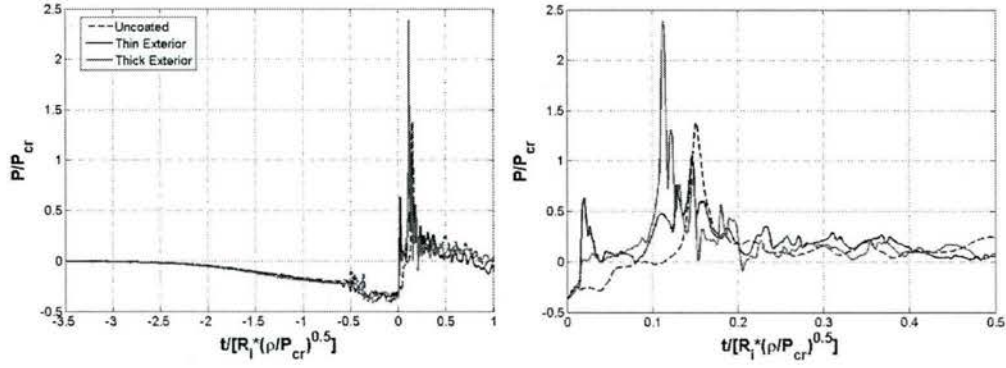


Figure 3: Local pressure histories measured at midspan, normalized by collapse pressure, plotted against dimensionless time for exterior coated specimens. The region from $\bar{t} = 0$ to $\bar{t} = 0.5$ is shown enlarged on the right.

First, it is seen that the exterior coatings (plotted in Figure 3) show little differences from the underpressure of the uncoated specimens. In these cases, there is a two-phase underpressure characteristic of the implosion of carbon composite tubes. The pressure first drops smoothly as the tube deforms without damage. At approximately 0.5ms prior to wall contact, there is a very sudden drop in pressure then a short plateau region up until wall contact is made. This coincides with large-scale damage occurring in the structure. At this time, longitudinal cracks form on the lobes of the buckling shape in regions of high tensile stress. This causes a sudden loss in structural stability and allows for the rapid acceleration of the walls, and consequently, a rapid drop in local pressure. Both thin and thick exterior coatings show these same characteristics and similar minimum pressures, however, it is seen that the thick exterior coating seems to reduce the duration of the second phase. This suggests the exterior coating has some effect on the development of damage, and will be further investigated in the following sections.

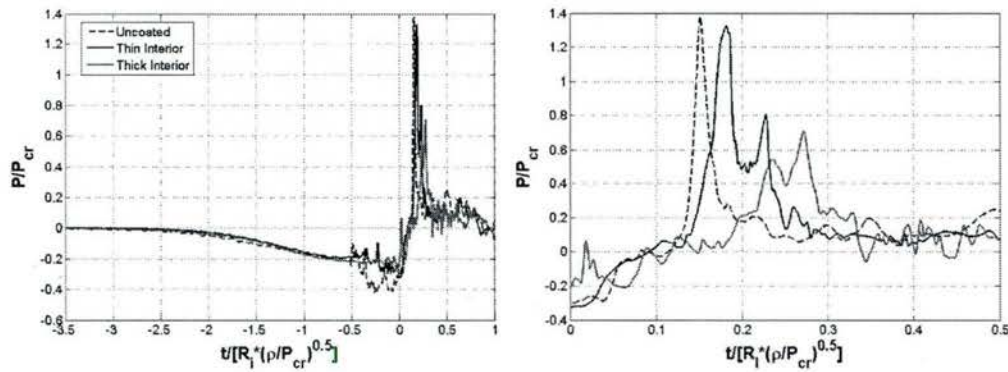


Figure 4: Local pressure histories measured at midspan, normalized by collapse pressure, plotted against dimensionless time for interior coated specimens. The region from $\bar{t} = 0$ to $\bar{t} = 0.5$ is shown enlarged on the right.

In contrast, Figure 4 shows that interior coatings cause quite significant differences in the underpressure region. Some elements of the two-phase characteristic remain, but are significantly altered. Both thin and thick interior coatings reduce the pressure drop seen in this region, with the thicker coating showing an even smaller pressure drop. This suggests that interior PU coatings reduce the acceleration of the structure, and consequently the acceleration of the surrounding fluid, and that increasing the thickness of the coating enhances this effect. In addition, the thick interior coating appears to suppress the second phase of the underpressure associated with damage development.

Overpressure Comparison

Figures 3 and 4 also illustrates changes to the overpressure region brought on by different coating types. For exterior coatings, thin coatings have little effect on the peak pressure, while thick coatings produce a significantly higher magnitude pressure peak. The maximum pressure for the thick exterior coated case is approximately 80% greater than the uncoated case which

gives more evidence that thick exterior coatings actually intensify the collapse of the structure. This appears to be due to a containment of the damage in the structure, and is discussed further in later sections.

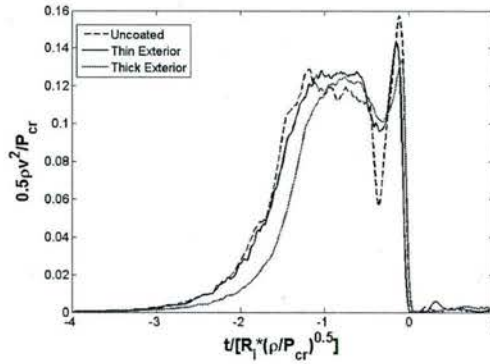
The interior coatings show even more interesting changes to the overpressure. Not only is the magnitude of the pressure pulse altered, but so is the timing of the pulse. As the thickness of the coating increases, the magnitude of the pressure pulse decreases, and the arrival of the pulse is delayed. The mitigation of the peak pressure again gives evidence that these coatings slow the collapse of these tubes, thereby lessening the severity of the pressure pulse. The change in timing of the peak suggests these coatings extend the contact event itself, meaning that it takes longer to arrest the structure and the deceleration of the tube walls is therefore less. This observation is further explored using DIC measurements of velocities of the tubes.

Midpoint Velocity

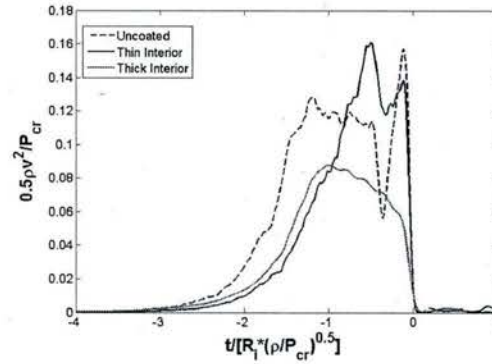
To compare the velocities of these structures during collapse, the data must first be scaled both in terms of velocity magnitude and time to account for differences caused by changing collapse pressure. Time is scaled using Eq. 5 as previously discussed. To scale velocities to account for different collapse pressure, the following dimensionless velocity is defined:

$$\bar{v} = \frac{\rho_0 v^2}{2P_{cr}} \quad (6)$$

Where v is the magnitude of the measured velocity. This dimensionless velocity term is similar to a normalized kinetic energy and removes the effect of pressure on the velocity. The non-dimensional velocity is plotted against non-dimensional time for each case studied in Figure 5 below.



(a) DIC velocity data for exterior coatings



(b) DIC velocity data for interior coatings

Figure 5: Dimensionless velocity measured at specimen midspan plotted against dimensionless time

Examining the midpoint velocities for the exterior coating case, little difference is seen in the velocity profile. Some of the peaked nature of the uncoated velocity is smoothed out, however the magnitudes are roughly the same. The only significant difference seen here is that for the thick exterior coated case, the duration of the plateau region prior to wall contact is shorter than both other cases. This plateau region is caused by large-scale damage occurring in the structure at this time, so it appears as though the thick coating is suppressing that feature of the failure process to some degree.

In contrast, coatings on the tube's interior have a dramatic effect on the midpoint velocity of the structure. Thin interior coatings have little effect on the peak velocity; however the character of the velocity history is significantly different. The plateau region normally associated with damage in the tube is absent, and instead the tube continues to accelerate to its maximum value. Interestingly, the acceleration of interior coated specimens is less than that of uncoated tubes, showing the resistive effect of the coating.

Specimens with thick interior coatings show even more of a difference in midpoint velocity. These specimens exhibit a significantly lower maximum velocity, and the velocity trace has a much more smooth character. Both of these qualities indicate that for this thickness of interior coating, the mechanical behavior of the PU layer begins to dominate the collapse. PU is a highly strain-rate sensitive material, and becomes stiffer as strain rate increases. Therefore, as the collapse accelerates, the PU coating is better able to resist the deformation and reduce the structural velocity.

Midpoint Acceleration

To gain additional insight on the effect of coatings on the mechanics of implosion, the normalized velocity defined previously is numerically differentiated to produce curves of normalized acceleration. The absolute value of acceleration is plotted over normalized time in Figure 6 below.

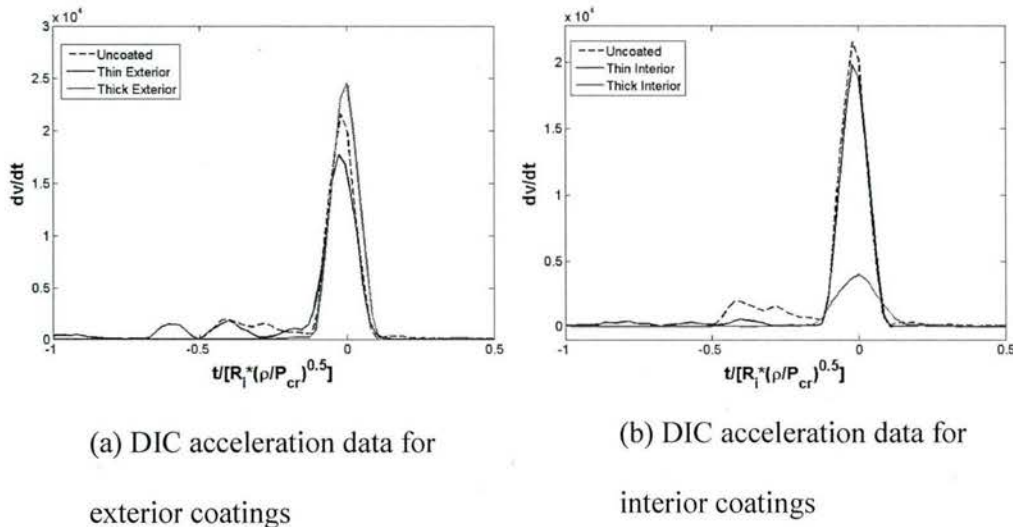


Figure 6: Absolute value of dimensionless acceleration measured at specimen midspan plotted against dimensionless time

Common to all curves in this Figure is the large spike in acceleration occurring at approximately $\bar{t} = 0$, which indicates the extreme deceleration that occurs following wall contact. Examining the plots for exterior coatings, relatively small differences are seen in the peak acceleration at wall contact. Thin exterior coatings show a small reduction, while thick exterior coatings show a small increase in acceleration as compared to the uncoated case. This appears to be related to the peak pressures measured during collapse, where the peak pressure decreases for a thin exterior coating but increases for the thick exterior coating.

Interior coatings show significant differences as compared to uncoated specimens. Thin interior coatings provide reduced peak acceleration, but thick interior coatings drastically reduce acceleration at wall contact. For the thick interior coated case, the peak is much less sharp and has a magnitude of approximately 25% that of the uncoated case. This indicates that this coating not only reduces the speed of the collapse, but also softens the impact at wall contact, causing a less rapid change in momentum. The different character of the velocity profile also suggests that at this thickness, the mechanics of the collapse are dominated by the behavior of the PU layer.

Flow Energy

For the relatively long duration of the collapse of some of these specimens, the overpressure region may be corrupted by reflections of the underpressure region from the tank walls. To overcome this limitation, fluid dynamics may be used, detailed in previous work by the authors [17,18,24]. Here, it was shown that the negative impulse of the underpressure region should be equal in magnitude to the positive impulse of the overpressure region. This phenomenon has been observed in several studies on the implosion of glass spheres as well as the implosion of aluminum tubes [2,9,24]. In the present study the impulse of the underpressure region is calculated, and it is assumed that its magnitude will be equivalent to that of the impulse released

in the pressure pulse. This will then be used to calculate flow energy following Equations 2 and 3. The flow energy as a percentage of the total available hydrostatic potential energy is plotted for the different material cases in Figure 7.

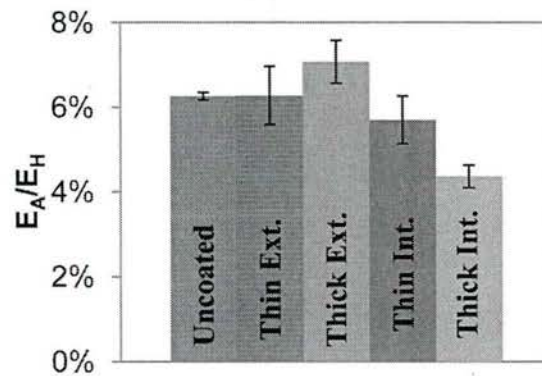


Figure 7: Total flow energy released in the implosion of each case, normalized by potential hydrostatic energy

Starting with thin coatings, it is seen that both interior and exterior coatings show little effect on the flow energy developed. Though there is some change in mean value, any change from the control uncoated case lies within error bars which is consistent with other observations made in previous sections. Both minimum pressure and maximum collapse velocity for thin-coated cases show little difference from the control, suggesting that coatings of this thickness had little effect on the severity of collapse.

Thick coatings, on the other hand, do have a significant effect on the flow energy released. Thick interior coatings show a significant (30%) reduction in flow energy developed in the collapse. This implies that this coating drastically reduces the severity of the collapse, and this is supported by the analyses previously discussed. Tubes with thick interior coatings showed less of a pressure drop, reduced collapse velocity, and lower peak acceleration. All of these factors

contribute to lessening the intensity of the failure event, and in turn reducing the flow energy released.

Conversely, thick exterior coatings show a significant (14%) increase in flow energy. This is somewhat unexpected as the maximum collapse velocity is similar to the uncoated case, however a much higher peak pressure is observed for these cases. To better explain and understand this observation, post-mortem analysis is conducted to examine the states of damage on each case in this study, and this is reported in Section 3.6.

One key question to address in this analysis is whether the change in energy released is due to the coating itself or simply due to the increased mass of the structure. This is answered by the percent increase in mass as reported in Table 1. As seen in this table, the added mass for the thin and thick coatings are approximately the same regardless of the location of the coating, interior or exterior. Though the added mass is the same, the effects on the pressure history, collapse velocity, and energy released are widely different. This shows that these effects are brought on by the specific coating itself rather than simply the added mass of the PU layer.

Effect of Exterior Coatings on Damage

The effects of the exterior PU coatings on the collapse mechanics of composite tubes may be further understood by examining post mortem specimens. For tubes with interior PU coatings, no visible change is observed in damage as compared to the uncoated case. Therefore, this section will examine changes in observed damage for tubes with exterior PU coatings only.

Figure 8 shows typical post mortem images for the case of an uncoated carbon/epoxy tube. The most prominent form of damage seen for these specimens is longitudinal, through thickness cracks, marked as "A" in this figure. These cracks show significant opening, as well as additional

cracking and pullout in adjacent tows. In addition, some circumferential cracking is present, indicated by "B" in the image. These cracks appear less severe than the longitudinal cracks, and initiated as the buckle propagated along the tubes' length.

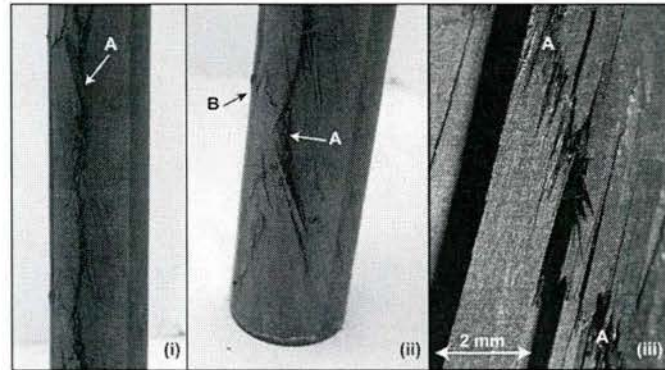


Figure 8: Post-mortem images of uncoated tubes showing (A) through-thickness axial cracks and (B) smaller circumferential cracks

To observe how exterior coatings affect the damage in the structure, the coatings on post mortem specimens are carefully removed while preserving the state of damage on the tube surface. Post mortem images of tubes with a thin exterior coating are shown in Figure 9 below.

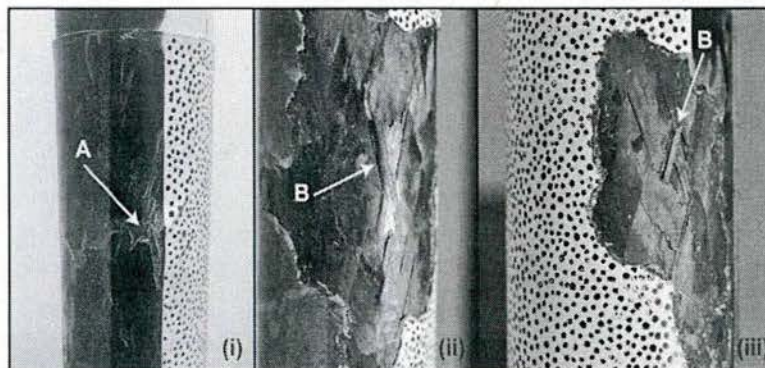


Figure 9: Post-mortem images of tubes with thin exterior coatings showing (A) coating delamination and puncture and (B) axial cracking (note: coating has been peeled to expose composite surface).

On the outside of the coating, areas of delamination of the PU coating are seen where cracks exist in the tube underneath (see A in Figure 9.i). The extreme bending at these sites caused the delamination, and in some cases, the fractured tube then punctured the PU coating. With the coating peeled back, the state of damage underneath is readily visible. Here through-thickness cracks are seen with carbon tows fraying from the surface (labeled as B in Figures 9.ii and 9.iii), which are responsible for rupturing the PU layer. Most importantly, the cracks for this case do not seem as severe as in the uncoated case. Uncoated tubes show much more fraying of carbon tows and opening in the crack faces. This indicates that the thin outer coating has a suppressive effect on the damage in the tube due to the confinement offered by the PU. To examine the effect of thickness on this phenomenon, post mortem images of tubes with a thick exterior coating are shown in Figure 10 below.

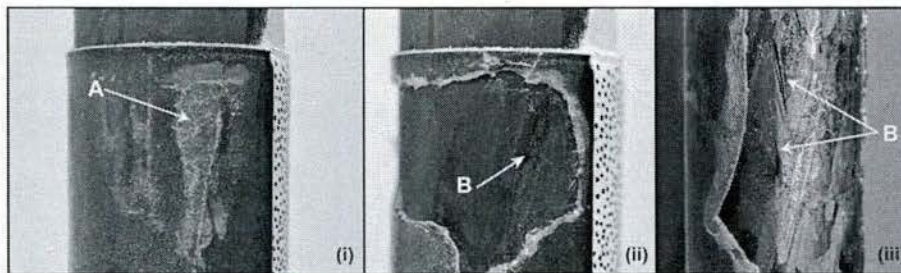


Figure 10: Post-mortem images of tubes with thick exterior coatings showing (A) coating delamination and (B) crimping in the outer ply with some cracking (coating has been peeled to expose composite surface).

Again, areas of delamination of the PU coating are seen where cracks exist, however for the thick outer coatings the PU layer was never punctured at these sites (see A in Figure 10.i). Peeling back the outer layer, the state of damage is seen in the center and right-most images. Here, the main longitudinal crack is indicated by "B" in Figures 10.ii and 10.iii, and is seen to be much less severe than either of the previous cases. There is significantly less fiber fraying along the crack, and no separation of tube walls is seen. In fact, in some cases, the crack does not appear to penetrate completely through the thickness. Instead a slight bend is observed in the outer layer indicating the location of the crack. Thus, the thick outer coating provides an even greater suppressing effect on the damage mechanisms present in these structures. The suppressing effect causes less energy to be dissipated in the implosion event, and contributes to the increased energy released in the pressure pulse as previously discussed.

Conclusions

The hydrostatic implosion of composite tubes with polymeric coatings on the interior and exterior surfaces was studied to examine differences caused by the specific type of coating. High-speed photography, DIC measurements, and dynamic pressure sensors are used to characterize the effects of the thickness and location of the coating on the mechanics of collapse as well as local pressure fields, with the goal of mitigating the pressure pulse. The completion of this work has resulted in the following conclusions:

- The collapse of layered composite tubes was well characterized using measurements of local pressure in conjunction with optical displacement measurements.
- The flow energy, obtained directly as a function of pressure, is a useful tool for comparing the total energy emitted during the implosion process.

- Thin coatings have little effect on pressure pulses emitted following implosion, regardless of location of the coating.
- Thick exterior coatings increase the energy released following implosion due to suppression of the damage mechanisms that dominate failure.
- Thick interior coatings decrease the energy released from implosion due to a reduction in collapse velocity and a softening of wall-to-wall contact.
- Interior polyurea coatings are successful in mitigating implosion pressure pulses, whereas, exterior coatings amplify their strength.

Acknowledgements

The authors would like to acknowledge the Office of Naval Research and Dr. Yapa D.S. Rajapakse for providing financial support to conduct this research under Grant No. N00014-10-1-0662.

References

- [1] Turner SE. Underwater Implosion of Glass Spheres. *J Acoust Soc Am* 2007; 121: 844–852.
- [2] Turner SE, Ambrico JM. Underwater Implosion of Cylindrical Metal Tubes. *J Appl Mech* 2012; 80(1): 1-11
- [3] Urick RJ. Implosions as sources of underwater sound, *J Acoust Soc Am* 1963; 35, pp. 2026–2027. DOI: 10.1121/1.1918898
- [4] Orr M, Schoenberg M. Acoustic signatures from deep water implosions of spherical cavities, *J Acoust Soc Am* 1976; 59: 1155–1159.

[5] Harben PE, Boro C. Implosion Source Development and Diego Garcia Reflections. Presented at the 23rd Department of Defense/Department of Energy Seismic Research Review, Jackson Hole, WY, 2-5 October 2001.

[6] Accident grounds neutrino lab - physicsworld.com [WWW Document], n.d. URL <http://physicsworld.com/cws/article/news/2001/nov/15/accident-grounds-neutrino-lab> (accessed 2.10.14).

[7] Ling J, Bishai M, Diwan M, Dolph J, Kettell S, Sexton K, Sharma R, Simos N, Stewart J, Tanaka H, Viren B, Arnold D, Tabor P, Turner S, Benson T, Wahl D, Wendt C, Hahn A, Kaducak M, Mantsch P, Sundaram SK. Implosion chain reaction mitigation in underwater assemblies of photomultiplier tubes. Nucl Instrum Methods Phys Res Sect Accel Spectrometers Detect Assoc Equip 2013; 729: 491–499.

[8] Diwan M, Dolph J, Ling J, Sharma R, Sexton K, Simos N, Tanaka H, Arnold D, Tabor P, and Turner S. Underwater Implosions of Large Format Photo-multiplier Tubes. Physics Procedia 2012; 37: 715-21.

[9] Farhat C, Wang CG, Main A, Kyriakides S, L. Lee H, Ravi-Chandar K, Belytschko T. Dynamic Implosion of Underwater Cylindrical Shells: Experiments and Computations. Int J Solids Struct 2013; 50(19): 2943-961.

[10] Ikeda CM, Wilkerling J, Duncan JH. The Implosion of Cylindrical Shell Structures in a High-pressure Water Environment. Proc of the R Soc A: Math, Phys and Eng Sci 2013; 469: 2160

- [11] Moon CJ, In-Hoon K, Bae-Hyeon C, Jin-Hwe K, Choi JH. Buckling of Filament-wound Composite Tubes Subjected to Hydrostatic Pressure for Underwater Vehicle Applications. *Compos Struct* 2010; 92(9): 2241-251.
- [12] Ross CTF, Little APF, Haidar Y, Waheeb AA. Buckling of Carbon/Glass Composite Tubes Under Uniform External Hydrostatic Pressure. *Strain* 2009; 47: 156-174.
- [13] Smith PT, Ross CTF, Little APF. Collapse of Composite Tubes under Uniform External Hydrostatic Pressure. *J of Phys: Conference Series* 2009; 181: 156-157.
- [14] Hernández-Moreno H, Douchin B, Collombet F, Choqueuse D, Davies P. Influence of Winding Pattern on the Mechanical Behavior of Filament-wound Composite Tubes under External Pressure. *Compos Sci and Technol* 2008; 68(3-4): 1015-024.
- [15] Hur SH, Son HJ, Kweon JH, Choi JH. Postbuckling of Composite Tubes under External Hydrostatic Pressure. *Compos Struct* 2008; 86(1-3): 114-24.
- [16] Yang C, Pang SS, Zhao Y. Buckling Analysis of Thick-Walled Composite Pipe under External Pressure. *J Compos Mater* 1997; 31(4): 409-26.
- [17] Pinto M, Gupta S, Shukla, A. Study of Implosion of Carbon/Epoxy Composite Hollow Cylinders Using 3-D Digital Image Correlation. *Compos Struct* 2014; 119: 272–286.
- [18] Pinto M, Gupta S, Shukla A. Hydrostatic Implosion of GFRP Composite Tubes Studied by Digital Image Correlation. *J of Press Vess Technol* 2015; 051302.
- [19] Pinto M, Shukla A. Shock-Initiated Buckling of Carbon/Epoxy Composite Tubes at Sub-Critical Pressures, *Exp Mech* 2015; 1-12, doi:10.1007/s11340-015-0033-1

- [20] Tekalur S, Shukla A and Shivakumar K. Blast resistance of polyurea based layered composite materials. *Compos Struct* 2008; 84: 271–281.
- [21] Bahei-El-Din YA, Dvorak GJ and Fredricksen OJ. A blast-tolerant sandwich plate design with a polyurea interlayer. *Int J Solid Struct* 2006; 43: 7644–7658.
- [22] Gardner N, Wang E, Kumar P, et al. Blast mitigation in a sandwich composite using graded core and polyurea interlayer. *Exp Mech* 2012; 52: 119–133.
- [23] Sutton MA, Orteu JJ, Schreier HW. *Image Correlation for Shape, Motion and Deformation Measurements: Basic Concepts, Theory and Applications*. New York, NY: Springer, 2009.
- [24] Gupta S, Parameswaran V, Sutton MA, Shukla A. A study of Underwater Implosion using Digital Image Correlation, *Proc of the R Soc A* 2014; 470(2172): 20140576.
- [25] Cole RH. *Underwater Explosions*. Princeton: Princeton Univ., 1948.
- [26] Arons A, Yennie D. Energy Partition in Underwater Explosion Phenomena. *Rev of Mode Phys* 1948; 20(3): 519-36.
- [27] Plesset, Milton S. *Bubble Dynamics*. N.p.: California Institute of Technology, Engineering Division, 1963.

Chapter 6 : Shock-Initiated Buckling of Carbon/Epoxy Composite Tubes at Sub-Critical Pressures

by

Michael Pinto and Arun Shukla

has been published in Experimental Mechanics

Corresponding Author: Arun Shukla

Dynamic Photo Mechanics Laboratory

Department of Mechanical, Industrial and Systems Engineering

University of Rhode Island

206 Wales Hall, 92 Upper College Rd Kingston, RI, 02881,

USA Phone: +1-401-874-2283

Email Address: shuklaa@uri.edu

ABSTRACT

A comprehensive investigation on the implosion of composite cylinders subjected to a nearby explosion is performed. Experiments are conducted in a large pressure vessel, designed to provide constant hydrostatic pressure throughout the event. Carbon fiber/epoxy filament-wound tubes are studied with constant hydrostatic pressure and varying charge standoff distances to determine the effect of the explosive loading on the mechanisms of collapse. 3-D Digital Image Correlation (DIC) is used to capture the full-field displacements and velocities during the implosion event, and to characterize the initial dynamic response of the tube. Dynamic pressure transducers measure the shock waves generated by the explosive and also the pressure pulse generated by the collapse. Results show that different magnitudes of explosive loading produce drastic differences in the way implosions are initiated, and in the extent of damage to the structure. Experiments with strong explosive loading show immediate collapse of the tube upon the arrival of shock wave. Relatively smaller explosive loading result in collapses due to the additional bubble pulse loading, or after accumulating damage for extended periods of time.

Introduction

In recent decades, there has been increased interest in using composites for naval and marine applications. As compared to metals, composite materials have reduced weight, improved corrosion resistance, and greater operating depths for submerged environments. However, widespread adaptation of composite materials is hindered by a lack of complete understanding and simple design rules, especially for extreme loading conditions [1]. One such condition in undersea applications is that of implosion. Implosion is the rapid collapse of a sealed, thin-walled structure subjected to external pressure. When the applied external pressure reaches a critical value, the structure becomes unstable and its walls buckle inward, causing the tube to collapse completely. An implosion caused by quasi-static pressurization to this critical pressure is known as a natural implosion. However, implosions can also be initiated at sub-critical pressures with an underwater explosive (UNDEX) loading. If a structure experiences a high magnitude shock – wave loading such as that generated by a near-field UNDEX, it may collapse at a relatively low hydrostatic pressure [2]. This work focuses on addressing this extreme condition for composite materials.

Some experimental work has been performed on the implosion of composite tubes, however these studies are limited to hydrostatic implosion and typically concerned only with evaluating collapse pressure [3-6]. Most recently, the hydrostatic implosion of carbon fiber and glass fiber reinforced tubes was studied experimentally by the authors using Digital Image Correlation to relate collapse mechanics to the changes in local pressure fields [7,8]. Some numerical studies have been performed on implosions initiated by explosive loading in recent years. Pegg studied the mechanics of explosive initiated implosions of homogenous materials and how the qualities of the impulse affect the instability [9]. Tanov et. al examined the effect of static preloading on

the impulse driven implosion of composite tubes using finite elements [10]. Krueger also used finite element models to study explosive initiated implosion of metallic tubes with varying impulse strengths [11]. Fatt et. al developed stability diagrams for composite cylinders under shock loading using Mathieu equations [12]. A few experimental studies also exist on the response of closed cylinders to underwater explosions. Both Brett and Yiannakopolous [13] and Hung et. al [14] independently evaluated the dynamic response of metallic cylinders subjected to a nearby explosive. In addition, Ikeda performed experiments on the explosive initiated implosion of metallic tubes with varying loading, to define the conditions for a collapse to occur [15]. Finally, Arora et. al performed experiments on the effects of air and underwater blast loading on composite panels and tube structures [16]. However, no experimental work exists on explosive initiated implosions of composite materials, and what numerical work does exist does not account for material damage.

This study looks to address this gap in understanding by using high-speed photography coupled with Digital Image Correlation to explore the implosion of composite tubes subjected to shock waves of different strengths. Experiments also focus on the interaction of the bubble pulse with the structure, and its effect on the implosion process. Depending on the stand-off distance of the charge, the tube may implode due to different features of the explosive pressure history. This will also change the degree of damage incurred in the structure, as well as the effect of the collapse on the local pressure field.

Experimental Details

The impodable volumes in this study are carbon/epoxy filament wound composite tubes, consisting of seven layers of unidirectional carbon fabric reinforcement arranged in a $[\pm 15/0/\pm 45/\pm 15]$ layup with a 60.3mm inner diameter and 381mm unsupported length. These

cylinders are manufactured by Rock West Composites (West Jordan, UT) with a nominal wall thickness of 1.63mm. The dimensions are selected as to provide specimens with a relatively low expected collapse pressure, and a high radius-to-thickness ratio so that thin-wall assumptions may be utilized.

The explosives used are RP-85 exploding-bridgewire (EBW) detonators manufactured by Teledyne RISI, Inc. (Tracy, CA). The output explosive material in these detonators is 1031mg of RDX (cyclotrimethylenetrinitramine), initiated by 80mg of PETN (pentaerythritol tetranitrate), the combination of which is equivalent to 1778mg of TNT.

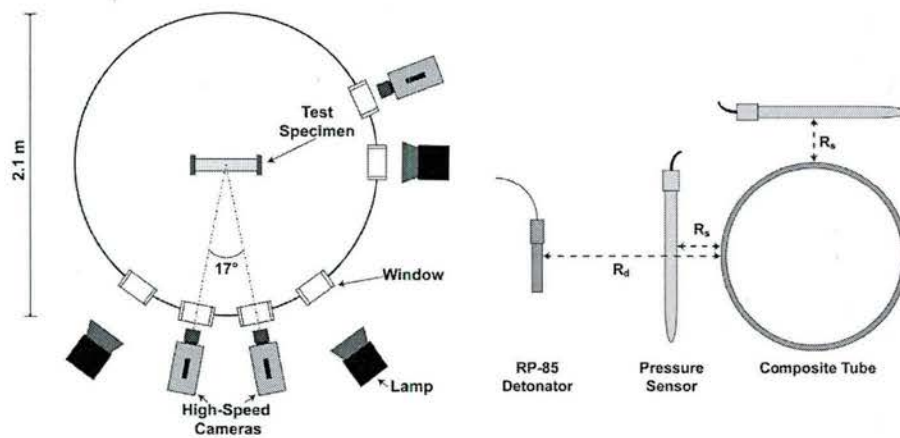


Figure 1: Diagram of experimental setup (left) and image of charge and sensor positioning (right), with the standoff distances of the detonator (R_d) and the sensor (R_s) clearly defined

All experiments are conducted in a 2.1m diameter spherical pressure vessel, able to provide constant hydrostatic pressure throughout the collapse event (see Figure 1). Several acrylic windows mounted about the midspan of the pressure vessel allow the specimens to be viewed by cameras and adequately lit by two high intensity light sources.

The specimen is sealed using two aluminum end caps then suspended horizontally in the center of the pressure vessel using steel cables secured to the inner walls of the vessel. To measure the incident shock wave loading and the changes in local pressure during the collapse event, high pressure blast transducers (PCB 138A05, PCB Piezotronics, Inc., Depew, NY) are mounted at different locations about the specimen. Two sensors are located at the midspan of the specimen, and four sensors are located at axial offsets of 127mm from the midspan. All sensors are mounted such that the distance between the sensing element and the outer surface of the tube is nominally 55mm. The amplified outputs of these sensors are recorded at a sampling rate of 2 MHz. The explosive charge is secured directly behind the specimen at a given standoff distance so as not to interfere with photography, and is aligned with the center of the implodable volume (see Figure 1).

The vessel is then flooded with filtered water, leaving a small air pocket. Once the vessel is filled, nitrogen gas is introduced into the air pocket to pressurize the enclosed water to the desired hydrostatic pressure. The pressure is increased slowly at a rate of 0.083 MPa/min to the chosen value. For this study, all experiments used a hydrostatic pre-pressure of 80% of the critical collapse pressure of the specimen. Following pressurization, the explosive is detonated using a high voltage firing unit which simultaneously triggers all data acquisition systems to record the event.

Prior to experiments, a random, high-contrast speckle pattern is applied by hand to a region spanning the entire length of the specimen and approximately half of the circumference using flat black and white paint. Features of the pattern were made sufficiently large as to occupy at least 3x3 pixels in the recorded images for optimal DIC measurements. Two high-speed cameras (Photron SA1, Photron USA, Inc.) positioned at a stereo angle of 17°, are used to capture images

of the patterned region of the specimen at a frame rate of 75,000 frames/second. The stereo images are analyzed using a commercially available DIC software, VIC3D 2012 (Correlated Solutions, Inc., Columbia, SC) to measure full-field displacements across the viewable surface of the specimen. 3-D Digital image correlation (DIC) is a well known non-contact optical technique to determine real-time, full-field displacements across the viewable surface of a specimen [17]. This technique is calibrated for underwater experiments based on previous work [18] for confidence in the accuracy of measured displacements and velocities. Using the referenced calibration method, in-plane and out-of-plane displacements may be determined within 1.2% and 2.5% error, respectively. A third high speed camera is used to observe the charge itself to track the growth and collapse of the gas bubble, and is set to record at 40,000 fps.

Results

Natural Implosion Experiments

Prior to explosive initiated series, several natural implosion experiments are performed on the tubes to be studied to determine the critical collapse pressure and to characterize the collapse and local pressure field in the case of a natural implosion. These experiments are performed in the same manner as recently published work by this group [7,8]. The critical collapse pressure of these tubes was found to be 0.90MPa. The pressure profile is plotted in Figure 2, along with the displacement and velocity of the center point of the tube. High-speed photographs of the tube at different times during the collapse are included in Figure 3. In these plots, $t = 0\text{ms}$ represents the instant that opposing walls of the tube make contact with each other.

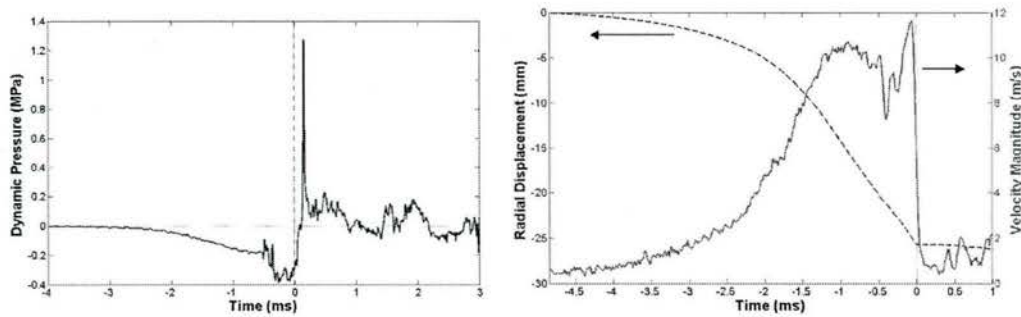


Figure 2: For a natural implosion, pressure history about the midspan of the specimen (left) and radial displacement and velocity curves measured at the center of the specimen (right)

It can be seen that the implosion of these tubes is quite similar to that of metallic tubes [19,20] as well as other composite tubes studied by this group [7,8]. Starting at $t = -4.7\text{ms}$, the walls of the tube begin to accelerate inward as observed in the displacement and velocity traces. As the walls accelerate, the local pressure decays to a minimum just prior to $t = 0\text{ms}$. At $t = 0\text{ms}$, opposing walls contact each other, resulting in the rapid deceleration of the walls. This imposes a large change in momentum onto the surrounding fluid, resulting in the high magnitude ($\sim 1.30\text{MPa}$) pressure pulse seen shortly thereafter. Following wall contact, the buckle propagates axially through the length of the tube until the entire tube is flattened. From the high-speed images in Figure 3, it is seen that the tube remains free of visible damage until just before the time of wall contact. At $t = -0.013\text{ms}$, extreme bending at the two lobes of the buckling shape cause through-thickness cracking parallel to the length axis of the tube. Post-mortem analysis shows that damage is mainly restricted to these two longitudinal cracks, which propagate through nearly the entire length of the specimen.

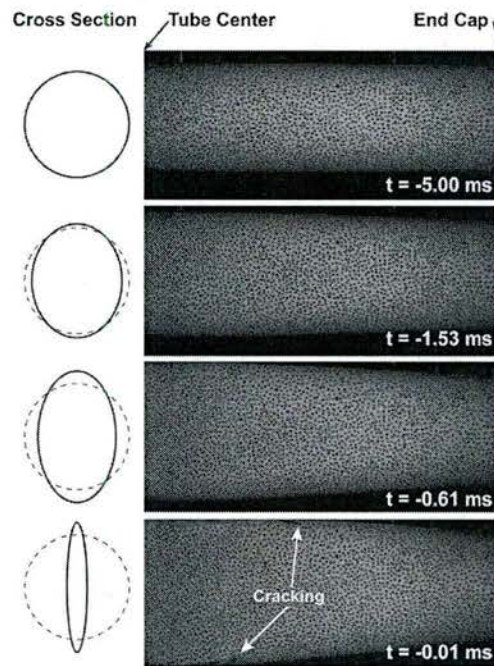


Figure 3: High-speed images taken at various times during the natural implosion experiments. Illustrations of the tube cross-section are to the left of the respective image. The tube is seen to buckle without visible damage until 0.013ms prior to wall contact

The experiments described above were used to design the explosive initiated implosion series, which is summarized in Table 1. For all experiments in this series, the hydrostatic pre-pressure is kept constant at 80% of the critical collapse pressure, or 0.71MPa. Three different explosive standoff distances are used, 102mm, 203mm, and 305mm. These standoffs are chosen to impart different magnitude shock waves to the specimens while not allowing the gas bubble to interact with the tube. At least 2 experiments are performed for each case, to demonstrate repeatability of results. For each case, the tube did implode, but the time at which the implosion initiated after the explosion is different for each standoff distance. This implies that for different standoff

distances, different features of the explosive pressure history trigger the collapse, and therefore the mechanics at play in each case is unique.

Interaction of Shock Wave with Specimen

One important thing to understand when studying the problem of an explosive initiated implosion is how the pressure wave interacts with the specimen. It is well known that the initial shock wave released from an UNDEX may be treated as an acoustic pressure pulse that travels at roughly sound speed once fully developed [21]. This allows the use of acoustic theory in analyzing the behavior of the wave. As an example, the pressure recorded at two different locations about the midspan of the tube for the case of a 305mm explosive standoff is plotted in Figure 4. Comparing pressure histories recorded at a sensor between the charge and the specimen (Sensor 1 in Figure 4) and at a sensor above the specimen (Sensor 2 in Figure 4), an interesting phenomenon is observed. In all experiments, it is seen that sensors located between the charge and the specimen record the initial high magnitude shock followed by a negative pressure spike of appreciable magnitude less than 0.1ms later. In contrast, sensors located above the tube record only the initial pulse, followed by a smaller pressure "tail" that is typical of shock waves.

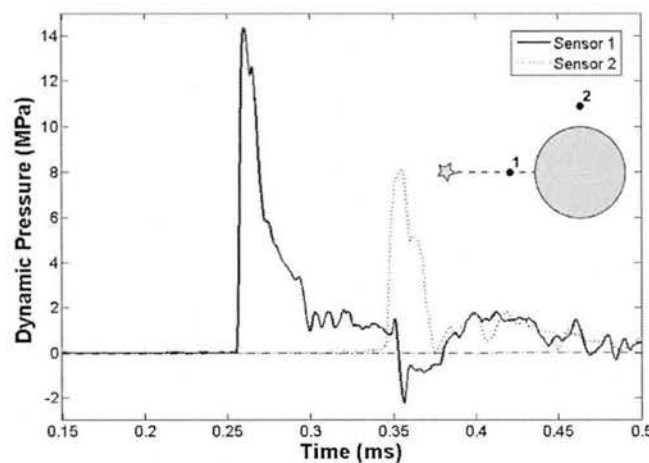


Figure 4: Initial shock wave measured at locations between the charge and specimen and directly above the specimen for the case of a 305mm explosive standoff. The star in the image represents the location of the charge.

Because the delay between the initial spike and the negative pulse is slightly greater than the acoustic travel time for twice the distance from the sensor to the specimen (2x70mm), the interface between the fluid and the specimen was further studied. When an acoustic wave encounters a boundary between two different materials, part of the wave will be transmitted into the second material while part will be reflected back into the first material. The reflected and transmitted pressures, P_r and P_t respectively, caused by an incident wave with pressure P_i are defined as:

$$P_r = R * P_i \quad P_t = (1 + R) * P_i \quad (\text{Eq.1})$$

Where R is known as the reflection coefficient. The reflection coefficient for a normal incidence of a wave at a boundary is defined as [22]:

$$R = \frac{\rho_2 c_2 - \rho_1 c_1}{\rho_2 c_2 + \rho_1 c_1} \quad (\text{Eq.2})$$

Where ρ is the material density, c is the sound speed of the material, and subscripts 1 and 2 refer to the material before and after the boundary, respectively. The density and sound speed for the water in this experiment are 998 kg/m³ and 1488 m/s, respectively. The through-thickness density and sound speed for carbon/epoxy composites has been reported as 1611 kg/m³ and 3042 m/s, respectively. For an acoustic wave traveling from water to the composite tube with normal incidence, the reflection coefficient was calculated as 0.535. Simple acoustic theory can show [22], using Eq. 2, that upon encountering the surface of the tube, an incident wave with

magnitude p_i creates a reflected wave with a magnitude $0.535p_i$, and a transmitted wave with a magnitude of $1.535p_i$ maintaining the same compressive sign. The transmitted wave travels through the composite tube until it reaches the enclosed air volume. The reflection coefficient at this interface is approximately -1 . This means that upon encountering this interface, all of the wave is reflected back into the composite wall with the same magnitude, but with opposite sign. This converts the pulse into a tensile wave which then travels back through the tube wall and into the surrounding fluid where it is observed by nearby sensors. Accounting for the reflection constant again at the composite-water interface calculated using Eq. 2, the magnitude of the tensile wave transmitted to the water is $0.821p_i$. This, coupled with attenuation in the various media, explains the reduced magnitude of the reflected tensile pulse observed in the pressure trace for sensors directly between the charge and the tube.

The important conclusion drawn from this analysis is that when a sealed composite tube is subjected to explosive loading, the pressure waves that travel through the walls of the structure are not solely compressive. If this tube is filled with a low impedance material such as air, tensile waves of significant magnitude will be caused in the tube wall by the impedance mismatch at the interior interface. This tensile loading has the potential to degrade the stability of the structure, as it may cause damage in the matrix material or at the fiber-matrix interface which are highly sensitive to out-of-plane tension [23].

Identifying Features of the Pressure History

By its nature, the pressure fields generated in an underwater explosion in a closed tank are very noisy. Reflections from the initial shock wave and the "bubble pulse" are important features to identify, but superposition of these features can make that a challenge. To address this, acoustic

wave theory coupled with an additional high-speed camera observing the explosive itself are used to distinguish these events.

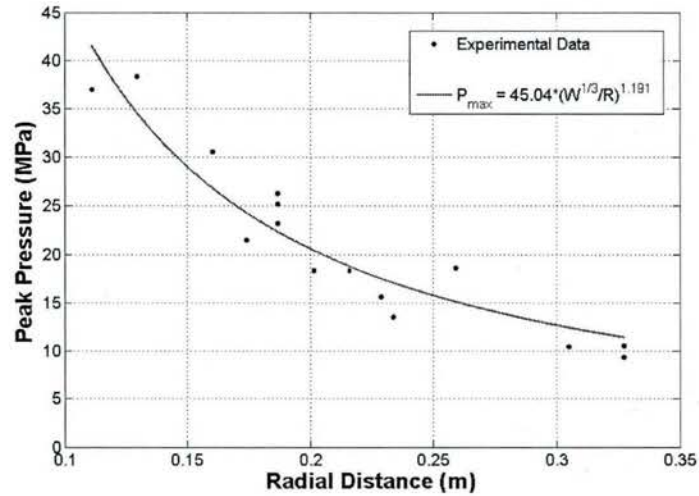


Figure 5: Peak pressure of RP-85 as a function of standoff distance. The parameters for the fit curve are given in the plot for a charge of mass, W , in kilograms

The initial shock wave produced by the RP-85 detonator is characterized by recording peak pressures at several different standoff locations. The model proposed by Shin [24] is then fit to the data, to obtain a relationship by which the peak pressure could be predicted as a function of standoff distance. Experiments were conducted with just the explosive in the pressure vessel to characterize the loading pulse. The fit model is included in Figure 5, and this was used to determine maximum incident pressures listed in Table 1.

Case	Hydrostatic Pressure (MPa)	Explosive Standoff (mm)	Maximum Predicted Incident Pressure (MPa)	Time before Implosion (ms)
1	0.71	102	45.9	0.93
2	0.71	203	20.2	6.83

3	0.71	305	12.4	15.22
---	------	-----	------	-------

Table 1: Summary of explosive-initiated implosion experiments

Reflections of the initial shock are determined by assuming that pulse travels with acoustic wave speed, which in water is approximately 1500 m/s. At this velocity, the shock will travel to the tank boundaries and back to the sensors after 1.04-1.80ms depending on the location of the charge. Using the same travel speed, a second reflection of that wave will arrive after 2.10-3.61ms. Attenuation of the wave during travel will cause the reflections to be significantly lower magnitude and less sharp, and because the charge is not in the absolute center of the tank, the reflected wave will be recorded as a tight group of small peaks. For these reasons, the first and second reflections of the initial shock are identified as clusters of smaller spikes in the pressure located in the aforementioned time windows.

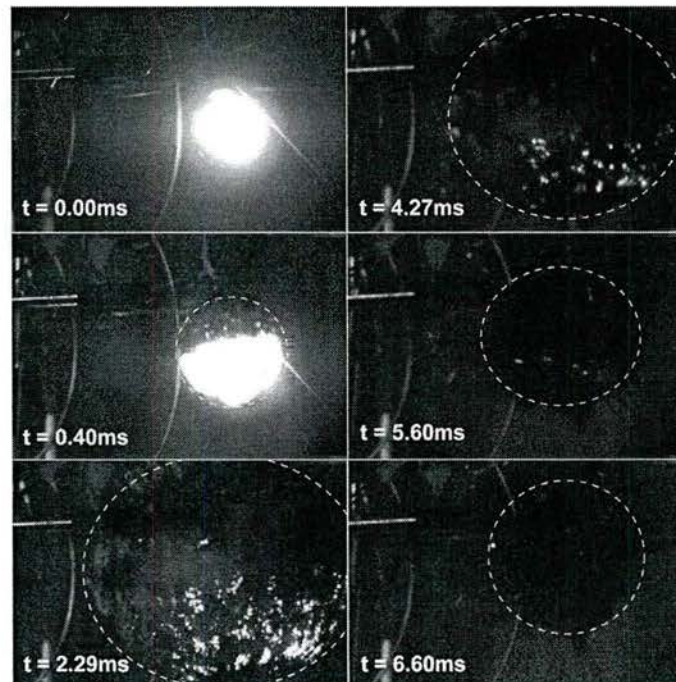


Figure 6: High-speed images of the growth and collapse of the gas bubble, the boundary of which is indicated by a dashed white line. Here the bubble reached maximum size at 2.29ms after detonation and collapsed at 5.60ms

The additional high-speed camera is used to identify the bubble pulse. When an underwater explosive is detonated, the decomposed gases of the charge create an expanding superheated gas bubble. After reaching its maximum critical size, the surrounding hydrostatic pressure of water causes the bubble to collapse, and upon completion of this collapse, a relatively strong and fairly broad pressure pulse known as the "bubble pulse" is emitted [21]. The magnitude of the bubble pulse is typically much smaller than that of the initial shock wave, however due to its long duration, the impulse is of comparable strength. To identify the timing of this pulse, a typical growth of the bubble to its maximum size and subsequent collapse is shown in Figure 6. In all cases, the bubble grows to its maximum size at approximately 2.29ms and collapses between 5.00ms and 5.60ms, so a broad pressure pulse found near this region in time is considered to be the bubble pulse.

Near-Field Explosion (102mm Standoff)

The pressure history at the point on the specimen nearest to the charge for the 102mm standoff is plotted in Figure 7, where the charge detonates at 0.00ms (this time notation will be used throughout later in this article). In this case, the tube implodes shortly after experiencing the initial shock from the explosive. The initiation of the instability occurs at approximately 0.90ms, well before the arrival of reflections from the tank wall, so it may be concluded that the initial shock wave alone possesses sufficient energy to trigger the collapse at this sub-critical static pressure. Wall contact occurs 5.00ms after the initiation of the implosion, roughly consistent with results from natural implosion experiments. This implies that though the initiation

mechanism of the collapse is different, the subsequent mechanics of the collapse are the same as for a natural implosion. In this case, no implosion pulse is detectable in the pressure history following wall contact. This is due to the noisy nature of the pressure signal at this time caused by the superposition of reflections of the initial shock and bubble pulses from the tank walls.

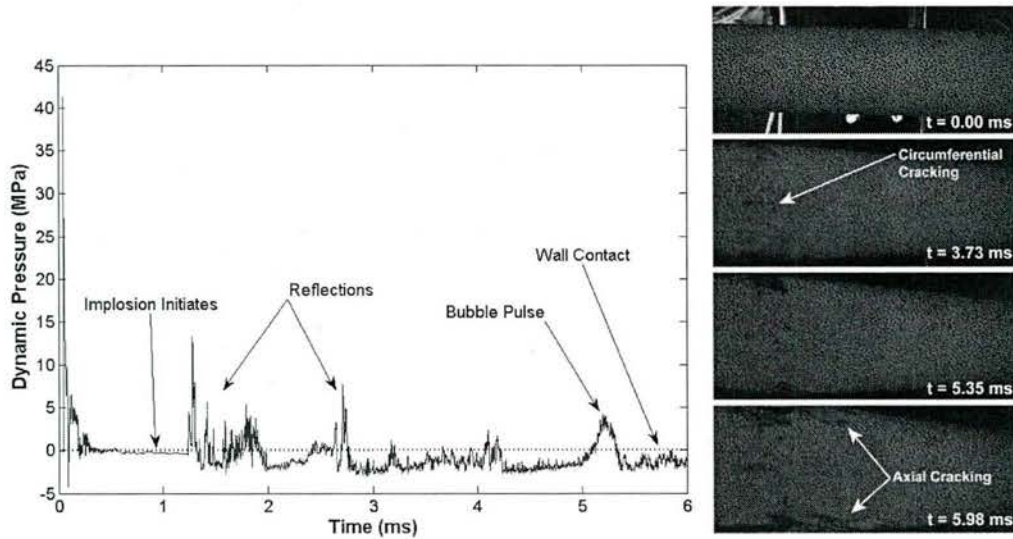


Figure 7: Pressure history (left) and high-speed images (right) for explosive experiments with 102mm standoff

Though the time to collapse is consistent with the natural implosion, a unique feature of this case is the initiation of observable damage prior to wall contact. The high-speed images in Figure 7 show that a large degree of circumferential cracking occurs 2.21ms prior to wall-contact, located at the midspan of the tube. These cracks are seen in post-mortem images (Figure 8) to run parallel to reinforcing fibers, implying that they occur in the resin-rich regions between fibers. The center of the tube experiences the most severe loading, as it is the closest to the charge. The cause for this early damage is the particular wave interaction discussed in Section 3.2. The resulting tensile loading within the tube wall is enough to cause inter-fibrillar as well as matrix

cracking, as seen in the high-speed images. This cracking significantly degrades the structural stability, and is a contributing factor in the damage initiation eventually leading to the implosion.

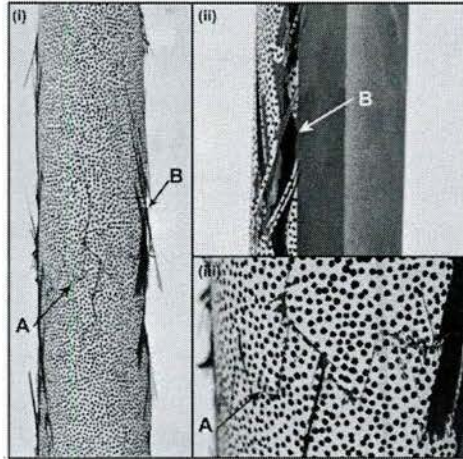


Figure 8: Post-mortem images showing the full-length (i), a side-view (ii), and a zoomed image of the tube center for 102mm explosive standoff. These images display circumferential cracking (A) and dramatic, through-thickness axial cracking (B)

Post-mortem images in Figure 8 show very extensive damage to the tubes, mainly in the form of through-thickness axial cracks (B) and circumferential cracks (A) localized about the midspan of the tube. The axial cracks in these tubes completely separate sections of the tube, and several frayed and pulled-out fibers are seen on the faces of the cracks. This shows that these cracks form in a very high energy event, enough to fracture both matrix and fiber in all seven plies and cause the pull-out of adjacent fibers. The axial cracking for this case is more extensive than all other cases, including that of natural implosion. Pegg [9] demonstrated that hydrostatic pressure combined with strong impulse loads result in more severe deformations, which is the reason for the extent of damage. In comparison, the circumferential cracks at the midspan are much less

severe. These cracks do not penetrate completely through the tube wall, do not travel very far from the tube midspan, and cause no fiber pull-out.

Mid-Field Explosion (203mm Standoff)

The pressure history at the point on the specimen nearest to the charge for the 203mm standoff is plotted in Figure 9. Implosion again occurs in this case, though it is much later in the time than the 102mm standoff case, initiating 6.53ms after the detonation of the charge.

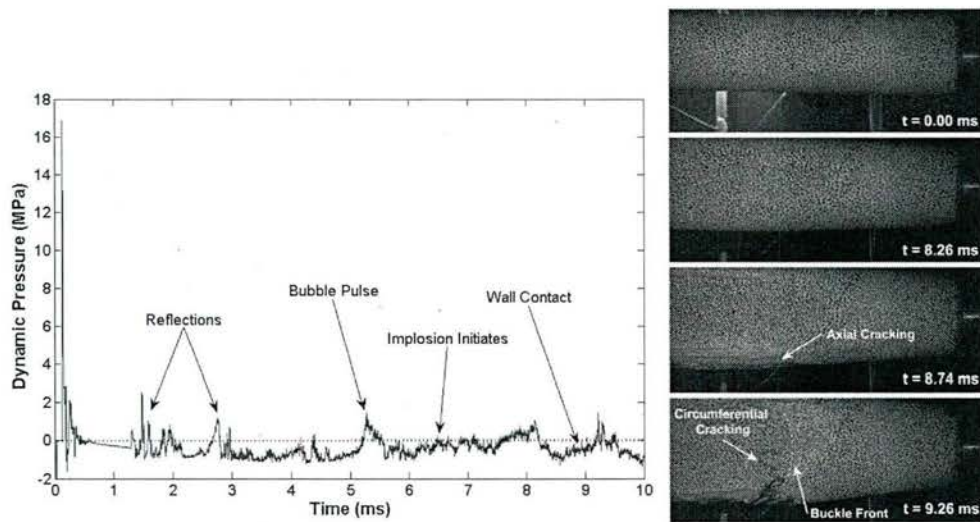


Figure 9: Pressure history (left) and high-speed images (right) for explosive experiments with 203mm standoff

This delayed collapse shows that neither the initial shock wave nor the reflections of that shock from the tank walls are sufficient to cause the collapse at this charge distance. The instability is triggered after the first bubble pulse showing that for this standoff distance, the bubble pulse is the cause of the implosion. The tube continues to collapse until wall contact is made 2.43ms after initiation, which is significantly shorter than the collapse time of the natural implosion (4.7ms). The reason behind this reduction in collapse time, as well as the reason for the timing of the

collapse, is related to the wave interaction discussed in Section 3.2. Each feature of the pressure trace that encounters the specimen - the initial shock, reflections, and the bubble pulse - results in tensile loading within the tube wall. Unlike the previous case, the loading is not severe enough to exceed the tensile strength of the matrix. Examining high-speed images in Figure 9, no visible cracking occurs from the impact of the shock or the subsequent reflections and bubble pulse. However, damage may still occur within the material. This repeated loading can degrade the fiber/matrix interface, cause and/or propagate delaminations, and grow any pre-existing defects where stress concentrations may occur. The net result is that at each loading event, damage will accumulate in the material, which will reduce its stiffness and structural integrity. In this case, damage accumulates enough in the first 5.00ms of the pressure history that the energy supplied by the bubble pulse is sufficient to initiate the instability. As is the case with 102 mm standoff distance, the implosion pulse is not reliably distinguished for these experiments due to the noisy nature of the pressure field at the time which it occurs.

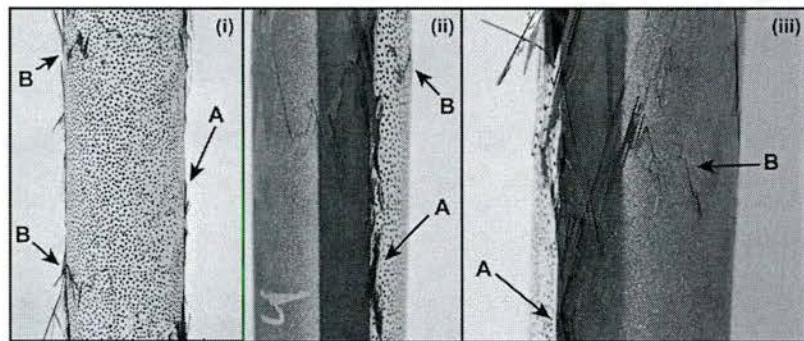


Figure 10: Post-mortem images of the front (i) and side faces (ii & iii) for 203mm explosive standoff, showing axial cracking (A) and multiple instances of circumferential cracking (B)

Post-mortem images (Figure 10) again show large amounts of damage, including through-thickness axial cracks (A) and circumferential cracks (B) offset from the midspan. Though the

axial cracks do penetrate completely through the thickness of the tube wall, they are significantly less severe than for the previous case. Fiber pull-out is observed in the vicinity of these cracks, however there is no separation of the tube walls, and the structure maintains a large portion of its integrity. The circumferential cracks appear similar to those seen in the previous case, however their location and cause are quite different. These cracks are seen to appear only after wall contact has made and the flattening of the tube has propagated past the point where the cracks emerge. This shows that these cracks are not a result of the incident shock, but rather due to the large deformations resulting from the buckle propagation.

Far-Field Explosion (305mm Standoff)

The pressure history at the point on the specimen nearest to the charge for the 305mm standoff is plotted in Figure 11. Similar to the previous two cases, these tubes implode in a mode 2 shape, however they collapse very late in the event, initiating 15.26ms after the detonation of the charge. This is long after both the initial shock and the first bubble pulse, showing that neither of these events trigger the collapse on their own. Wall contact occurs at 1.83ms following the initiation of the implosion, even shorter than for the 203mm standoff case. Like the 203 mm standoff case, the cause for the delayed collapse as well as the duration of the collapse is due to the accumulation of damage caused by each successive loading event in the pressure history. This damage continually degrades the structural stiffness, until the vibrations caused by the impulse coupled with hydrostatic pressure can drive the implosion. The development of visible damage as seen in the high-speed images is less severe than for this case as no circumferential cracking appears at any time.

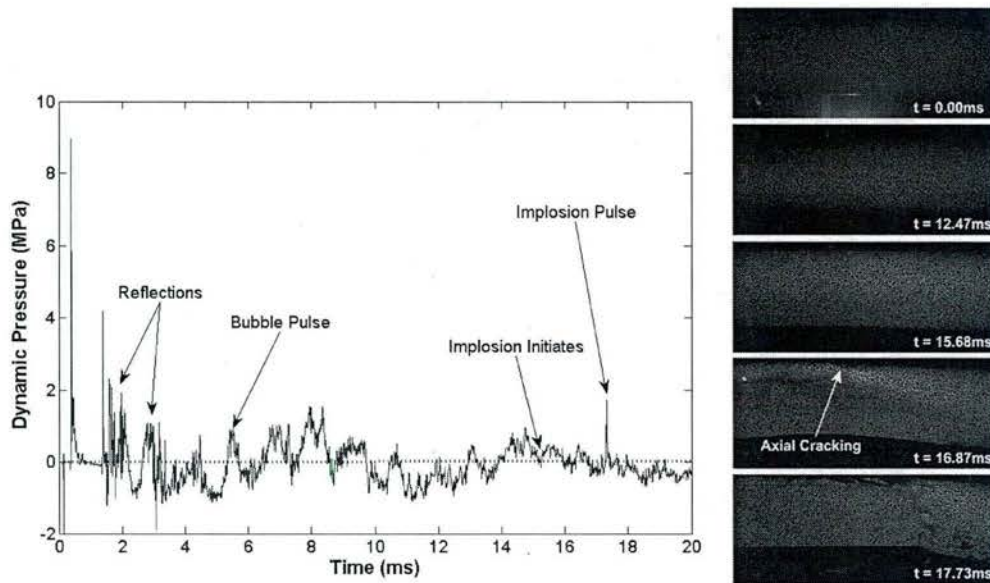


Figure 11: Pressure history (left) and high-speed images (right) for explosive experiments with 305mm standoff

In this case, the pressure field has settled enough that an implosion pulse is clearly distinguished. Wall contact occurs at 17.09ms, and 0.21ms later a sharp high magnitude pressure spike is recorded with strength of 1.67MPa. The magnitude and timing of this pulse is consistent with that seen in natural implosion experiments, giving additional evidence that this is in fact an implosion pulse.

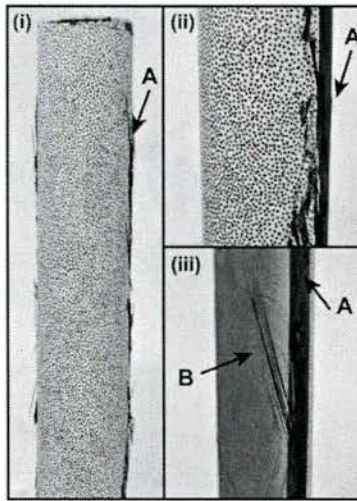


Figure 12: Post-mortem images of the front (i), side (ii), and back (iii) faces for 305mm explosive standoff, showing axial cracking (A) and adjacent outer ply cracks (B)

Post-mortem images of these specimens (Figure 12) show the least damage of all cases, mainly in the form of through-thickness axial cracks (A). Referring back to the high-speed images in Figure 11, these cracks appear shortly before wall contact is made, implying that they are a result of extreme bending strains at that time. Some fiber pull-out is seen near these cracks as well as interfibrillar cracking in the outer ply, parallel to the 15° fiber angle of that layer (B). The net damage in the structure is still far less extensive than that found in the previous two cases, due to the greatly reduced intensity of the incident shock (see Table 1).

DIC Analysis of Initial Shock Response

From previous work, it is known that prior to a dynamic collapse, hollow cylinders experience some degree of quasi-static ovaling due to hydrostatic pressure [7,8,18]. For a natural implosion, a maximum pre-buckling radial deformation of -1.57mm is measured prior to the dynamic collapse. At 80% of the critical collapse pressure, the pre-buckling reaches only -

0.56mm, showing that a significant perturbation of more than 1mm is required to reach a region of instability.

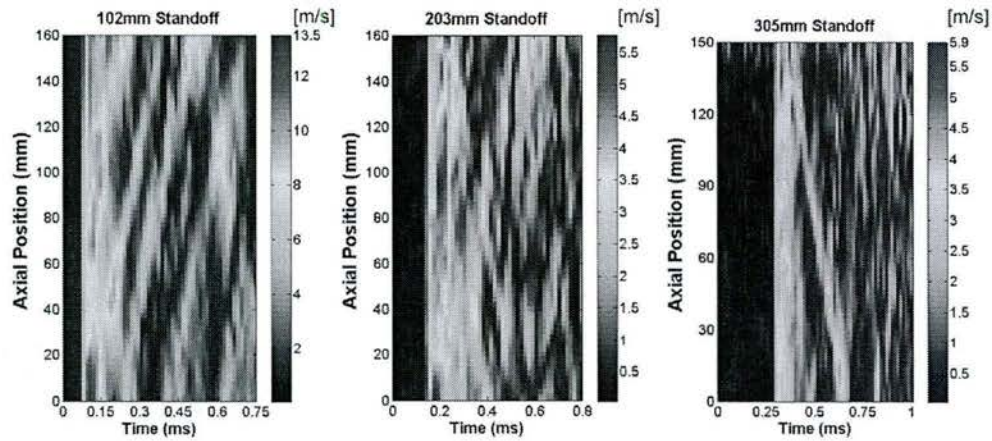
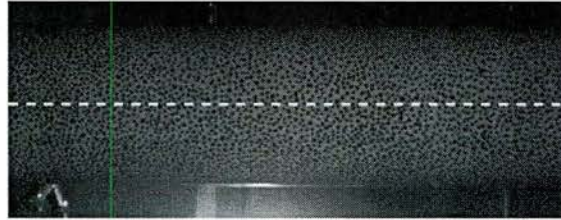


Figure 13: Velocity contours for half of the length of each specimen after impact of the initial shock. The top image indicated the location of DIC data extraction with a dashed white line. The zero point on the y-axis indicates the center of the tube, and color represents velocity magnitude in meters/second

DIC is also used to compare the initial response of the tube to the shock loading. Figure 13 shows contours of velocity magnitude across half of the length of the tube over time. The first observation that can be made is the uniformity of loading across the length of the structure. At the close standoff, the initial response of the structure is very localized near the center of the tube. For higher standoffs, the response is more uniform across the length of the specimen. As

standoff distance is increased, the front of the pressure wave becomes increasingly planar due to geometric spreading, and will load a greater area upon initial impact. The magnitudes of the initial velocities are also quite different. For the 102mm, 203mm, and 305mm standoffs, tubes show a maximum initial velocity of 13m/s, 5.7m/s, and 4.5 m/s, respectively. This reduction is expected, since the peak pressure of the initial shock wave will decay as $\frac{1}{R_e}$, where R_e is the distance from the explosive. The difference in uniformity of the loading across the length of the tube, coupled with the difference in peak velocity greatly affects the dynamic response of the structure.

More important in this Figure is the visible difference in modal response of the structure to each loading case. For the farthest standoff distance, the tube appears to vibrate with a single axial lobe. After the initial impact of the shock, a single region of elevated velocity is seen to travel along the length, implying a single lobe of deformation. For the closest standoff, the response following the arrival of the shock is quite different. Here, multiple regions of high velocity are seen propagating axially along the tube at the same instant. This implies that at closest standoff, the initial localized shock wave excites higher-order axial modes in the structure, which is why the wave is able to initiate the instability. In the absence of damage, impulse-initiated buckling occurs due to the vibrations of the structure due to the applied shock [2]. The closest standoff excites higher-order vibrations with relatively high velocities, which provides a sufficient perturbation to trigger the collapse. In addition, previous research has shown that short pulse durations characteristic of explosive loads necessitate very high peak pressures to initiate an implosion [2]. For these reasons, neither of the larger standoffs are capable of causing a collapse from the initial shock alone, but rely on subsequent growth of damage.

Conclusions

The explosive-initiated implosion of carbon/epoxy composite tubes is studied for varying incident shock wave strengths. High-speed photography, DIC measurements, and dynamic pressure sensors are used to characterize the mechanisms of collapse for each case studied. The completion of this study has resulted in the following conclusions:

- A composite tube may implode at pressures 20% below the critical static pressure if it experiences impulsive loading from a nearby explosive.
- Explosive initiated implosions of composite tubes may occur due to: (i) the initial shock, (ii) the bubble pulse, or (iii) long after both of these features due to the accumulation of damage.
- The failure of composite tubes under these shock wave loading is fundamentally different from homogenous materials. It is largely governed by the damage created within the material due to high magnitude tensile waves reflected from the inner solid/air boundary.
- The implosion pulse generated from the collapse of the tubes is typically obscured in the pressure history, however in the case of a long delayed collapse, this pulse may be distinguished and is consistent with that generated in a natural implosion.
- The DIC technique can be used to extract the initial vibration response of the structure following loading, and shows that higher order modes are excited for closer standoff distances leading to the dynamic collapse.

Acknowledgements

The authors would like to acknowledge the Office of Naval Research and Dr. Yapa D.S. Rajapakse for providing financial support to conduct this research under Grant No. N00014-10-1-0662.

References

- [1] Mouritz AP, Gellert E, Burchill P, Challis K. Review of Advanced Composite Structures for Naval Ships and Submarines. *Compos Struct* 2001; 53(1): 21-42.
- [2] Lindberg HE, Florence AL. *Dynamic Pulse Buckling: Theory and Experiment*. Dordrecht: M. Nijhoff, 1987.
- [3] Moon CJ, In-Hoon K, Bae-Hyeon C, Jin-Hwe K, Choi JH. Buckling of Filament-wound Composite Tubes Subjected to Hydrostatic Pressure for Underwater Vehicle Applications. *Compos Struct* 2010; 92(9): 2241-251.
- [4] Ross CTF, Little APF, Haidar Y, Waheeb AA. Buckling of Carbon/Glass Composite Tubes Under Uniform External Hydrostatic Pressure. *Strain* 2009; 47: 156-174.
- [5] Smith PT, Ross CTF, Little APF. Collapse of Composite Tubes under Uniform External Hydrostatic Pressure. *J of Phys: Conference Series* 2009; 181: 156-157.
- [6] Hur SH, Son HJ, Kweon JH, Choi JH. Postbuckling of Composite Tubes under External Hydrostatic Pressure. *Compos Struct* 2008; 86(1-3): 114-24.
- [7] Pinto M, Gupta S, Shukla A. Study of Implosion of Carbon/Epoxy Composite Hollow Cylinders Using 3-D Digital Image Correlation. *Compos Struct* 2014; 119: 272-286.

- [8] Pinto M, Gupta S, Shukla A. Hydrostatic Implosion of GFRP Composite Tubes Studied by Digital Image Correlation. *J of Press Vess Technol* 2015:.
- [9] Pegg, NG. Effects of Impulse Duration and Combined Impulse-hydrostatic Pressure on Buckling Stability of Cylindrical Structures. *J of Ship Research* 38.2 (1994): 164-71.
- [10] Tanov R, Tabiei A, Simites G. Effect of Static Preloading on the Dynamic Buckling of Laminated Cylinders Under Sudden Pressure. *Mech of Advanced Materials and Struct* 6.3 (1999): 195-206.
- [11] Krueger, Seth R. Simulation of Cylinder Implosion Initiated by an Underwater Explosion. Monterey, CA: Naval Postgraduate School, 2006.
- [12] Hoo Fatt MS, Pothula SG. Dynamic Pulse Buckling of Composite Shells Subjected to External Blast. *Compos Struct* 2010; 92(7): 1716-727.
- [13] Brett J, Yiannakopoulos G. A Study of Explosive Effects in Close Proximity to a Submerged Cylinder. *International J of Impact Eng* 35.4 (2008): 206-25.
- [14] Hung CF, Lin BJ, Hwang-Fuu JJ, Hsu PY. Dynamic Response of Cylindrical Shell Structures Subjected to Underwater Explosion. *Ocean Eng* 36.8 (2009): 564-77.
- [15] Ikeda, Christine M. Fluid-structure Interactions Implosions of Shell Structures and Wave Impact on a Flat Plate. Thesis. University of Maryland, College Park, 2012.
- [16] Arora H, Hooper PA, Dear JP. The Effects of Air and Underwater Blast on Composite Sandwich Panels and Tubular Laminate Structures, *Experimental Mechanics* 2012; 52: 59-81, ISSN: 0014-4851

- [17] Sutton MA, Orteu JJ, Schreier HW. Image Correlation for Shape, Motion and Deformation Measurements: Basic Concepts, Theory and Applications. New York, NY: Springer, 2009.
- [18] Gupta S, Parameswaran V, Sutton MA, Shukla A. A study of Underwater Implosion using Digital Image Correlation, Proc of the R Soc A 2014; 470(2172): 20140576.
- [19] Turner SE, Ambrico JM. Underwater Implosion of Cylindrical Metal Tubes. J Appl Mech 2012; 80(1): 1-11.
- [20] Ikeda CM, Wilkerling J, Duncan JH. The Implosion of Cylindrical Shell Structures in a High-pressure Water Environment. Proc of the R Soc A: Math, Phys and Eng Sci 2013; 469: 2160
- [21] Cole RH. Underwater Explosions. Princeton: Princeton Univ., 1948.
- [22] Kinsler LE, Frey AR. Fundamentals of Acoustics. New York: Wiley, 1962.
- [23] Sridharan S. *Delamination Behaviour of Composites*. Cambridge, England: Woodhead, 2008.
- [24] Shin, Young S. "Ship Shock Modeling and Simulation for Far-field Underwater Explosion." Computers & Structures 82.23-26 (2004): 2211-219.

Chapter 7 : Dynamic Instabilities in Double Hull Composite Cylinders Under Hydrostatic Pressure

by

Nicholas DeNardo, Michael Pinto, and Arun Shukla

undergoing final revisions for publication

Corresponding Author: Arun Shukla

Dynamic Photo Mechanics Laboratory

Department of Mechanical, Industrial and Systems Engineering

University of Rhode Island

206 Wales Hall, 92 Upper College Rd Kingston, RI, 02881,

USA Phone: +1-401-874-2283

Email Address: shuklaa@uri.edu

ABSTRACT

The dynamic collapse of hollow and filled double hull composite cylinders is investigated experimentally. Carbon-fiber/epoxy double cylinders with and without parametrically-graded PVC foam cores in between are collapsed in a large-diameter pressure vessel, and dynamic pressure data is used in conjunction with underwater DIC to determine the effect of the double hull structure on implosion mechanics. Buckling initiation and overall collapse behavior of the specimen are studied, as well as the pressure pulse from the implosion released into the fluid. Incidents of the outer tube imploding but not the inner are reported, in addition to cases where both collapse. Results show heavier foam cores increase collapse pressure dramatically, and this increase in collapse pressure is predictively related to the mechanical and geometric properties of the foam cores themselves. Normalized dynamic pressure emitted from implosions is shown to occur in distinct phases, with an additional under- and overpressure region present if the inner tube collapses. When normalized for hydrostatic pressure, fluid impulses from various core densities are shown to remain constant. Energy flux from the implosions, presented as a percentage of available hydrostatic energy, is shown to increase as a function of core density. Increased foam crushing energy at higher core densities, and increased damage observed in post-mortem specimens from heavier cores, are identified as mechanisms responsible for these behaviors.

Introduction

Implosion is a fluid-structure interaction problem that involves the buckling, collapse, and subsequent pressure pulse emission of an enclosed shell when external fluid pressure around the structure reaches critical value and the shell collapses dynamically. This process happens in distinct stages, with the first phase of instability initiation followed by a second phase in which the walls buckle inward at high velocities and local pressure in the surrounding fluid drops via Bernoulli's principle. After a point, these walls make contact with one another, and abruptly decelerate to zero velocity. As buckle propagation occurs, the sudden change in momentum of the walls simultaneously causes an immense pressure spike in the fluid, and a high pressure wave is released outward [1], [2].

Implosion has been studied for several decades, with early work in the field primarily focused on evaluating the acoustic pulses from deep sea implosions [3]–[5]. Following a series of high profile accidents and developing interest from the naval community, however, implosion research has been reinvigorated in recent years. In the first of these events, a photomultiplier tube at the Super-Kamiokande Neutrino Observatory imploded during filling, causing a chain reaction of pressure pulses that destroyed a total of 7000/11000 such tubes within the facility and cost an estimated \$20 million dollars of damage [6]. Later, the AUV *Nereus* imploded while on a deep-sea research dive off the coast of New Zealand. The vehicle had been expected to reach the deepest depths of the ocean consistently; its failure resulted in a substantial loss of confidence in the subsea engineering community, in addition to the monetary and opportunity cost of the vehicle itself [7]. Jointly, these accidents emphasize the need for increased understanding of the implosion phenomenon, in terms of both the buckling-based initiation of implosion as well as prediction and mitigation of its associated pressure pulse.

Several studies from the past decade partially address these gaps. Turner and Ambrico performed experimental and computational investigations of the implosion of both glass spheres and metal tubes, and were able to identify key stages in the implosion process, as well as develop effective computational models that agreed well with their experimental results [1], [2]. Farhat et al. investigated the implosion of metal cylinders, and demonstrated that changes in geometry affect both buckling pressure and collapse mode by performing well-corroborated experimental and computational studies [8]. Ikeda et al. performed experiments on the effect of geometry of metal tubes on the emitted pressure pulse from implosion [9]. Gupta et al. performed an experimental investigation of implosion, and used high speed photography and digital image correlation to determine collapse velocities and displacements across the surface of the tube, and related that information to pressure pulse emission [10].

Composite materials have also been studied with regards to the implosion phenomenon. Because of their excellent strength- and stiffness-to-weight ratios, as well as their natural corrosion resistance, they make excellent candidates for marine engineering applications, including those where implosion is a matter for concern. In that vein, the buckling of composite cylinders has been studied by several authors analytically and computationally, in an effort to predict their buckling mode shapes and critical collapse pressures [11]–[16]. Additionally, Pinto et al. studied the implosion behavior of glass- and carbon-fiber composite tubes. This work included the performance of digital image correlation during the collapse process, and investigated both buckling behavior and pressure pulse mechanics [17], [18]. The mitigation of implosion pressure pulses via the application of polyurea coatings was also investigated [19].

That said, the previously mentioned works have only investigated the implosion of isotropic materials and classical composite laminates; there remains little work on the implosion

of double hull-structured composite materials, where two facesheets of thin but strong material are concentrically assembled with a thick but comparatively low density core. Moreover, the work that does exist primarily focuses on the buckling of sandwich structures and doesn't address pressure pulse emission from the implosion process [20]–[26]. None of these studies include experimental verification of their analytical and computational results, and none address the effect of the sandwich construction on pressure pulse emission within the surrounding fluid.

The aim of this study is to experimentally investigate the implosion of double hull composite structures, considering both buckling performance, as well as pressure pulse analysis and mitigation. To most closely approximate the conditions of a submersible or other deep sea vehicle, cylindrical geometry will be investigated. Double hull composites have several unique advantages for this kind of application: in addition to the benefits of composite materials listed previously, double hull structures offer increased buckling resistance, excellent acoustic attenuation, and further increases in specific stiffness over monolayer composites [23].

This study marks the first time that the mechanics unique to a double hull implosion have ever been reported, with several key differences from the behavior of monolayer structures being observed. Double hull structures are found to emit “double pulses” during implosion wherein two distinct pressure pulses are registered, corresponding to the collapse of the outer and inner tubes, respectively. The facesheets are also found to collapse independently of one another, such that the inner tube may or may not survive the collapse of the outer tube, depending on external hydrostatic pressure. The outer tube is found to buckle and flatten against the inner tube, with a time delay sometimes occurring before the collapse of the inner tube, if it collapses at all.

Material Selection and Specimen Design

The specimens in this study use carbon-fiber/epoxy tubes manufactured by Rock West Composites (West Jordan, UT) for their inner and outer facesheets. The outer tube has a $[\pm 15/0/\pm 45/\pm 15]$ layup, with a nominal 60.4 mm ID and 1.7 mm wall thickness. The inner tube has the same layup and nominal thickness, but a nominal ID of 38.6 mm. Prior to assembly, the outer tube is painted by hand with a high-contrast, stochastic, black-and-white speckle pattern that covers half of its circumference and its entire length. During assembly, the tubes are mounted concentrically and sealed using aluminum endcaps such that their unsupported length is 279.4 mm. In addition to being sealed from water, the tubes are also sealed between one another so that water may not enter the inner tube in the event that the outer tube fractures or its seal is otherwise broken.

The PVC foam cores used in the specimens are from the Divinycell H series of foams, as produced and provided by DIAB, Inc. (DeSoto, TX). Foam cores of different densities from this are parametrically graded across trials: experiments are performed with Divinycell H35, H60, H80, and H100 foam cores, as well as with the foam core removed. In all cases, the foam cores have a nominal 41.9 mm ID, and 9.2 mm thickness. The cores are machined from flat sheets by first creating small rings with the aforementioned radial dimensions. The rings are then stacked on top of each other during assembly to match the 279.4 mm unsupported length of the composite facesheets.

Experimental Procedure

All experiments are performed using a semi-spherical pressure vessel of 2.1 meter diameter, with a maximum static pressure rating of 6.89 MPa, shown in Figure 1. The vessel is designed to maintain constant hydrostatic pressure through the collapse process, and has optical

viewports mounted radially around its midsection for photography and lighting during experiments. Two high-speed cameras (Photron SA1, Photron USA, Inc., San Diego, CA) are mounted coaxially with the portholes of the tank, such that a stereoscopic viewing angle of 17° is created toward the speckled surface of the double hull specimen after it is fixed within the vessel. This enables performance of underwater 3-D DIC in post processing, in the manner presented in [10], [17] and [18].

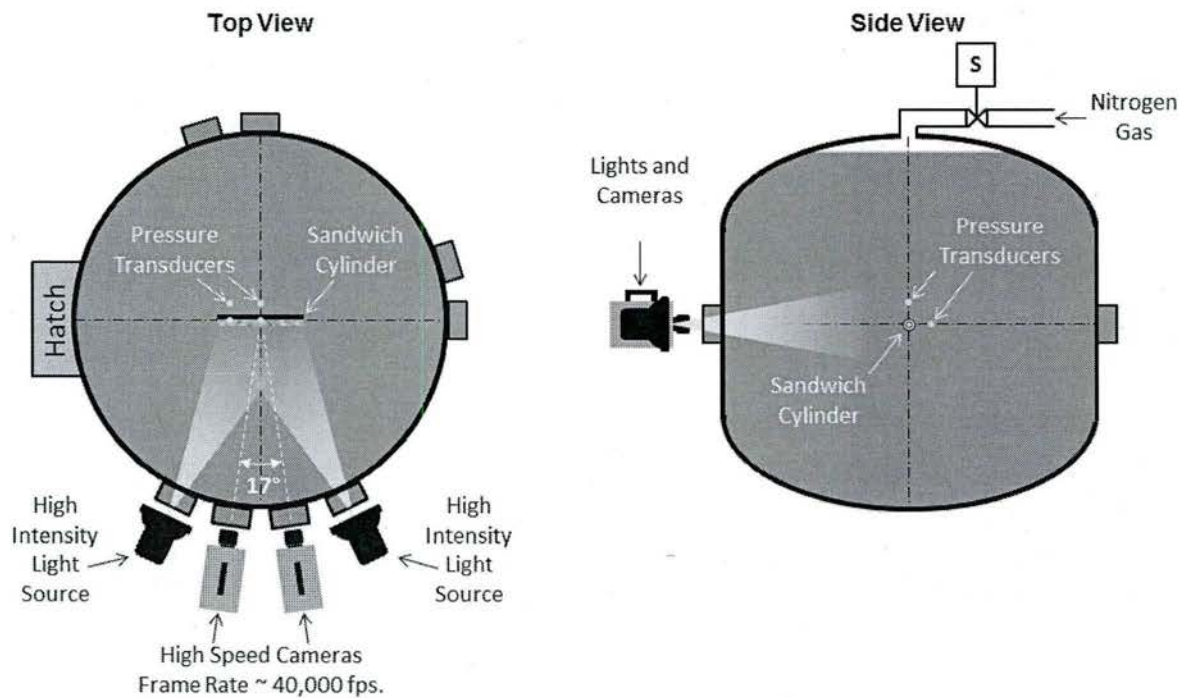


Figure 1: Experimental facility; (left) section through mid-height; (right) longitudinal section

To execute the experiments, specimens are mounted horizontally in the center of the vessel using thin steel cables that provide minimal acoustic reflections; the specimen is oriented such that the speckle pattern on the outer tube faces in the direction of the viewports and corresponding cameras. To monitor the pressure pulse emitted by the implosion, tourmaline

high-pressure blast transducers (PCB 138A05, PCB Piezotronics, Inc., Depew, NY) are mounted above and behind the implodable on its center and ends. All sensors are mounted with their sensing elements at a nominal radial distance of 50 mm from the face of the outer tube, with those on the ends located at a longitudinal offset of 127 mm from the midsection of the tube. The amplified output from the pressure sensors is monitored using an Astro-Med Dash 8HF-HS portable data recorder (Astro-Med Inc., West Warwick, RI) at a sampling rate of 2 MHz. Once mounting is complete, the vessel is filled with filtered water, and sealed. Nitrogen gas is introduced to an air pocket at the top of the vessel to pressurize the fluid at a rate of approximately 0.083 MPa/min. Once critical pressure is achieved and implosion occurs, the cameras and pressure sensors are simultaneously end-triggered and their data saved, such that image and pressure data are directly matched in time.

Analysis

Increase in collapse pressure

The collapse pressure of double hull structures with a foam core increases with the stiffness of the foam. When listing collapse pressures in this study, only those of the outer tube are given. This allows for direct comparison between cases regardless of whether the inner tube collapses or not, and is used when listing all collapse pressures or changes thereof, unless otherwise noted.

In predicting the collapse pressures of double hull structures, it was decided to focus on the increase in collapse pressure of the tubes on account of the double hull structure, rather than absolute pressures. The increase in collapse pressure of a particular specimen is given by:

$$\Delta P_{cr} = P_{cr} - P_{cr,0} \quad (1)$$

Where ΔP_{cr} is the increase in collapse pressure of the outer tube due to the double hull structure, P_{cr} is the experimentally measured collapse pressure of that specimen, and $P_{cr,0}$ is the estimated collapse pressure of that same specimen if its foam core were to be removed.

Composite Thickness Effects on Collapse Pressure

In analyzing collapse pressure, it is necessary to account for thickness variation in the outer tubes: small inconsistencies in the manufacturing process of the tubes resulted in variation of average thickness by as much as 0.254 mm, and the collapse pressures of composite tubes are sensitive to variations in thickness.

From literature, the following equation can be used to estimate the collapse pressure of a composite cylinder without a foam core [27]:

$$P_{cr} = \frac{\gamma \sqrt{E_1 E_2} t^{5/2}}{(1 - \mu_{12} \mu_{21})^{3/4} L R_c^{1/2} R_o} \left(\frac{1}{1 + \frac{\sqrt{E_1 E_2} I}{R_c R_o t G}} \right) \quad (2)$$

Where γ is a constant that depends on geometry, E_1 and E_2 are the longitudinal and hoop moduli of the composite cylinder, t is average thickness, μ_{12} and μ_{21} are the anisotropic Poisson's ratios, L is Length, R_c is average cylinder radius, R_o is outer cylinder radius, I is moment of inertia about the centerline, and G is shear modulus. Equation (2) shows that critical collapse pressure scales by a factor of $t^{2.5}$. It follows that:

$$\frac{P_{cr,1}}{P_{cr,2}} = \frac{t_1^{2.5}}{t_2^{2.5}} \quad (3)$$

Where $P_{cr,1}$ and $P_{cr,2}$ are the collapse pressures of two similar tubes with different average thickness, and t_1 and t_2 are those thickness values. For the outer tubes used in this study, Equation (3) predicts the relationship between collapse pressures within 0.5 % for the hollow specimens. Equation (3) can be rearranged to predict the collapse pressure of the outer tube of a given specimen with its core removed:

$$P_{cr,0} = \frac{t_0^{2.5}}{t_{ref}^{2.5}} P_{cr,ref} \quad (4)$$

Where $P_{cr,0}$ is the predicted collapse pressure of the outer tube of a given specimen, and t_0 is that specimen's measured thickness. $P_{cr,ref}$ and t_{ref} are the collapse pressure and thickness of the reference specimens in this study, which had their cores removed when experimented on. Thus the change in the collapse pressure of a double hull specimen is given by:

$$\Delta P_{cr} = P_{cr} - \frac{t_0^{2.5}}{t_{ref}^{2.5}} P_{cr,ref} \quad (5)$$

Careful thickness measurements of the outer tube were needed to make accurate predictions of the collapse pressure of the double hull structure using Eq. (5).

ΔP_{cr} is critical in evaluating the true effect of core material on collapse pressure, as discussed later. This is a very important quantity in the design of subsea vehicles, where avoiding collapse is paramount.

Impulse

The area under the pressure-time curve is often of more importance in terms of measuring implosion damage potential than the magnitude of the pressure alone. To that end, the following equation is employed [28]:

$$I = \int_0^t dP dt \quad (6)$$

Where I is the impulse per unit area imparted to the water by the wavefront, dP is dynamic pressure, and t is an arbitrary time of interest. In order to simplify the problem, the total impulse is calculated here for the underpressure regions only, under the assumption that the impulse for the overpressure region will be equal in magnitude, as discussed in [1], [8], [10].

It will be shown in the results section of this paper that some double hull structures release “double pulses” during implosion wherein two distinct pressure pulses are emitted, each corresponding to the collapse of the outer and inner tubes. In such cases, the following formula is used:

$$I_{total} = \int_0^{t_1} dPdt + \int_{t_2}^{t_3} dPdt \quad (7)$$

Where I_{total} is the total impulse per unit area of the double hull structure's collapse, t_1 is the time at which the first underpressure region crosses the t-axis, t_2 is the time at which the second underpressure region begins as the pressure traces crosses below the t-axis again, and t_3 is the time at which the second underpressure region ends as the pressure trace crosses the t-axis a third time.

In order to compare the impulse behavior of the various foam cores, it is necessary to account for differences in collapse pressure caused by differing core strengths. The following formula is used, which normalizes the impulse values from Equation (7) with respect to collapse pressure:

$$I_{norm} = \frac{\int_0^{t_1} dPdt + \int_{t_2}^{t_3} dPdt}{\int_0^{t_1} P_{cr}dt + \int_{t_2}^{t_3} P_{cr}dt} \quad (8)$$

Here, I_{norm} is the total impulse per unit area of the wavefront, normalized by an impulse term associated with the collapse pressure of the specimen in question. Generally, the impulse of an implosion scales with the ambient hydrostatic pressure at which the implosion occurred. Equation (8) removes this effect via normalization, and allows for direct comparison of impulse between cases with different collapse pressures.

Energy

An acoustic energy flux analysis is also performed to measure implosion damage potential, where the afterflow energy flux through a surface some arbitrary distance from the event is given by [29]:

$$E_F = \frac{I_{total}^2}{2\rho_0 R_s} \quad (9)$$

Where E_F is acoustic energy flux, ρ_0 is the density of the fluid, and R_s is the distance of the sensor from the surface of the collapsing tube. Assuming a spherical pressure wave, the energy flux given by Equation (9) can be multiplied by the surface area of a sphere of radius equivalent to the standoff distance of the sensor to yield the total afterflow energy of the implosion pulse:

$$E_A = E_F(4\pi R_s^2) \quad (10)$$

To compare directly between cases with differing collapse pressures, it is necessary to normalize this value with available hydrostatic energy:

$$E_{norm} = \frac{E_A}{E_H} \quad (11)$$

Where E_H is available hydrostatic energy prior to collapse, given by:

$$E_H = P_{cr}(\Delta V_{implosion}) \quad (12)$$

and $\Delta V_{\text{implosion}}$ is the difference in displaced fluid volume before and after the implosion.

Results and Discussion

Predicting Collapse Pressure

It is important to be able to predict the buckling behavior of a double hull structure as a function of material and geometrical properties. To that end, a series of experiments were performed to determine the mechanical properties of the foam core materials (Table 1)[30]. Comparing the stress-strain curves from those tests to the radial predeformation strain immediately prior to buckling (Table 1), it can be seen that buckling always occurred in the foam-crushing region of the stress-strain curve. Plotting the measured crushing strengths of the various foams against the ΔP_{cr} values measured previously, a linear trend is observed in Figure 2A, intersecting the origin and having a nondimensional slope of 2.6. This implies that for the given core geometry, it would be possible to find an even higher strength core than those studied here, and that applying such a core in the specimen would very likely increase buckling strength along the line in Figure 2A.

Foam Name	Measured Density (kg/m ³)	Measured In-Plane Crushing Strength (MPa)	Predeformation Strain at Buckle Initiation (%)
H35	38	0.228 ± 0.008	11.1 ± 0.6
H60	60	0.445 ± 0.015	18.9 ± 2.1
H80	80	0.653 ± 0.018	11.1 ± 0.7
H100	100	0.967 ± 0.044	20.5 ± 4.9

Table 1: Relevant quasi-static foam core properties and data

Plotting ΔP_{cr} values versus the measured density of each foam core (Table 1) gives the data shown in Figure 2B. The trend is nonlinear for this series of foams. This is noteworthy from an applications perspective because it is often desired to minimize the weight of underwater vehicles. It is possible that the mass-efficiency of the core increases with density for this series of foams, such that higher density cores are both stronger and more efficient per unit mass. This has not been validated.

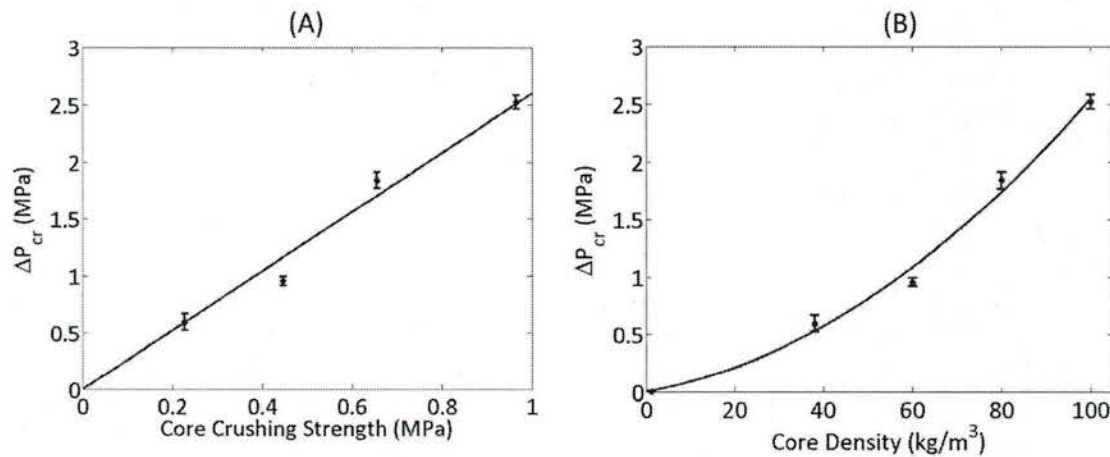


Figure 2: Increase in collapse pressure as a function of (A) foam core crushing strength; (B) foam core density

Collapse Behavior Categories

Three overarching behaviors were observed in the collapse of the double hull specimens. In 1), the outer tube collapsed and crushed the foam core but the inner tube did not collapse. In 2), the outer tube collapsed and crushed the foam core, after which there was a brief dwell time before the inner tube collapsed. In 3), the outer tube collapsed, crushed the foam core, and collapsed the inner tube in a singular motion, with no dwell in between.

The outer tubes in this study collapsed in mode 3, whereas the inner tubes collapsed in an asymmetrical mode 2, if they collapsed at all (Figure 3). In all cases where the inner tube collapsed, the outer tube collapsed first, then remained crushed against the surface of the inner during the latter's collapse, conforming to its shape. In behaviors 1) and 2), the outer tubes formed around the shape of the inner tube, rendering the inner's shape clearly visible; there was not time for this to occur when the inner and outer tubes collapsed in a singular motion.

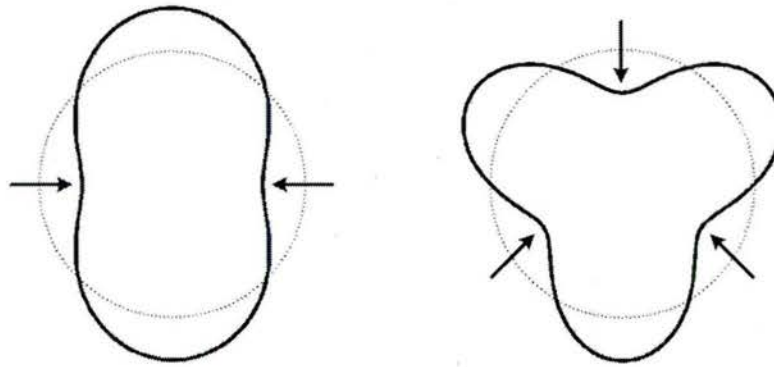


Figure 3: Example collapse mode shapes; (left) mode 2; (right) mode 3

The difference in collapse mode between the inner and outer tubes had no effect on the instability of the inner tube: collapse pressure of the inner tube was the dominant factor. The addition of a core increased the collapse pressure of the outer tube, sometimes to levels above that of the inner tube. The collapse pressure of the outer tube had to be higher than that of the inner tube (inner tube collapse pressure is approximately 2.4 MPa) for the inner tube to collapse.

Detailed results from each case are presented here, with data from similar collapse behaviors grouped together to enable comparison.

DIC Contours

DIC was utilized to obtain velocity and position data for the imploding cylinder to provide insight into the collapse mechanics of the double hull structure. Radial velocity data was extracted from a line spanning the half-length of the tube, such that a longitudinal position of 0 corresponds to the tube's center. This data was taken from the duration of the collapse, allowing for comparison in time and longitudinal position. Images of the specimens at key stages of its collapse were also used in conjunction with DIC contours of radial displacement to gain further understanding of collapse mechanics.

Outer Tube Only Collapse

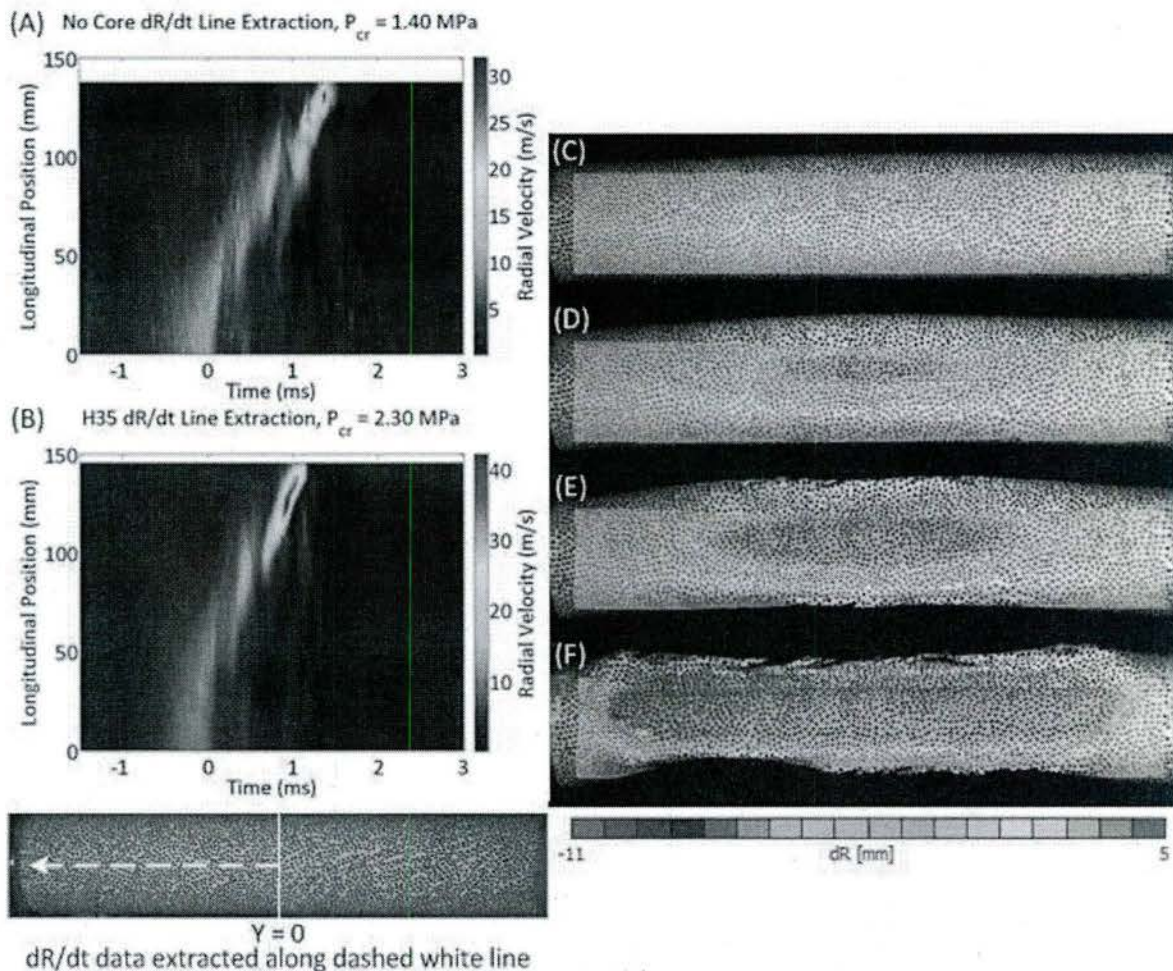


Figure 4 Figure 4 (A) and (B) show velocity contours for cases where the outer tube collapsed and the inner did not. Both cases demonstrate this overarching behavior, though there is no foam core in (A) and there is one in (B). Typically during implosion, wall contact occurs first at the center, and then propagates longitudinally in a phase commonly referred to as buckle propagation, as has been reported in [10], [17], [18]. The same behavior can be seen here, though in this case wall contact is made between the outer and inner tubes, with the crushed foam core between the two. The center of the tube registers a velocity first, reaching a maximum of about 12 m/s then dropping off to 0 when wall contact occurs. Following that, buckle propagation is observed as radial velocities of approximately 12 m/s spread along the length of the tube in time, then drop to zero as wall contact is made at greater positions along the length of the tube. The result is a half-crescent shape that is curved to the right in each contour. The highest radial velocities are measured near the endcaps in both cases: this is because the slope of the buckle increases as it propagates along the length of the tube, leading to dramatically higher radial velocities near the end of the tube [Figure 4 (C) through (F)]. Similar behavior has been observed in aluminum tubes [10]. Also of note are the higher overall radial velocities in (B), where those seen during buckle propagation are approximately 15 m/s. This is because collapse pressure in (B) is 0.9 MPa higher than in (A), a difference of 64.3%.

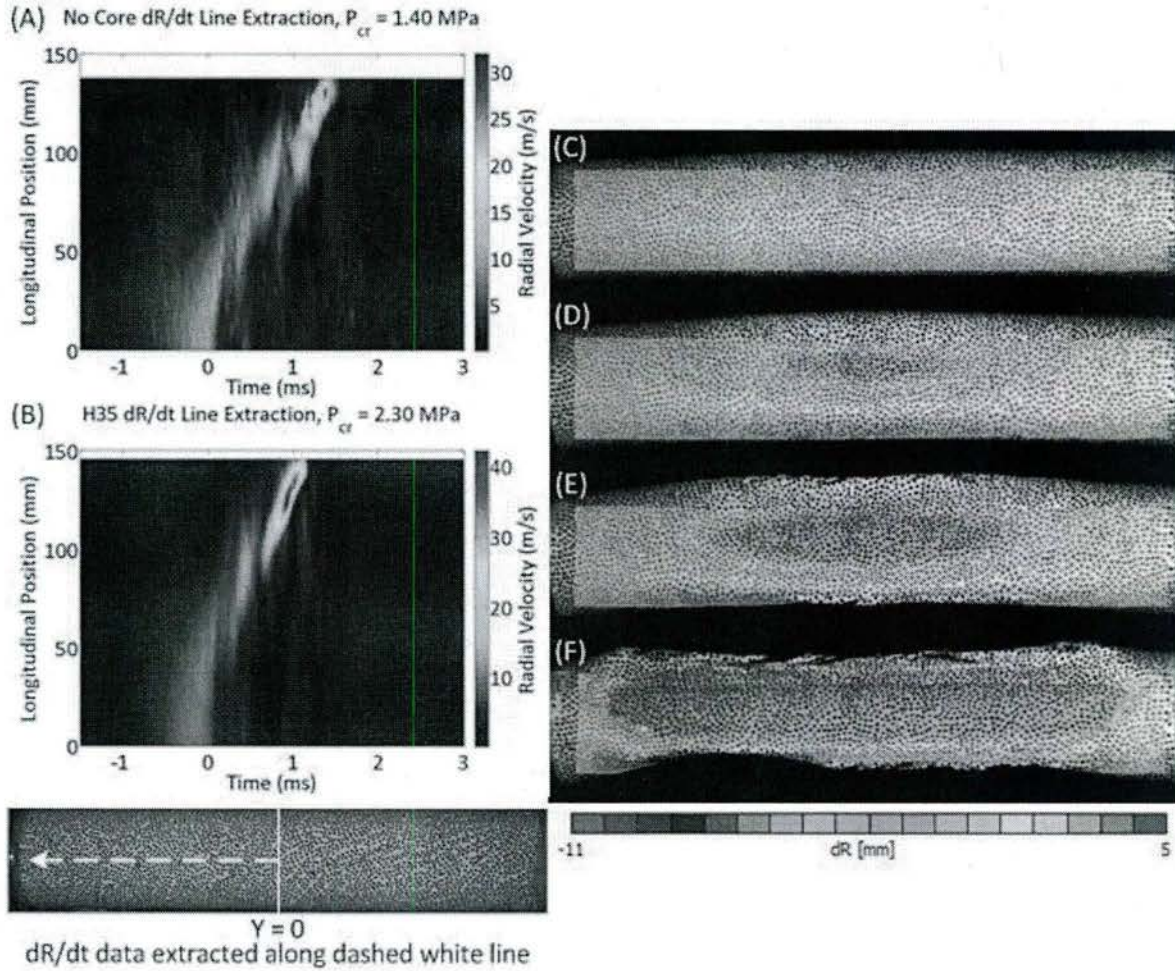


Figure 4: DIC data for outer tube only collapse cases; (A) dR/dt line extraction for no core case; (B) dR/dt line extraction for H35 core case; (C)[-2.003 ms] Image of H35 core specimen prior to buckling, with dR contours superimposed; (D)[-0.003 ms] complete core crushing at midpoint; (E)[0.417 ms] buckle propagation of collapsed outer tube against inner tube; (F)[1.017 ms] completed collapse, with profile of uncollapsed inner tube visible;

Complete Collapse, With Dwell

Figure 5 (A) and (B) show velocity contours for cases where the outer tube collapsed, a brief dwell occurred, and then the inner tube collapsed. Here, the outer tube collapses with very

similar mechanics to those seen in the previous section, exhibiting the same crescent shape seen in the velocity plots, with highest velocities at the endcaps. The inner tube demonstrates different collapse mechanics however, as it exhibits constant collapse velocities along its length, and does not undergo buckle propagation. This can be seen in the figure from around time 1.0 ms onwards in (A), and 1.3 ms in (B). In each instance, similar velocities occur along the tube length, with the result being a vertical line of high velocity instead of the half-crescent shape common to buckle propagation.

The collapse of the inner tube happens more slowly in (A) than in (B). In the H60 case, the inner tube implodes with velocities of 10-12 m/s consistently being registered along the length of the tube, whereas in the H100 case, velocities are commonly 20-25 m/s along the length of the tube and occasionally reach as high as 30 m/s. Maximum velocities in (A) are also lower than those in (B), with the former demonstrating peak velocities of approximately 35 m/s while the latter shows about 45 m/s. This is because collapse pressure in (B) is 1.74 MPa higher than in (A), a difference of 67.7%.

Total collapse duration for the H60 specimen [Figure 5 (A)] is 3 ms, greater than that for any other case. This occurs because the ratio between hydrostatic pressure and inner tube collapse pressure is about 1.1 in the H60 case, while being 1.7 for the H100 case. In the former, the ratio is small enough that the pressure exerted on the inner tube during the dwell takes longer to overwhelm it, so it doesn't collapse until about 1.5ms after the implosion of the outer tube. Because the ratio is much higher for the H100 case, the duration of the dwell time is reduced, and the inner tube implosion begins about 1ms after the implosion of the outer tube. For foam cores of lower strength, the outer/inner P_{cr} ratio does not exceed 1, so the inner tube does not

collapse. Because the ratio is just over 1 for the H60 specimens, that case features the longest dwell time.

The uniform longitudinal collapse of the inner tube is likely due to material damage in the inner tube causing an asymmetric collapse (visible from post-mortem specimens) that does not comply with the modal symmetry given by structural stability theory [31], [32].

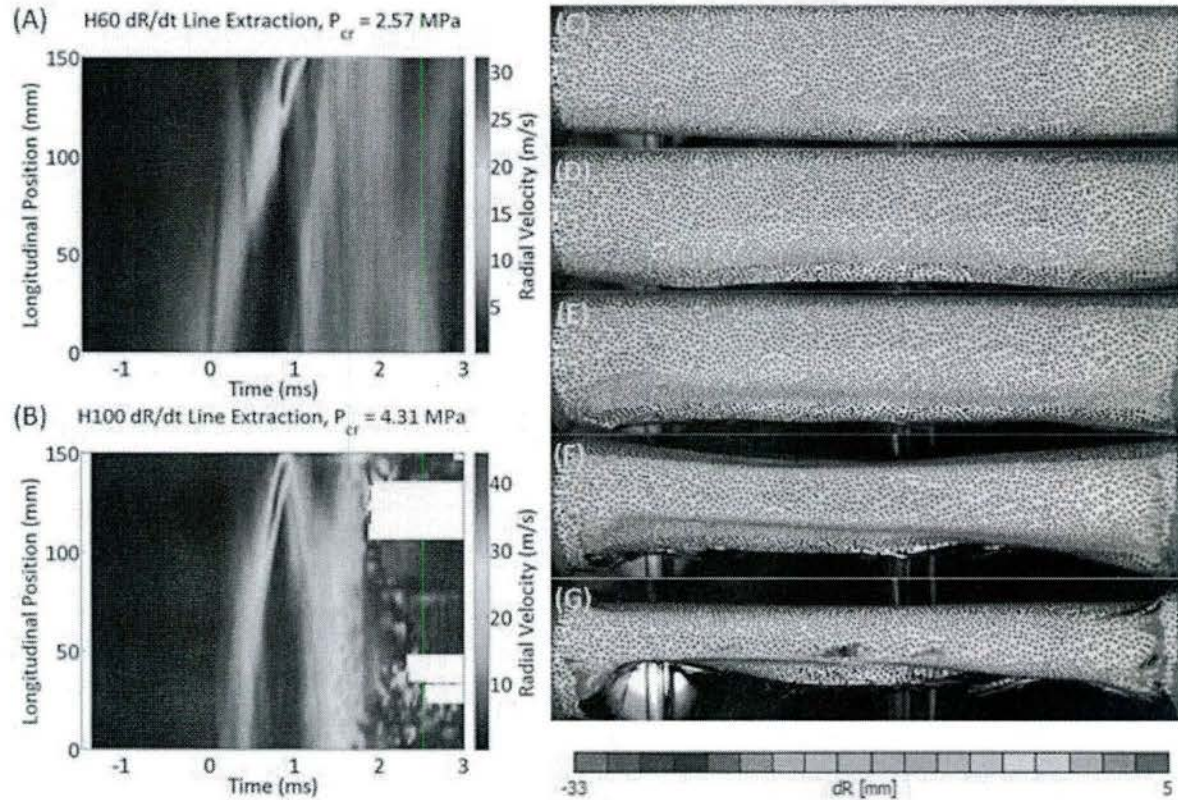


Figure 5: DIC data for complete collapse with dwell cases; (A) dR/dt line extraction for H60 core case; (B) dR/dt line extraction for H100 core case; (C)[-1.0115 ms] Image of H100 core specimen prior to buckling, with dR contours superimposed; (D)[0.4818 ms] complete core crushing at midpoint; (E)[0.8818 ms] end of buckle propagation of outer tube along inner tube; (F)[1.4685 ms] initiation of collapse of inner tube; (G)[2.0018 ms] completed collapse;

Complete Collapse, Without Dwell

Figure 6 (A) shows a velocity contour for the case where the outer tube collapses on the inner in a singular motion with no time delay in between. This type of collapse happens when the natural buckling modes of the inner and outer tubes align with one another, discussed later.

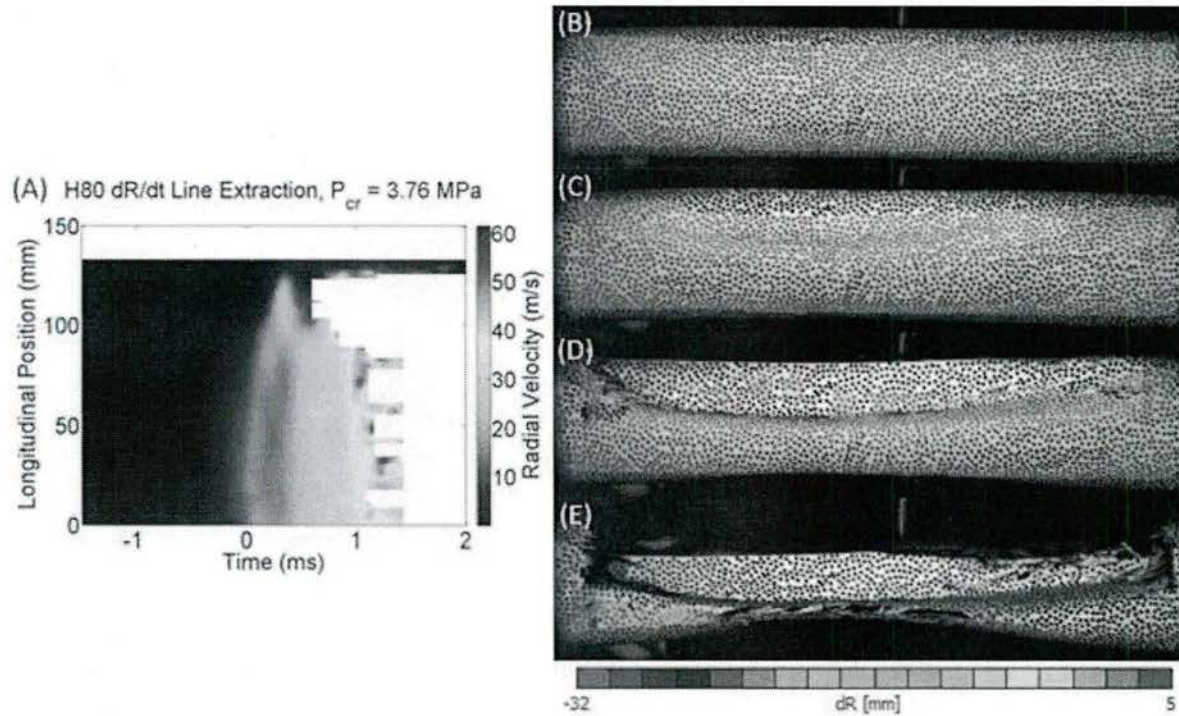


Figure 6: DIC data for complete collapse without dwell case; (A) dR/dt line extraction for H80 core case; (B)[-0.8160 ms] Image of H80 core specimen prior to buckling, with dr contours superimposed; (C)[0.1173 ms] complete crushing of foam core at midpoint; (D)[0.6240 ms] collapsing inner tube – note lack of buckle propagation of outer tube against inner; (E)[1.1040 ms] completed collapse;

A unique feature of (A) is that maximum collapse velocity is on the order of 60 m/s, at least 50% higher than that seen in other cases. This velocity is located along the midsection of the tube, similar to the inner tube collapse mechanics described in the previous section. These

velocities are achievable because, without the dwell observed in other cases, the pressure in the fluid continues to accelerate the structure inward through the duration of the structure's motion. Additionally, uniform high velocities are seen to occur along the length of the structure in time as the inner tube collapses, in much the same manner as described in the previous section. These similarities occur despite the removal of the dwell period. This implosion is also the fastest of all cases, with a total duration of 1.4 ms.

Double Hull Implosion Pressure Pulse

Outer Tube Only Collapse

Figure 7 shows the pressure pulse emitted in cases where only the outer tube collapses. Following buckling initiation at (A), there is a relatively smooth underpressure region until time 0 at (B), defined as the point at which matrix cracking begins in the tube. Defining the onset of matrix cracking in the outer tube as time 0 is convenient for composite double hull tubes, because it consistently occurs at similar radial deflections between cases, whereas complete foam crushing and wall contact can vary depending on foam core density. Crack initiation at (B) results in high frequency variations in pressure being introduced to the signal, as well as a drop in pressure immediately after cracking begins. At this point, the inner tube is still moving inwards radially, but eventually stops at (C): in the no-core case, this corresponds to wall contact, and in the H35 case, this corresponds to complete crushing of the foam core against the inner tube. After this point, the pressure in the fluid rapidly increases to a maximum at (D), which is concurrent with the collapsed zone of the buckle spreading outward. The pressure spike occurs on account of the sudden change in momentum of the fluid.

The characteristics of the pressure pulse seen for the double hull cylinders are similar to what has been reported in the literature for monolayer composite structures, but the “peakiness” of the behavior, as well as the maximum dynamic overpressure from the implosion, are reduced substantially in this configuration compared to the single-cylinder configuration of similar dimensions reported in [17]. This reduction in overpressure is due to the reduced potential energy of the event, shown with Equation (12): when the inner tube survives, the change in volume $\Delta V_{\text{implosion}}$ from implosion is reduced, and the less energetic event results in measurable reductions in waveform amplitude. Additionally, the outer tubes in this study collapse entirely in a mode 3 shape, while the tubes in [17] initiate collapse in mode 3 but finish their collapse in mode 2. In this study, the presence of the inner tube prevents the dynamic mode change. Because of the 3-lobe shape here, one of the valleys collapses against the inner tube first, while the other two lobes wrap around the tube. Displaced fluid volume continues to be reduced by this action, absorbing energy. The result is that the high-frequency pressure pulse observed in the single tube configuration is largely eliminated.

In the H35 case, shown on the bottom of Figure 7, the presence of the foam core causes energy absorption from cell crushing, and prevents outright wall contact; instead, the foam core densifies to a point where it cannot be crushed more, and a quasi-wall contact is made. This causes a less abrupt change in fluid momentum which, combined with the aforementioned factors, reduces frequency and amplitude in the dynamic overpressure signal as compared with that of the reference.

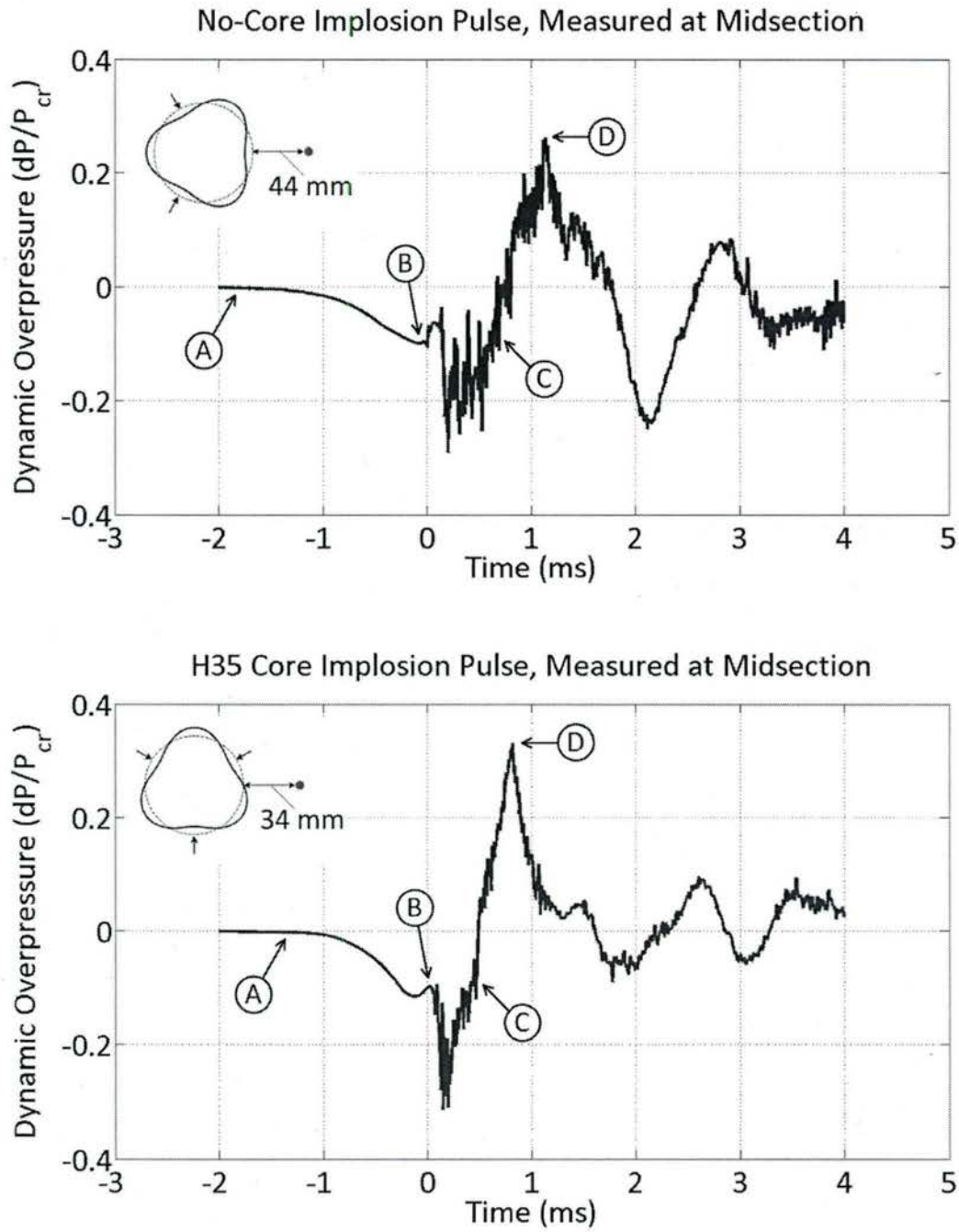


Figure 7: Normalized pressure pulses from cases where only the outer tube collapsed;(top) No-core case; (bottom) H35 foam core case; (inset, top left, both figures) outer tube buckling mode shape and sensor location

Complete Collapse, With Dwell

Figure 8 shows the pressure pulse recorded in cases where the outer tube collapses, a brief dwell occurs, and then the inner tube collapses. Here, buckling initiation of the outer tube occurs at (A), followed by a smooth underpressure region that exists until the onset of matrix cracking and associated drop in fluid pressure at (B). The underpressure region then continues until (C), where the pressure trace crosses the t-axis and an initial over-pressure corresponding to the collapse of the outer tube against the inner is recorded at (D). Following that, the inner tube begins to buckle because the hydrostatic pressure is greater than it can survive on its own. What follows is a secondary implosion pulse corresponding to the collapse of the inner tube, with a new underpressure region in the pressure signal being created at (E). At (F), there is a spike in pressure which corresponds to the development of damage in the inner tube as it collapses. The underpressure region continues until (G), where the inner tube makes wall contact with itself, and a secondary pressure peak is created which exceeds that of the first in amplitude.

In the H100 case, the amplitude of the first pressure spike is much lower than that of the H60 case, because more energy is absorbed through core compressive strain during implosion. This is because of the higher modulus and crushing strength of the H100 foam. However, the secondary spike is of much greater amplitude in the H100 case. This is because collapse pressure is substantially higher, for greater E_H . The foam core absorbs relatively little energy during the collapse of the inner tube because it is already crushed, so its mitigating effects are minimized during that portion of the collapse. Finally, the time delay between the inner- and outer-tube pulses is greater for the H60 case than any other. This is because of the uniquely long dwell time for the H60 case.

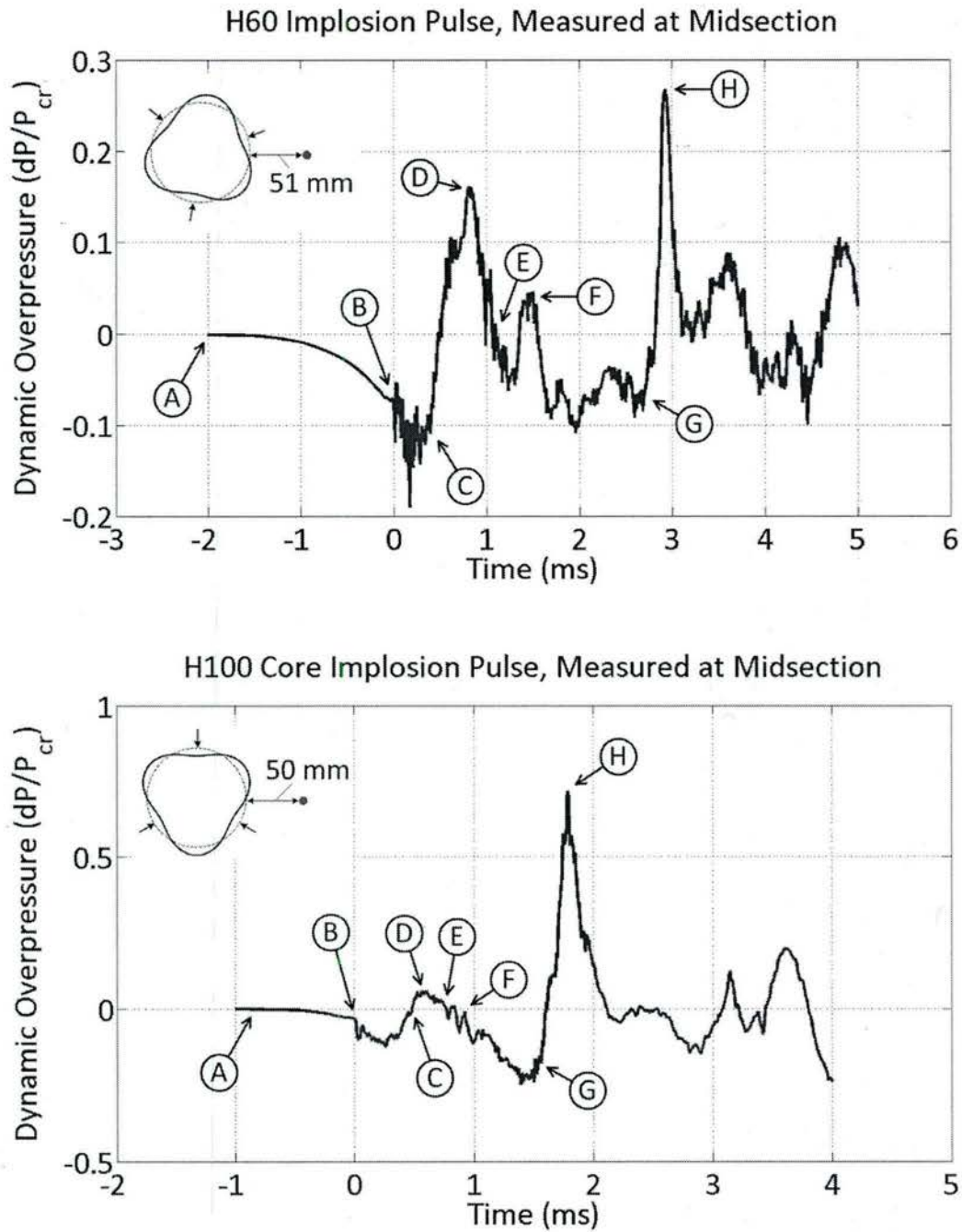


Figure 8: Normalized pressure pulses from cases where the outer tube collapsed, dwelled briefly, then the inner tube collapsed; (top) H60 foam core case; (bottom) H100 foam core case; (inset, top left, each plot) outer tube buckling mode shape and sensor location

Complete Collapse, Without Dwell

Figure 9 shows the pressure pulse emitted when the inner and outer tubes collapse in a singular motion. At (A), buckling initiation occurs, followed by a smooth underpressure region until (B), where extensive damage begins in the outer tube. As the inner tube begins to collapse, a small spike in pressure is seen at (C), likely corresponding to the development of damage in the inner tube. At (D), the inner tube makes wall contact with itself, and a large pressure spike is registered at (E).

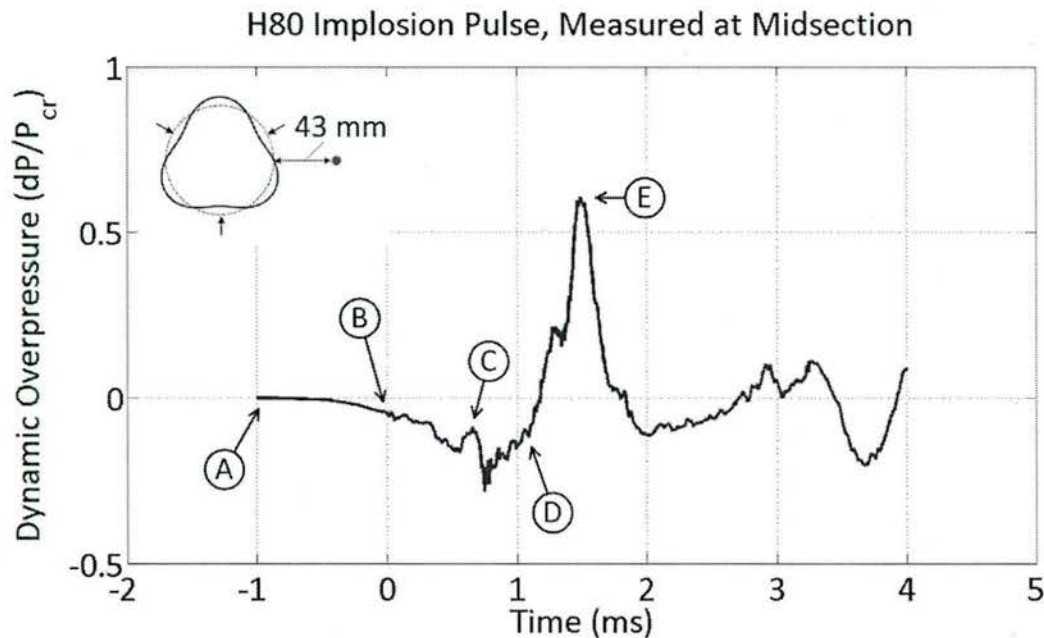


Figure 9: Normalized pressure pulse measured at mid section of the H80 foam core case where the outer tube and inner tube collapsed in a singular motion; (inset, top left) outer tube buckling mode shape and sensor location

The pressure pulse of a straight-through collapse appears qualitatively similar to that of the outer tube only collapse, but the underpressure region is of greater duration. This is because

the tube collapses a greater distance radially in one motion, so the associated underpressure duration is increased. Additionally, the pressure spike recorded in this case is of greater amplitude than that where only the outer tube collapses. This is due to the greater potential energy of the event: change in volume is increased substantially when the inner tube implodes, so the pulse released is larger.

The peak amplitude of the straight through collapse is less than that reported in literature for composite tubes of similar geometry [17]. In the reference, specimens similar to the outer tube in this study emitted a maximum dynamic overpressure of approximately 0.8, whereas the same value reported here is 0.6. That is despite the substantial increase in collapse pressure in the double hull case (3.76 MPa vs 1.61 MPa in the reference). This reduction in maximum overpressure despite increases in collapse pressure clearly demonstrates the mitigating effect of the foam core.

Impulse and Energy

I_{norm} for various implosion cases is plotted in Figure 10A, with foam core density on the horizontal axis. To allow for direct comparison between cases, the integrals from t_2 to t_3 in both the numerator and denominator are taken to be zero for instances where the inner tube did not collapse. The results are constant with foam core density, which implies that the impulse is mainly a function of collapse pressure, and is not directly influenced by core density or other properties. The exception to this trend in the data is the case of the H60 core, which has a lower magnitude normalized impulse. The reason for this is because of the uniquely long time delay between inner and outer tube collapses for these cases. As a result, it can be concluded that foam core properties do not directly affect impulse, with collapse pressure being the dominant factor instead.

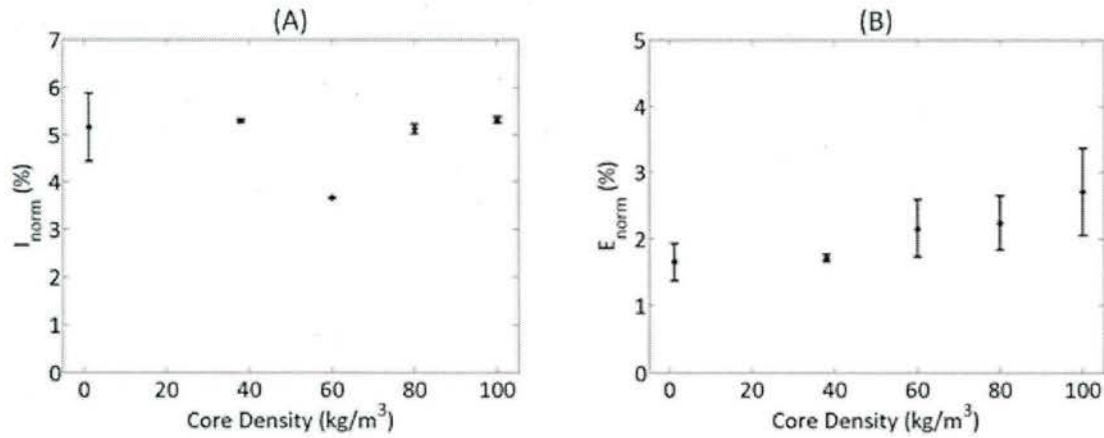


Figure 10: Implosion emissions as a function of core density showing (a) normalized underpressure impulse; (b) normalized waveform energy

A plot of normalized energy values, which present the energy emitted by the implosion event as a function of available hydrostatic energy, is given in Figure 10B. There, normalized energy released is constant with core density, although there is more variation in the H60, -80, and -100 cases. This is because the inner tube collapses in the aforementioned cases, and introduces new damage mechanisms. Nevertheless, a definite increasing trend is observed.

Post-Mortem Specimen Evaluation

The post-mortem analysis of the specimens yields additional insight into the mechanics of the collapse process, and helps to explain the energy mitigation behavior discussed above. Generally, damage in heavier foam core cases is more extensive because stronger foam cores enable higher collapse pressures: in the H100 case, P_{cr} is approximately triple that of the H35 case, and because the inner tube also collapses, the energy of the event is increased even further. This enables new damage mechanisms, which causes greater overall energy absorption in the heavier foam core cases.

Outer Tube Only Collapse

Figure 11 shows post-mortem images of the H35 foam core case, where only the outer tube collapsed. At (A), there are longitudinal, through-thickness cracks in the outer tube, corresponding to the mode 3 shape of the specimen. These connect to cracks in the circumferential direction at the endcaps (B), where complete fiber failure is observed as the endcaps shear the material during the dynamic collapse. At (C), the surviving internal tube can be seen, with little to no apparent damage. The crushing of the foam core in mode 3 shape can be seen at (D), where the foam core has not recovered elastically at the locations where the outer tube buckles inward. A mode 3 buckling shape can clearly be seen in the crushed shape of the core, reinforcing earlier findings suggesting that core crushing absorbs energy during the outer tube's implosion. Finally, note that the outer tube is largely elastically recovered from its imploded shape; this is characteristic of the implosion of all composite tubes, not just double hull specimens.

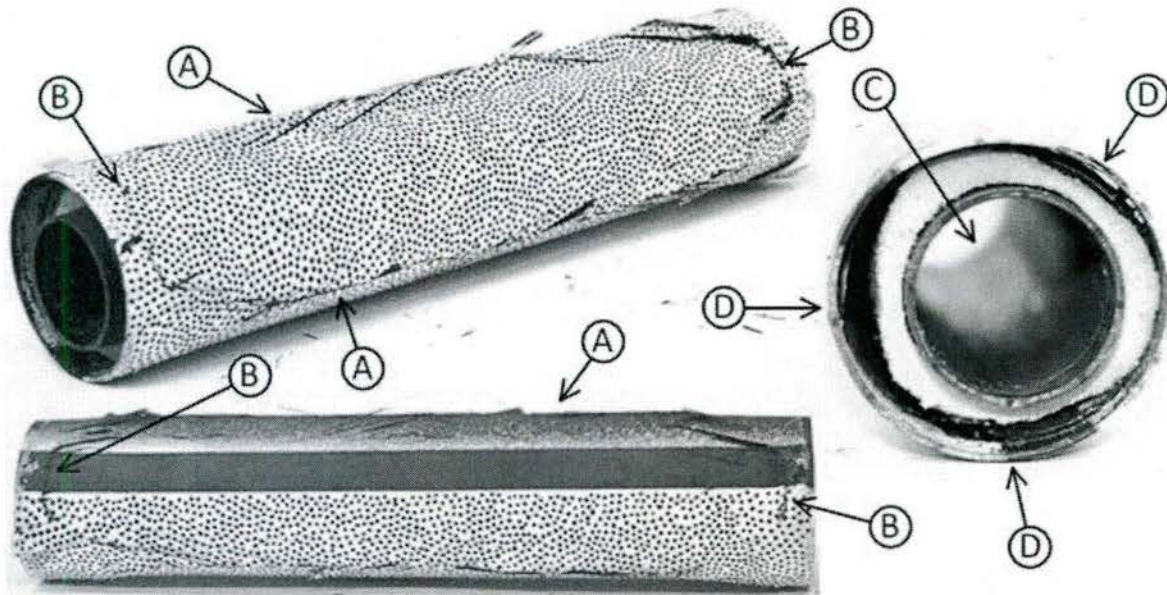


Figure 11: H35 core post-mortem specimen photographs; (top left) isometric view; (bottom left) top view; (right) right view; (A) longitudinal through-thickness cracks in outer tube, corresponding to mode 3 buckling shape; (B) circumferential through-thickness cracks from endcaps; (C) Intact inner tube; (D) foam core crushing in mode 3 shape.

Complete Collapse, With Dwell

Figure 12 shows post-mortem images of the H100 foam core case, which collapsed completely but with a time delay between tubes. At (A), longitudinal, through-thickness cracks corresponding to a mode 3 shape are seen. In this case, one of those cracks has developed into a complete tear, indicated at (B). One half of the tear folded under the other as the inner tube collapsed in an asymmetric mode 2 shape; this occurs in all specimens where the inner tube implodes in addition to the outer.

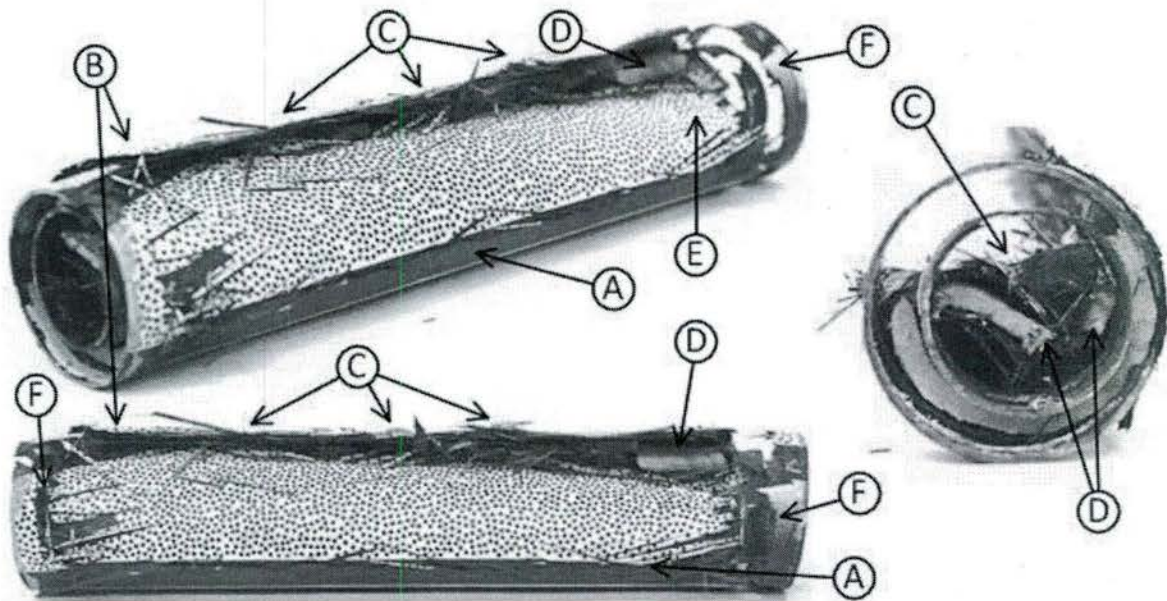


Figure 12: H100 core post-mortem specimen photographs; (top left) isometric view; (bottom left) front view; (right) right view; (A) longitudinal through-thickness cracks in outer tube, corresponding to mode 3 buckling shape; (B) Edge of through thickness tear, where the outer tube has completely cracked and folded under itself; (C) Delamination at tear edge; (D) Torn foam core; (E) Incomplete elastic recovery; (F) circumferential through-thickness cracking from endcap shear.

Several important instances of damage should be noted at the tear. First, the fibers along the tear have all failed, with substantial fiber pullout visible. There is also significant delamination at the tear face (C), visible at both the ends of the tube as well as the surface of the damage itself. The tear propagated to the foam core (D). The carbon/epoxy material of the outer and inner tubes has also not recovered to cylindrical shape (E) after being removed from the pressurized environment of the water. This is because the broken fibers from the tubes intertwine with one another where the tear and fold-under occurs, and also cut into the foam core

material. This prevents them from returning to their original shape, and implies the presence of residual stress in the material, even after it is removed from water.

Finally, at (F), circumferential cracks from endcap-induced shear are seen. The cracks extend entirely around the circumference of the specimen on one end and largely around it on the other, and the portion of the outer tube that was supported by the endcap is entirely detached on one end.

Complete Collapse, Without Dwell

Figure 13 shows post-mortem images of an H80-core specimen, where the inner and outer tubes both collapsed in a singular motion. At (A), cracks corresponding to a mode 3 buckling shape can be seen. These generally occur on the lobes of the collapse shape, so that the areas between these cracks experience the highest radial velocities inward. At (B), the location where the outer tube collapsed on the inner can be seen, with a fold where the inner tube buckled inward. Note that this fold occurred directly between the lobes indicated by cracks (A), and that there is another mode 3 lobe crack on the outer tube, at the exact opposite side of the outer tube. This indicates that collapses with no dwell occur when the directions of the tubes align with one another (Figure 14), which is supported by high-speed imagery from the event [Figure 6 (B) through (E)]. Beyond that, there is complete through-thickness fracture of both the tubes and the foam core at the center of the folded-in location, as well as at the top and bottom hinges where the fold-in occurs (C). There is substantial delamination and fiber pullout in these areas (D). Finally, circumferential cracks created by shear from the endcaps can be seen at (E), which extend almost entirely around the circumference of the tube.

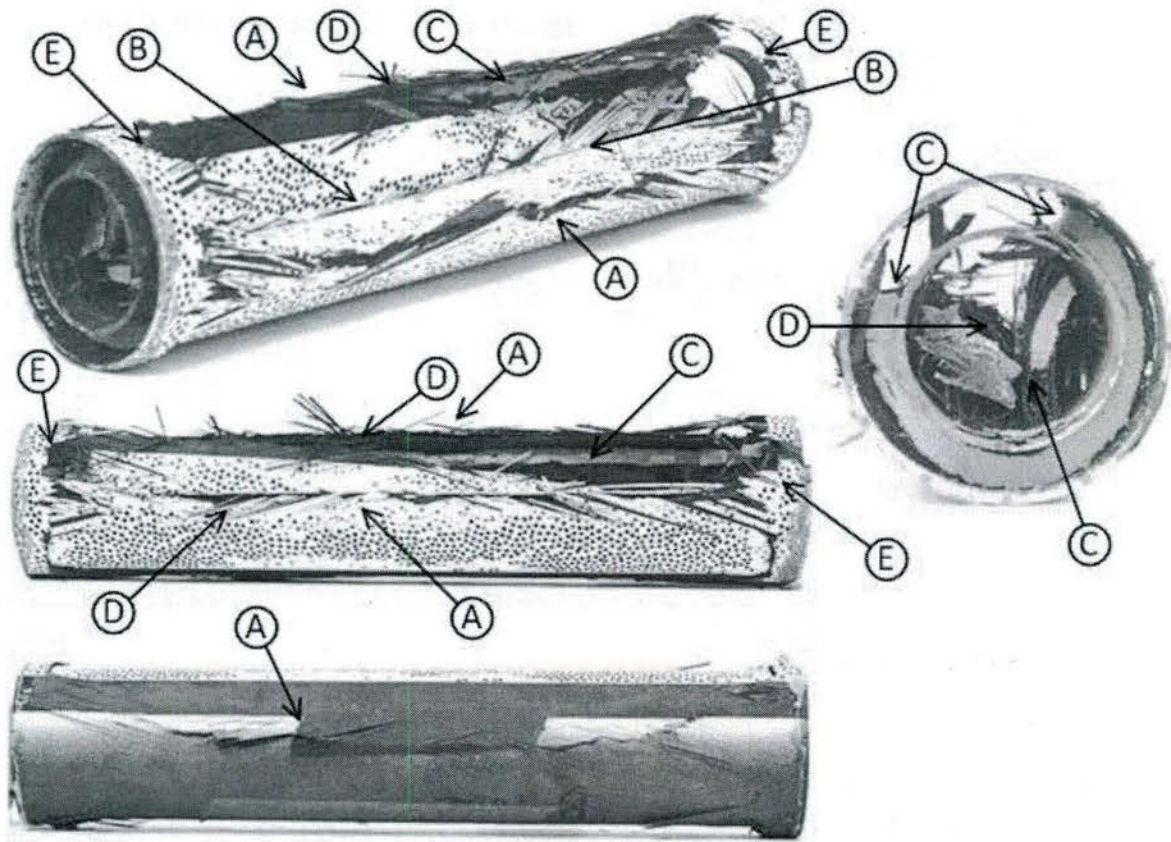


Figure 13: H80 core specimen post-mortem photographs; (top left) isometric view; (center left) front view; (bottom left) bottom view; (right) right view; (A) longitudinal cracking corresponding to lobes of mode 3 buckling shape; (B) center of fold where buckling directions of tubes aligned; (C) Through-thickness tearing of both the tubes and core corresponding to collapse of the inner tube; (D) Delamination and fiber pullout along tear edges; (E) Circumferential cracking from endcaps

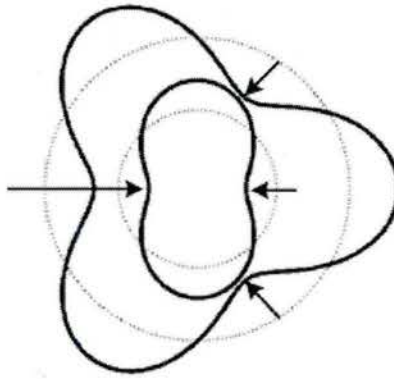


Figure 14: Schematic of buckling mode shapes in case where both tube collapse without a dwell; note collinear buckling direction of inner and outer tubes

Conclusions

The hydrostatic implosion of double hull composite cylinders with polymeric foam cores of parametrically graded density was investigated. High-speed photography and dynamic pressure sensors were used to record implosion events in a unique facility, and 3-D, underwater DIC was used to attain full-field displacement data during the collapse. Careful evaluation of the experimental data has enabled the following conclusions to be made:

- The inner and outer facesheets of a double hull structure implode separately from one another, and, depending on collapse pressure, the inner tube may either survive or implode as well.
- Double hull composite structures demonstrate one of three general implosion behaviors: (1) The outer tube implodes but the inner survives; (2) The outer tube implodes, there is a brief time delay, then the inner implodes; (3) The outer and inner tubes implode in a singular motion with no dwell.
- The inner tube implodes if the collapse pressure of the outer tube is higher than the inner.

- The inner and outer tubes collapse in a singular motion if their natural buckling directions are aligned, but a dwell occurs if they are not.
- The increase in critical pressure of the outer facesheet on account of the double hull structure is directly proportional to the strength of the foam core. The proportionality constant has been shown to be a function of geometrical properties of the core.
- In cases where the outer tube collapses but the inner does not, an implosion pulse is generated which is similar to a monolayer tube implosion, but of lower frequency and amplitude. This is created by the outer tube collapsing and flattening against the inner.
- In situations where both inner and outer tubes implode, the pulse from the outer tube's collapse is followed by a secondary implosion pulse from the collapse of the inner tube. The impulse and amplitude of the second event may match or exceed that of the first.
- After normalizing for collapse pressure, the impulse of a double hull implosion is constant with core density, regardless of whether the inner tube implodes or not.
- Energy released by a double hull implosion, normalized by hydrostatic energy, tends to increase with core density.
- Specimens with stronger cores undergo increased damage from implosion, on account of their higher collapse pressures. This increase in damage, combined with the increase in foam core crushing energy, causes higher strength cores to mitigate more energy overall.

Acknowledgements

The authors would like to acknowledge the Office of Naval Research and Dr. Yapa D.S. Rajapakse for providing financial support for this research under Grant No. N00014-10-1-0662. The authors would also like to acknowledge the DIAB Corporation (DeSoto, TX) for providing the foam core materials used in this study.

References

- [1] S. E. Turner and J. M. Ambrico, "Underwater Implosion of Cylindrical Metal Tubes," *J. Appl. Mech.*, vol. 80, p. 11013, 2012.
- [2] S. E. Turner, "Underwater implosion of glass spheres," *J. Acoust. Soc. Am.*, vol. 121, no. 2, p. 844, 2007.
- [3] R. J. Urlick, "Implosions as Sources of Underwater Sound," *J. Acoust. Soc. Am.*, pp. 2026–2027, 1963.
- [4] M. Orr and M. Schoenberg, "Acoustic signatures from deep water implosions of spherical cavities," *J. Acoust. Soc. Am.*, vol. 59, no. 5, pp. 1155–1159, 1976.
- [5] P. E. Harben and C. O. Boro, "Implosion source development and diego garcia reflections," in *23rd Seismic Research Review: Worldwide Monitoring of Nuclear Explosions*, 2001, pp. 23–31.
- [6] E. Cartlidge, "Accident grounds neutrino lab," *Physics World*, 2001. [Online]. Available: <http://physicsworld.com/cws/article/news/2001/nov/15/accident-grounds-neutrino-lab>.

[Accessed: 22-Jun-2016].

- [7] "Robotic deep-sea vehicle lost on dive to 6-mile depth," 2014. [Online]. Available: <http://www.whoi.edu/news-release/Nereus-Lost>. [Accessed: 22-Jun-2016].
- [8] C. Farhat, K. G. Wang, A. Main, S. Kyriakides, L. H. Lee, K. Ravi-Chandar, and T. Belytschko, "Dynamic implosion of underwater cylindrical shells: Experiments and Computations," *Int. J. Solids Struct.*, vol. 50, no. 19, pp. 2943–2961, 2013.
- [9] C. M. Ikeda, J. Wilkerling, and J. H. Duncan, "The implosion of cylindrical shell structures in a high-pressure water environment," *Proc. R. Soc. A Math. Phys. Eng. Sci.*, vol. 469, no. 2160, 2013.
- [10] S. Gupta, V. Parameswaran, M. A. Sutton, and A. Shukla, "Study of dynamic underwater implosion mechanics using digital image correlation," *Proc. R. Soc. A Math. Phys. Eng. Sci.*, vol. 470, no. 2172, pp. 20140576–20140576, 2014.
- [11] H. Hernandez-Moreno, B. Douchin, F. Collombet, D. Choqueuse, and P. Davies, "Influence of winding pattern on the mechanical behavior of filament wound composite cylinders under external pressure," *Compos. Sci. Technol.*, vol. 68, no. 3–4, pp. 1015–1024, 2008.
- [12] S. H. Hur, H. J. Son, J. H. Kweon, and J. H. Choi, "Postbuckling of composite cylinders under external hydrostatic pressure," *Compos. Struct.*, vol. 86, no. 1–3, pp. 114–124, 2008.
- [13] C. J. Moon, I. H. Kim, B. H. Choi, J. H. Kweon, and J. H. Choi, "Buckling of filament-wound composite cylinders subjected to hydrostatic pressure for underwater vehicle

applications," *Compos. Struct.*, vol. 92, no. 9, pp. 2241–2251, 2010.

- [14] C. T. F. Ross, A. P. F. Little, Y. Haidar, and A. A. Waheeb, "Buckling of carbon/glass composite tubes under uniform external hydrostatic pressure," *Strain*, vol. 47, no. SUPPL. 1, pp. 156–174, 2011.
- [15] P. T. Smith, C. T. F. Ross, and A. P. F. Little, "Collapse of composite tubes under uniform external hydrostatic pressure," *J. Phys. Conf. Ser.*, vol. 181, pp. 156–157, 2009.
- [16] C. Yang, S.-S. Pang, and Y. Zhao, "Buckling Analysis of Thick-Walled Composite Pipe under External Pressure," *J. Compos. Mater.*, vol. 31, no. 4, pp. 409–426, 1997.
- [17] M. Pinto, S. Gupta, and A. Shukla, "Study of implosion of carbon/epoxy composite hollow cylinders using 3-D Digital Image Correlation," *Compos. Struct.*, vol. 119, pp. 272–286, 2015.
- [18] M. Pinto, S. Gupta, and A. Shukla, "Hydrostatic Implosion of GFRP Composite Tubes Studied by Digital Image Correlation," *J. Press. Vessel Technol.*, vol. 137, no. 5, p. 51302, 2015.
- [19] M. Pinto and A. Shukla, "Mitigation of pressure pulses from implosion of hollow composite cylinders," *J. Compos. Mater.*, 2015.
- [20] J.-H. Han, G. a. Kardomateas, and G. J. Simitses, "Elasticity, shell theory and finite element results for the buckling of long sandwich cylindrical shells under external pressure," *Compos. Part B Eng.*, vol. 35, pp. 591–598, 2004.

- [21] J. . Hutchinson and M. . He, "Buckling of cylindrical sandwich shells with metal foam cores," *Int. J. Solids Struct.*, vol. 37, no. 46–47, pp. 6777–6794, 2000.
- [22] G. A. Kardomateas and G. J. Simitzes, "Buckling of Long Sandwich Cylindrical Shells Under External Pressure," *Jam*, vol. 72, no. 4, pp. 493–499, 2005.
- [23] A. V. Lopatin and E. V. Morozov, "Buckling of the composite sandwich cylindrical shell with clamped ends under uniform external pressure," *Compos. Struct.*, vol. 122, pp. 209–216, 2015.
- [24] J. Shen, G. Lu, D. Ruan, and C. Chiang Seah, "Lateral plastic collapse of sandwich tubes with metal foam core," *Int. J. Mech. Sci.*, vol. 91, pp. 99–109, 2015.
- [25] M. Ohga, A. Sanjeewa Wijenayaka, and J. G. A. Croll, "Reduced stiffness buckling of sandwich cylindrical shells under uniform external pressure," *Thin-Walled Struct.*, vol. 43, no. 8, pp. 1188–1201, 2005.
- [26] K. Arjomandi and F. Taheri, "Stability and post-buckling response of sandwich pipes under hydrostatic external pressure," *Int. J. Press. Vessel. Pip.*, vol. 88, no. 4, pp. 138–148, 2011.
- [27] K. L. Koudela and L. H. Strait, "Simplified Methodology for Prediction of Critical Buckling Pressure for Smooth-Bore Composite Cylindrical Shells," *J. Reinf. Plast. Compos.*, vol. 12, no. 5, pp. 570–583, 1993.
- [28] R. H. Cole, *Underwater Explosions*. Princeton, New Jersey: Princeton University Press, 1948.

- [29] A. B. Arons and D. R. Yennie, "Energy partition in underwater explosion phenomena," *Rev. Mod. Phys.*, vol. 20, no. 3, pp. 519–536, 1948.
- [30] ASTM standard D1621, "Standard Test Method for Compressive Properties Of Rigid Cellular Plastics," *ASTM Int.*, 2016.
- [31] R. von Mises, "The Critical External Pressure of Cylindrical Tubes," *Zeitschrift des Vereines Dtsch. Ingenieure*, vol. 58, no. 19, pp. 750–767, 1914.
- [32] R. von Mises, "The Critical External Pressure of Cylindrical Tubes Under Uniform Radial and Axial Load," *Stodola's Festschrift*, pp. 418–430, 1929.